MULTI-SCALE ANALYSIS AND SIMULATION IN 3D CRYSTAL PLASTICITY LARGE DEFORMATION FINITE ELEMENT PLATFORMS TO PREDICTING AND DESIGNING THERMOMECHANICAL RESPONSES OF METALLIC NANO-LAYERS

by

Zara Moleinia

A Dissertation

Submitted to the Faculty of Purdue University

In Partial Fulfillment of the Requirements for the degree of

Doctor of Philosophy

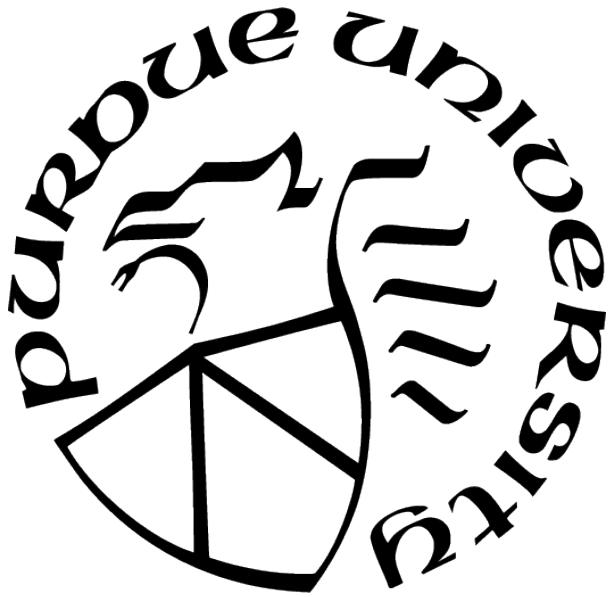

School of Materials Engineering

West Lafayette, Indiana

December 2020

THE PURDUE UNIVERSITY GRADUATE SCHOOL
STATEMENT OF COMMITTEE APPROVAL

Dr. David F. Bahr, Chair

School of Materials Engineering

Dr. R. Byron Pipes

School of Materials Engineering

Dr. Lia Stanciu

School of Materials Engineering

Dr. Michael Titus

School of Materials Engineering

Approved by:

Dr. David F. Bahr

TABLE OF CONTENTS

LIST OF TABLES

LIST OF FIGURES

ABSTRACT

The current work centers on multi-scale approaches to simulate and predict metallic nano-layers thermomechanical response in crystal plasticity large deformation finite element platforms. Multiple parts including multi-scale modeling divided into two major scales; nano- and homogenized levels, sensitivity analysis, micro-scale simulations, precipitate hardening, and computational aid hardware and software development are researched. Copper/niobium nano-layers are designated as case studies. At the nano-scale, a size-dependent constitutive model based on entropic kinetics is developed through the thermodynamical phase space of metallic nano-systems. A deep-learning adaptive boosting technique called the single layer calibration is established to acquire associated constitutive parameters applicable to a broad scope of setups entirely different from those of calibrations. The model is validated by experimental data with solid agreements followed by the simulation of multiple cases regarding size, loading pattern, layer type, and geometrical effects specifying the inconsequential effects of layers or loading orientations, predominant influence of size over the other traits, the impacts of a constituent in a bi-crystal cases, and generalized size effects on yield and flow strengths as well as transition strain. Sensitivity analysis is performed on the size-dependent constitutive model as a diagnostic-prognostic field through the factor prioritization in order to capture the influential parameters where the size effects designed parameters, namely, m, c_s, c_{sat}, and h_0 are found the dominant factors on the main behavioral features. At the homogenized level, macro-homogeneity is utilized through the statistical mechanics of the microcanonical ensemble and the Clausius-Duhem inequality to link the scales through entropy flux. A homogenized crystal plasticity-based constitutive model is developed with the aim of expediting while retaining the accuracy of the computational processes for which effective constitutive functionals are realized. The high nonlinearity of the functional constants is dealt with through a metaheuristic genetic algorithm approach leading to determining the associated terms in an optimized fashion. The homogenized constitutive model

results are favorably verified with nano-scale data while expediting computational processes by several orders of magnitude. The temperature effects are captured through developing a temperature-dependent constitutive model where elastic constants and effective functional parameters are determined and calibrated. The model is validated with experimental data with multiple demonstrations of temperature effects identifying the degradation of a thin nano-layer at high temperature into a thicker one at lower temperature and dramatic drops of up to $\approx 80\%$ in flow strength at about $1000K$. The work is expanded to micro-scale where a crystal plasticity constitutive model is developed with the same backbones of the model presented in the nano range. The implicit trace of size is designed in this format as the physics behind the spectrum lead. The deep-learning single layer calibration is utilized to obtain the associated constitutive parameters where validated by the experimental data. Precipitate hardening phenomenon is realized and implemented considering Orowan strengthening mechanism in nano-systems. Wherefore several cases indicating the impacts of size and volume fraction of precipitates on mechanical properties are assessed and discussed revealing the exponential increase on flow strength and hardening with respect to precipitate volume fractions, the high stress absorption by precipitates creating extreme stress gradient with the matrix, and the effect of a strengthened constituent, here Nb, on the overall behavior of these nanolamellars. The developed nano-scale size-dependent constitutive model, the deep-learning single layer calibration method, sensitivity analysis, homogenized constitutive model, temperature-dependent constitutive model, micro-scale constitutive model, precipitated strengthening analyses, genetic algorithms, numerical solvers, and process optimizers are implemented through three-dimensional crystal plasticity nonlinear finite element codes in the large deformation platform. A dedicated supervised cluster has been constructed with specific architecture and orchestration policies compatible with the current data processing and workloads.

1. INTRODUCTORY IN METALLIC NANO-LAYERS

1.1 Introduction

Metallic nano-layers are nano-systems made of alternating metallic lamellae while associated mechanical properties become distinctive from those of the bulk counterparts, Fig. 1.1. These materials have exceptional mechanical properties including significant yield and flow strength, considerable ductility, notable fatigue tolerance, substantial radiation damage forbearance, and forth.

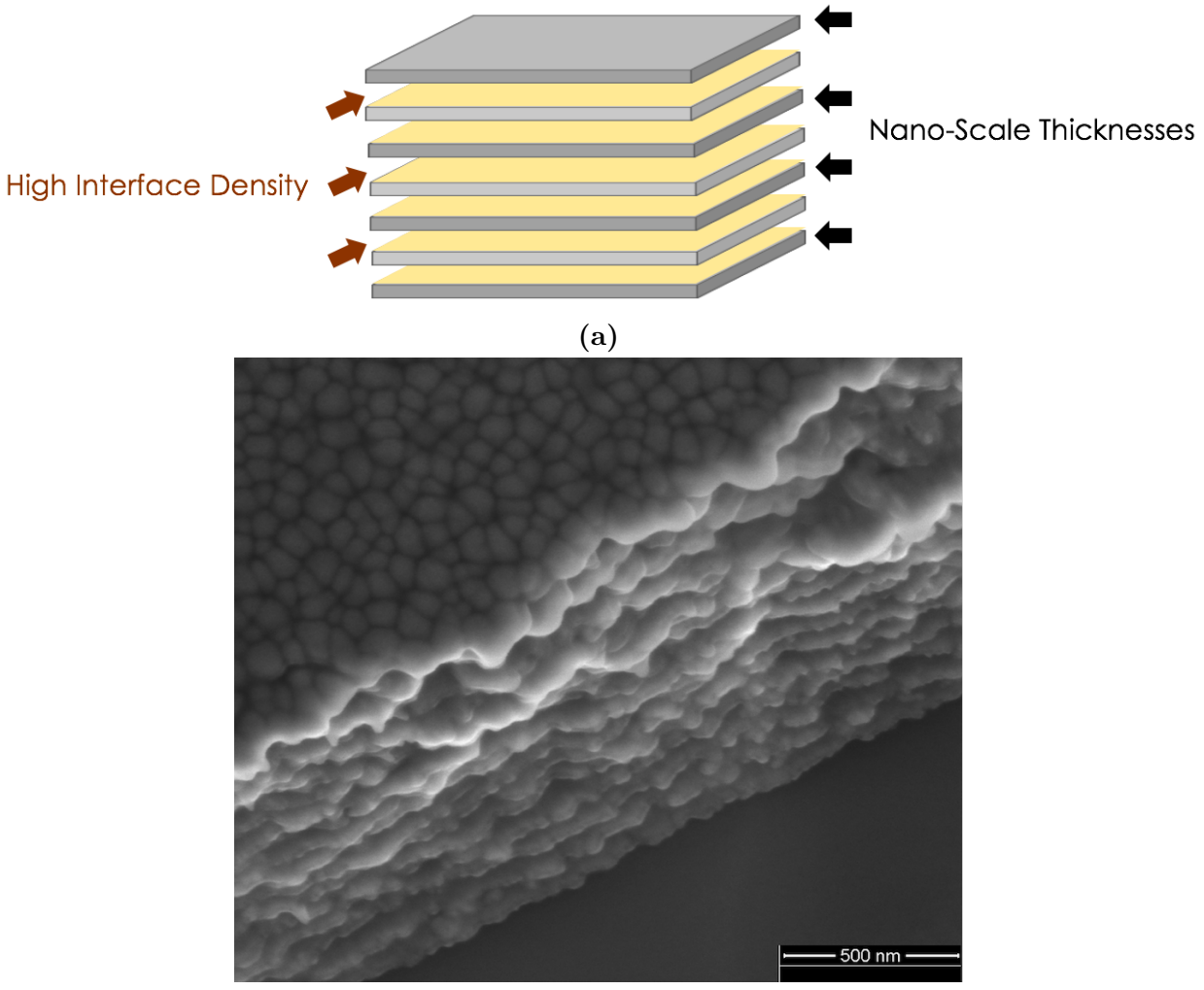

(a)

(b)

Figure 1.1: (a) Metallic nano-layers made of alternating metallic lamellae with a high density of interface. (b) Scanning electron microscopy of a copper chromium nano-layer with the thickness of about 30 nm.

As an example, in copper niobium nano-layers having a thickness of 40 nm, flow strength can reach about 1.75 GPa with the ductility of more than 30 % [1], as demonstrated in Fig. 1.2.

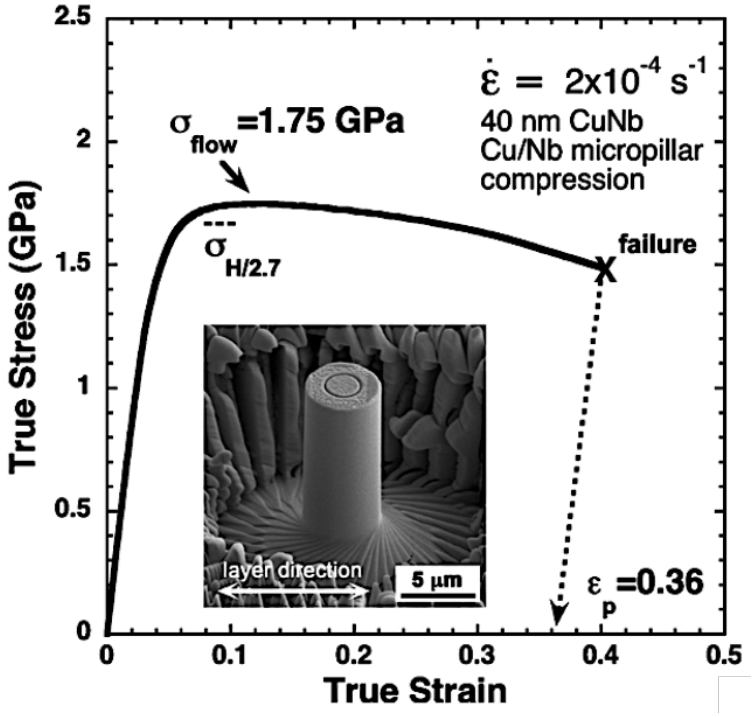

Figure 1.2: An example of a copper niobium nano-layer having a thickness of 40 nm with flow strength of about 1.75 GPa and the ductility of more than 30 % [1].

1.2 Application of Metallic Nano-Layers

The novel properties of these nano-composites such as high strength and ductility make them conducive to occupy a prominent portion of vast practical applications, Fig. 1.3. These features can be attributed to the high density of interfaces, fine microstructures, and complex dislocation mechanisms [15]. Design and behavioral prediction of metallic nano-lamellars necessitate a profound understanding of deformation mechanisms ascribed to layer spacing, interface morphology and composition, and dislocation mechanisms in different segments.

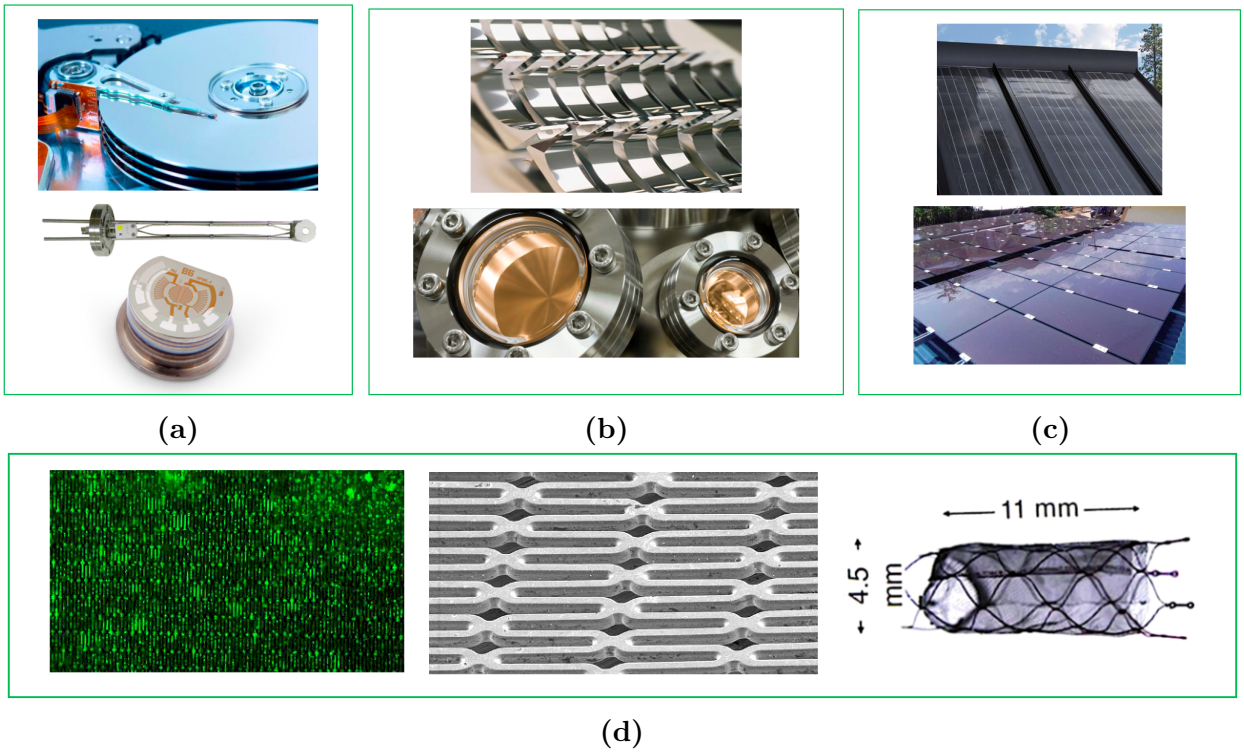

Figure 1.3: Diverse applications of metallic nano-layers in (a) electronic industry, (b) coating mechanical tools, (c) solar systems, and (d) medical treatments.

1.3 Computational Methods in Metallic Nano-Layers

The majority of the studies on metallic nano-films are performed either for large scales using local and simplified models [16, 17] or for very small scales using molecular dynamics [2] as well as discrete dislocation dynamics.

The molecular dynamics results can not be adequately verified with experimental data as it is deducible in Fig. 1.4, where the simulation and pillar compression test results could not agree, especially in yielding and flow strengths.

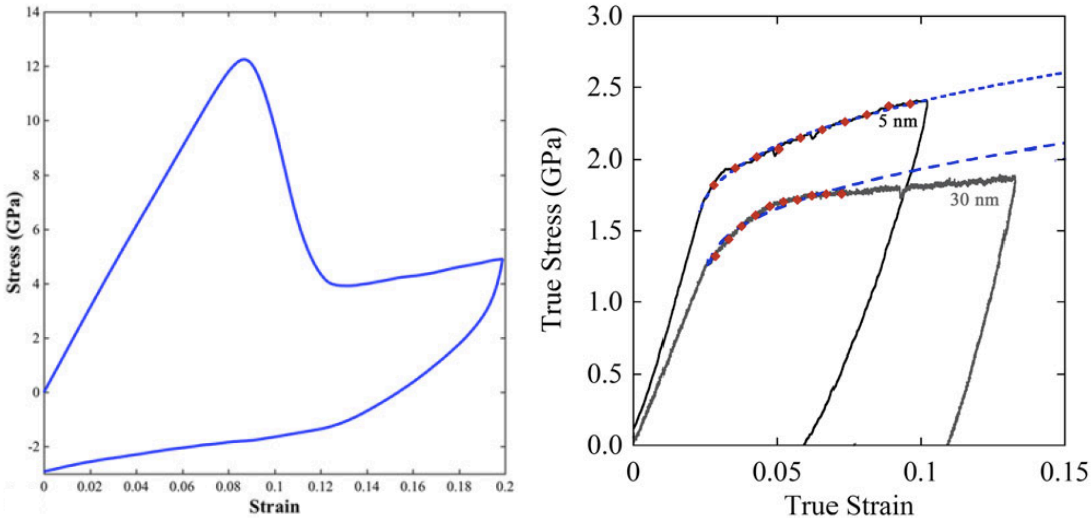

Figure 1.4: Comparison of the results in (a) a typical loading-unloading stress-strain curve from molecular dynamics simulations and (b) the micro-pillar compression test for two individual layer thicknesses of 5 nm and 30 nm [2]. The appreciable discrepancy between the simulation and experiment, especially in yielding and flow strengths, implies the remote possibility of proper verification.

One of the most important reasons for these types of discrepancies is associated with the consideration of a high strain rate in the atomic level which naturally is compatible with the velocity of the variable therein, yet, not with practical cases.

Discrete dislocation dynamic simulations also suffer more or less the same limitations. Being unable to capture a variety of dislocation mechanisms at the same time, being restricted to two-dimensional modeling for practicalities, as demonstrated in Fig. 1.5 [3], thus, neglecting several three-dimensional dislocation interactions, not being capable of detecting large plastic strains and modeling realistic unit cells as well as non-local size effects, and huge time and energy consumption, are of the shortcomings.

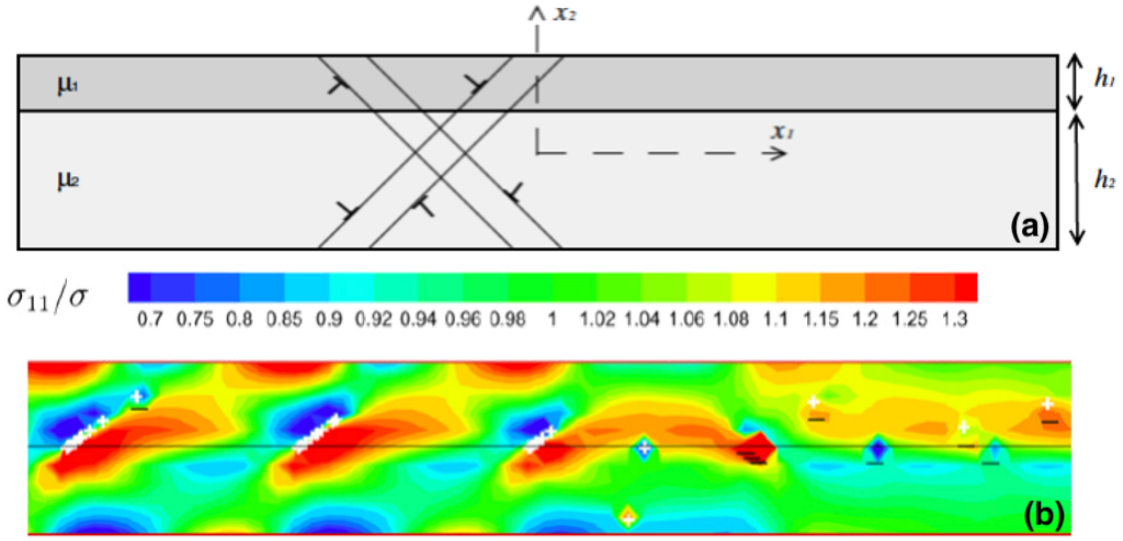

Figure 1.5: Discrete dislocation dynamic simulation of (a) a two dimensional Al/Cu bilayer for which (b) the normalized contour of the normal stress on the x_1 direction is plotted [3].

1.4 Selected Computational Approach in Metallic Nano-Layers

The continuum models are able to capture vital features, however, if simplified approaches are pursued, to a limited extent. Therefore, enhancing the constitutive models and deformation mechanisms in these types of simulations are extremely beneficial in detecting the actual, verifiable responses, due to which this work will be thoroughly concentrating on these matters.

At the micrometer range, the Hall-Petch relation [18, 19] is often employed, $\sigma \propto d^{-0.5}$, indicating the increase of strength with layer thickness refinement based on dislocation pile-up against interfaces along with other transgranular dislocation mechanisms as the dominant strength-controlling processes. The approach is founded on the average size simulation leading to the computational simplification [20] which makes it easier to incorporate in generic applications while in the sensitive cases is not advised. At nano-scales, this relation breaks down due to the insufficient impact of decaying exponent and lack of other associated effects which is mostly observed when the motion of dislocations is hindered at interfaces and grain boundaries [21].

To overcome these difficulties and address the crystalline anisotropy and size dependence aspects in the associated governing equations, crystal plasticity (CP), a proper tool reflecting the anisotropic nature of crystalline materials [22], along with finite element (FE) analysis is utilized. The crystal plasticity finite element (CPFE) approach in the large deformation platform, when performed in three dimensions, has the ability to assess and simulate the grain interactions, interface abrupt mechanical transitions, mixed deformation mechanisms, complex boundary conditions, and diverse empirical and physics-based constitutive models [23, 24]. Three-dimensional CPFE method can be applied in a multi-scale framework providing comprehensive plastic kinematics and thermodynamics of a system.

Advanced CPFE analyses can be utilized in a widen length spectrum from nano to macro polycrystalline scales through constitutive models derived based on the specifics of the body phase space. In addition, the acquired outcomes can be adequately compared through the experimental data as one of the prominent advantages of utilizing such approaches.

2. FUNDAMENTAL THEORIES AND SCHEMES

2.1 Introduction

This research is aimed at developing a homogenized multi-scale crystal plasticity model with parametric representations of the nano-level morphology in its evolution laws. In this framework, CP models hierarchically encompass dominant features at each scale through the constitutive models followed by the implementation of microstructure properties and finally behavioral prediction and design. The computational processes proceed through calibration and validation with experimental data including pillar compression tests, to gather information assisting with the constitutive model variables and effective functionals terms. In order to create a broad, in-depth perspective, in the subsequent sections, the rational behind the utilization of CPFE approaches are discussed in detail.

2.2 Crystal Plasticity Approach

The elastoplastic deformation of crystalline aggregates is mechanically anisotropic due to the anisotropy of the elastic constants and the activation of the crystallographic deformation mechanisms. As a consequence, the associated mechanical phenomena such as flow stress and strain hardening inhere the same trait indicating that mechanical parameters of a crystalline matter embedded in constitutive models are tensor quantities [25]. Fig. 2.1 exhibits a polycrystalline copper including eleven grains under uniaxial tensile test with a non-uniform distribution of plastic deformation across the sample along and even within the grains.

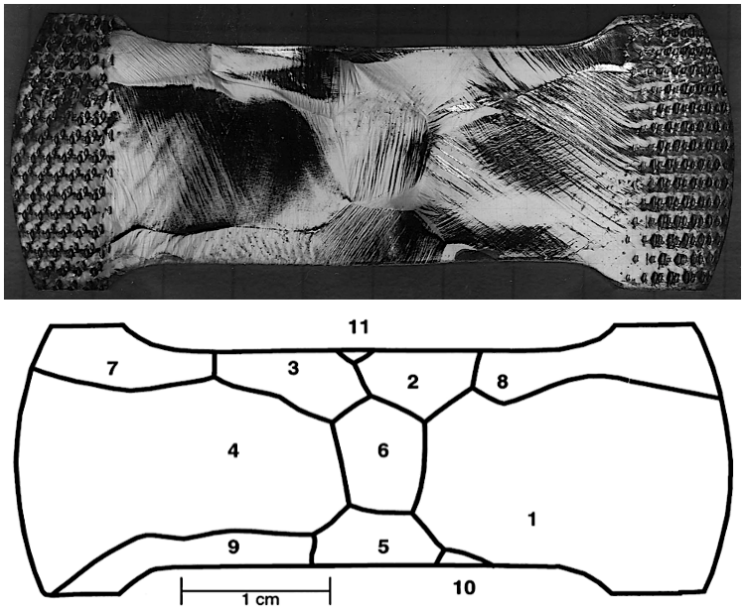

Figure 2.1: An example of nonuniform plastic deformation in a polycrystalline copper including eleven grains under a uniaxial tensile test [4]. Irregular deformations are observed along and within the grains.

Furthermore, in single crystals, orientation dependence can result in significant discrepancies in mechanical properties. Fig. 2.2 displays different stress-strain curves for a single crystal nickel-base superalloy in both elastic and plastic regimes for dissimilar orientations of $\langle 001 \rangle$, $\langle 011 \rangle$, and $\langle 111 \rangle$. These concerns can be addressed through crystal plasticity by having orientations as the primary state variables while continuum plasticity is unable to account for those effects due to the lack of related intrinsic variables within.

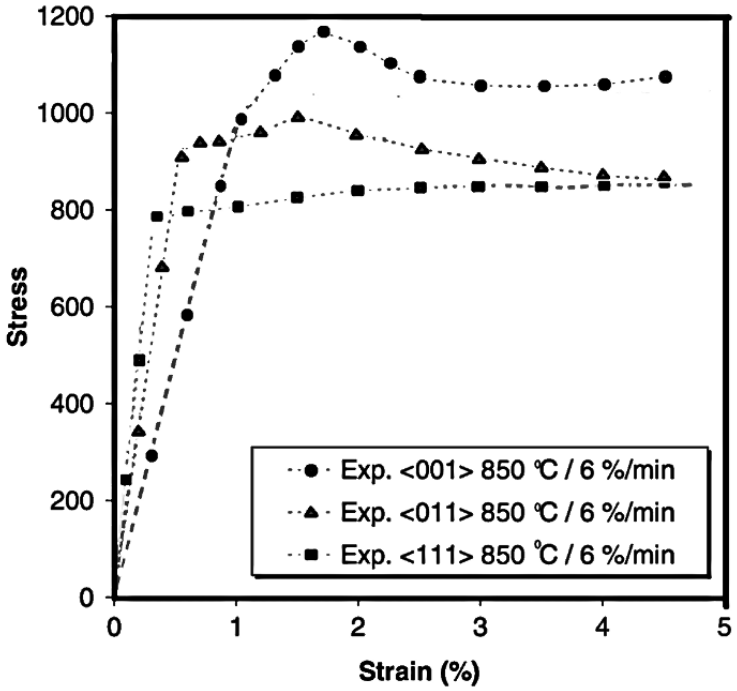

Figure 2.2: The stress-strain curves of a single crystal nickel-base superalloy for three directions of $\langle 001 \rangle$, $\langle 011 \rangle$, and $\langle 111 \rangle$ indicating the anisotropy phenomenon [5].

2.3 Large Deformation Analysis

Plasticity theories are applicable primarily to solids experiencing inelastic deformations considerably greater than elastic ones. Once strains or rotations become so immense, large displacement kinematics must be considered which is the case for most metals and metallic alloys. The crystal plasticity approach has the potential to be designed for either small or large deformation [25]. Small deformation relations simplify the implementation and simulation process, yet, make the model limited to a small strain range. Experimental results in metallic nano-composites, as demonstrated in Fig. 2.3, suggest the existence of large strains up to about 30%.

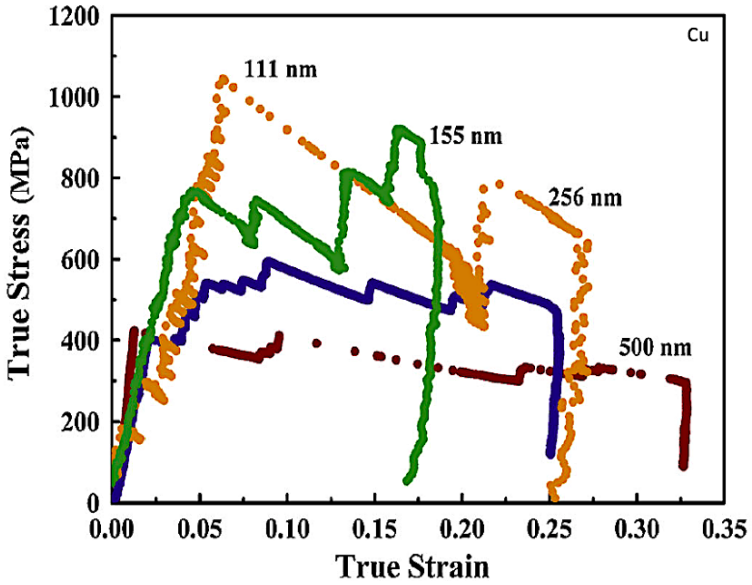

Figure 2.3: Stress-strain curves for single crystals of copper for four thicknesses of 111 nm, 155 nm, 256 nm, and 500 nm with large plastic deformation up to about 30 % [6].

Thereby, in spite of the straightforward use of infinitesimal strain theory, those relations cannot be relied on for practical strain ranges, and finite strain theory must be accommodated where different configurations are considered for deformation conditions linked through motion functions.

2.4 Rate Dependence Phenomenon

Another characteristics related to metals and metallic alloys, is the rate dependence responses of these materials, as illustrated in Fig. 2.4.

As observed, the critical points of the stress-strain curves change values with the variation of the applied strain rates. Thus, this matter must as well be addressed properly in the associated governing relations, otherwise, the real properties can not be reliably detected.

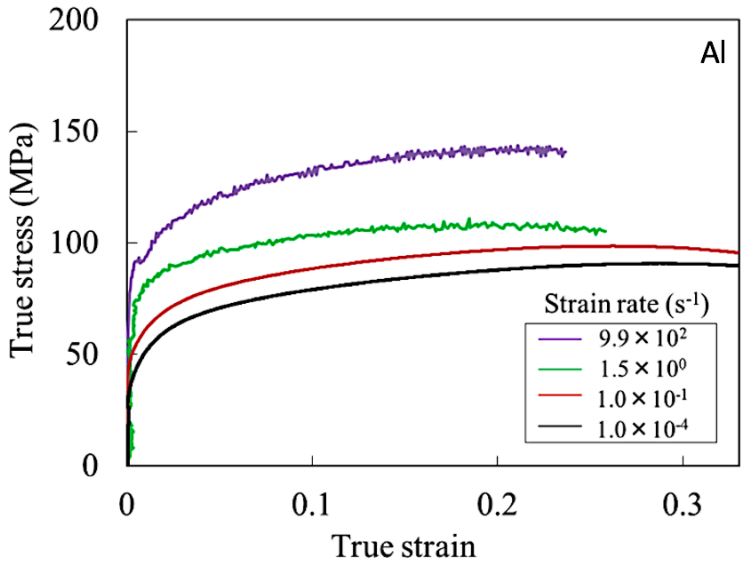

Figure 2.4: Stress-strain curves of an aluminum specimen under four different strain rates [7]. The variation in strain rates affects the critical points values as well as the overall behavior of the sample indicating the rate dependence nature of the tested material.

2.5 Large Deformation Kinematics

The kinematics of finite strain describes the process where a body originally located in a reference configuration is deformed in the current state by a combination of externally applied forces and displacements over a period of time, t. The motion function $\chi(\mathbf{X}, t)$ maps a material position vector $\mathbf{X}$ or a reference line element $\mathbf{dS}$ to a spatial position vector $\mathbf{s}$ or a current line element $\mathbf{ds}$ with material displacement $\mathbf{U}(\mathbf{X}, t)$ and designated right-handed coordinate system, as demonstrated in Fig. 2.5

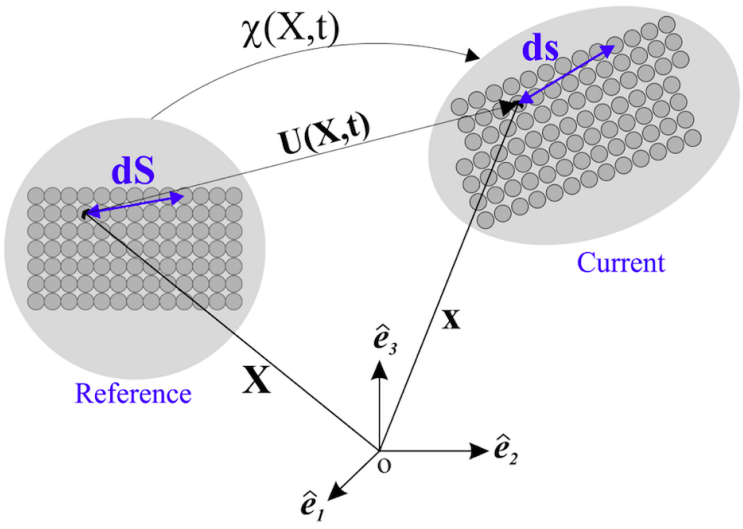

Figure 2.5: Deformation of a material position and line from reference to spatial configuration mapped by the motion function.

In this system, the deformation gradient representing the quality of the motion is defined in terms of motion or displacement functions with

$$\mathbf{F}(\mathbf{X},t) = \nabla_{\mathbf{X}}\ \chi(\mathbf{X},t) = \mathbf{I} + \frac{\partial \mathbf{U}}{\partial \mathbf{X}}\,, \tag{2.5.1}$$

as a generalized definition of deformation in a system. Accordingly, the Lagrangian strain is determined as

$$\mathbf{E} = \frac{1}{2}\left[\frac{\partial \mathbf{U}}{\partial \mathbf{X}} + \left(\frac{\partial \mathbf{U}}{\partial \mathbf{X}}\right)^{T} + \frac{\partial \mathbf{U}}{\partial \mathbf{X}}\left(\frac{\partial \mathbf{U}}{\partial \mathbf{X}}\right)^{T}\right]\,, \tag{2.5.2}$$

where the first two terms generally define the small strain relations whereas the last term appears only due to the large deformation consideration emphasizing the second-order displacement gradient. Similarly, the Eulerian strain is described through

$$\mathbf{e} = \frac{1}{2}\left[\frac{\partial \mathbf{u}}{\partial \mathbf{x}} + \left(\frac{\partial \mathbf{u}}{\partial \mathbf{x}}\right)^{T}\right]\,. \tag{2.5.3}$$

At this point, the rate dependence feature of the system is recognized via the velocity gradient as

$$\mathbf{l} = \nabla_{\mathbf{x}} \mathbf{v}(\mathbf{x}, t) \, . \tag{2.5.4}$$

Now, by incorporating the fundamental concepts of the finite strain scheme, the main structure of crystal plasticity is built as discussed in the following sections.

2.6 Crystal Plasticity in Large Deformation Finite Element

Large strain-description is accommodated through a multiplicative decomposition of the total deformation gradient, $\mathbf{F}$, into the elastic deformation gradient, $\mathbf{F}^e$, which is the deformation component due to the reversible response of the lattice under external loads and displacements as well as rigid-body rotations, and the plastic deformation gradient, $\mathbf{F}^p$, as an irreversible deformation that persists when all external forces and displacements are removed. In this sense, the transformation of the reference state by $\mathbf{F}^p$ leads to the creation of the intermediate configuration. The intermediate configuration signifies the presence of dislocations which produce the permanent shape changes. In addition, due to the rate dependence of most metals and metallic alloys, the rate of deformation gradient needs to be involved through the velocity gradient, $\mathbf{l} = \dot{\mathbf{F}}\mathbf{F}^{-1}$, as well.

The decomposition framework is demonstrated in Fig. 2.6, where an atomistic structure in the reference configuration is in the undeformed state. The current configuration displays the deformed structure including both elastic and plastic deformations where the plastic part of displacements in the form of stretch type is calculated in the intermediate configuration.

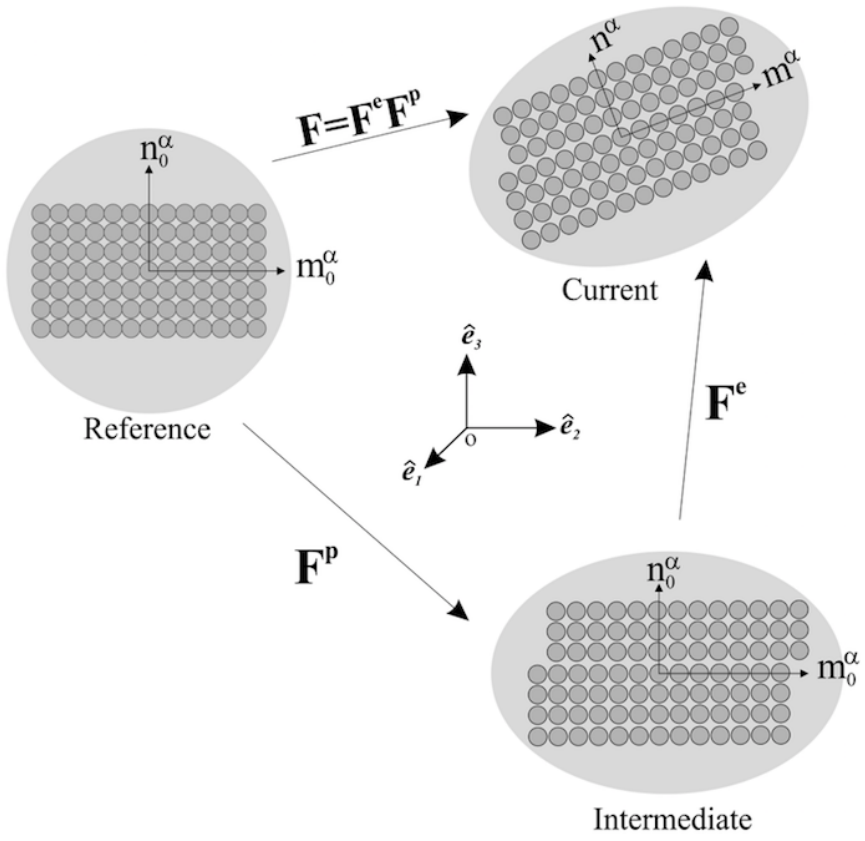

Figure 2.6: Framework decomposition into reference, intermediate, and current configuration.

With the presence of plastic deformations, multiplicative decomposition is adopted in order to divide the elastic and plastic parts of the deformation. In fact, an intermediate configuration is introduced to solve the indeterministic equation of $\mathbf{F} = \mathbf{F}^e\mathbf{F}^p$ by calculating $\mathbf{F}^p$. For a given deformation, the plastic part $\mathbf{F}^p$ is calculated using constitutive model via the plastic part of the velocity gradient, $\mathbf{l}^p = \dot{\mathbf{F}}^p\mathbf{F}^{-p}$, where Asaro equation [26] is employed in order to find $\mathbf{l}^p$ as

$$\mathbf{l}^p = \sum_{\alpha=1}^{N} \dot{\gamma}^\alpha \mathbf{s}_0^\alpha \,, \tag{2.6.1}$$

in which $s_0^\alpha = m_0^\alpha \otimes n_0^\alpha$ is the Schmid tensor where m_0^α and n_0^α are slip and normal directions, respectively, in the reference configuration. Most of the constitutive models are Orowan

based [27], i.e.,

$$\dot{\gamma}^{\alpha} = \rho_m^{\alpha} b^{\alpha} v^{\alpha} \,, \tag{2.6.2}$$

where ρ_m^{α} is the mobile dislocation density, b^{α} the Burgers vector, and v^{α} the dislocation velocity for a given slip system. At this point, constitutive models must be utilized in order to calculate $\dot{\mathbf{F}}^{p}$. Thus, an integration scheme needs to be accommodated to determining the total plastic part of the deformation gradient. Afterward, the elastic part of the deformation is computed through

$$\mathbf{F^e} = \mathbf{F}\mathbf{F}^{-\mathbf{p}} \tag{2.6.3}$$

Further, the elastic part of deformation gradient can be used in Hooke's law in order to acquire the Second Piola-Kirchhoff stress, $\mathbf{S}$, which is obtained in terms of Green-Lagrange strain and anisotropic material elastic tensor, $\mathscr{C}$, with

$$\mathbf{S} = \mathscr{C}\mathbf{E} \,, \tag{2.6.4}$$

where $\mathbf{E}$ in terms of the deformation gradient is expressed as

$$\mathbf{E} = \frac{1}{2}(\mathbf{F}^{eT}\mathbf{F}^{e} - \mathbf{I}) \,. \tag{2.6.5}$$

Here, solving the equilibrium equation in the current configuration requires the calculation of Cauchy stress, $\boldsymbol{\sigma}$, with regard to Second Piola-Kirchhoff stress by

$$\boldsymbol{\sigma} = \frac{1}{|\mathbf{F}^{e}|}\mathbf{F}^{e}\mathbf{S}\mathbf{F}^{eT} \,. \tag{2.6.6}$$

This relation holds due to plastic incompressibility, i.e., $\det\mathbf{F}^{p} = 1$.

In the subsequent parts, the equilibrium equation is specified through finite element meth-

ods. Finite element (FE) methods are a powerful numerical tool with a broad scope of science and engineering applications. In FE analysis the problem domain is discretized into geometric elements along with considering the material properties and governing equations. Afterwards, the domain is constructed and represented with equations through associated boundary conditions. These equations are solved signifying the estimated responses of the system. Generally, in solid mechanics, the focus is on bodies in equilibrium, that is, the summation of forces and moments is also zero for any sub-system or element. In any closed sub-domain, conservation of linear momentum compels force balances expressed by

$$\sigma_{ij,j} + f_i = 0 \tag{2.6.7}$$

as equilibrium equations, where $\sigma_{ij,j}$ denotes the Cauchy stress components and f_i the body force members in the indicial notation and large deformation framework. The relation between stress and strain, make equilibrium equalities, partial differential equations with exact and approximate solutions. The former normally requires simple geometries and loading conditions where most practical cases are excluded from that realm. The latter, however, can be dealt with through FE analysis as one of the numerical methods in order to acquire possible solutions in intricate real cases with numerous material and geometrical nonlinearities involved in their base relations.

The prime relations in the FE method commonly are derived through the potential energy. Considering Lagrangian description and the principle of virtual work on a system with the volume Λ and surface $\partial\Lambda$, the equilibrium equation in the variational form with neglecting point loads is stated with

$$P_{total} = \int_{\Lambda} \mathbf{S} : \delta\mathbf{E}\, dV - \int_{\Lambda} \mathbf{f} : \delta\mathbf{u}\, dV - \int_{\partial\Lambda} \mathbf{T} : \delta\mathbf{u}\, dS\,, \tag{2.6.8}$$

where $\mathbf{S}$ corresponds to second Piola-Kirchhoff stress, $\mathbf{E}$ the Lagrangian strain, $\mathbf{f}$ the body force, $\delta\mathbf{u}$ an arbitrary virtual displacement field, and $\mathbf{T}$ the surface traction.

The virtual strain $\delta\mathbf{E}$ due to the virtual displacement can be expressed by

$$\delta\mathbf{E} = \frac{1}{2}\left[\left(\frac{\partial\delta\mathbf{u}}{\partial\mathbf{X}}\right)^T\frac{\partial\mathbf{x}}{\partial\mathbf{X}} + \left(\frac{\partial\mathbf{x}}{\partial\mathbf{X}}\right)^T\frac{\partial\delta\mathbf{u}}{\partial\mathbf{X}}\right] . \tag{2.6.9}$$

Due to the fact that the majority of practical problems are in fact three dimensional, the associated finite element analysis is of interest in this work. Thereby, eight-node hexahedral elements demonstrated in Fig. 2.7 are discussed and utilized in the computational processes. For the mapped cubic element, the Lagrange shape functions are written as

$$N_I = \frac{1}{8}(1+\xi_I\xi)(1+\eta_I\eta)(1+\zeta_I\zeta) \;\; ; \;\; I = 1, 2, ..., 8 \, , \tag{2.6.10}$$

where (ξ_I, η_I, ζ_I) denotes the coordinates of the node I.

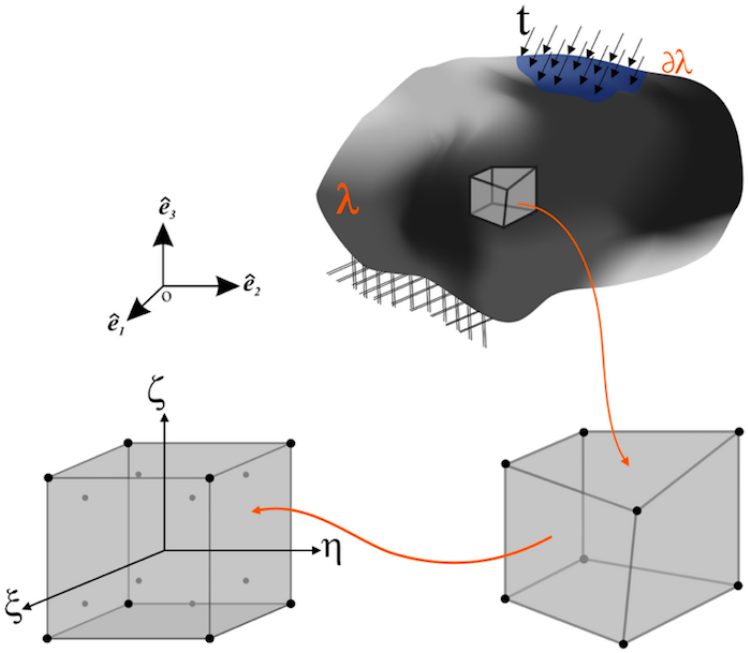

Figure 2.7: Eight-node hexahedral element.

For an isoparametric element, $\mathbf{X} = N_I\, X_I$, the virtual displacement field can be interpolated with shape functions $\mathbf{N}_I$ as a function of the virtual displacements in elemental nodes, $\delta\check{\mathbf{u}}$,

hence, the virtual Lagrangian strain is represented with

$$\delta\mathbf{E} = \frac{1}{2}\sum_{I}\left[(\delta\check{\mathbf{u}}_I \otimes \nabla_{\mathbf{X}}\mathbf{N}_I)^T\mathbf{F} + \mathbf{F}^T(\delta\check{\mathbf{u}}_I \otimes \nabla_{\mathbf{X}}\mathbf{N}_I)\right] . \tag{2.6.11}$$

Now, the Eulerian virtual displacement can be derived considering $\mathbf{e} = \mathbf{F}^{-T}\delta\mathbf{E}\mathbf{F}^{-1}$ and $\nabla_{\mathbf{x}} = \nabla_{\mathbf{X}}F^{-1}$ as

$$\delta\mathbf{e} = \frac{1}{2}\sum_{i}\left[(\delta\check{\mathbf{u}}_i \otimes \nabla_{\mathbf{x}}\mathbf{N}_i) + (\delta\check{\mathbf{u}}_i \otimes \nabla_{\mathbf{x}}\mathbf{N}_i)^T\right] . \tag{2.6.12}$$

Considering a domain with volume, v, subjected to external forces and displacements on its boundary, Γ, as demonstrated in Fig. 2.7, in the absence of body forces and inertial effects, the principle of virtual work for any arbitrary velocity vector field, $\delta\mathbf{v}$, compatible with all kinematically admissible constraints is expressed as

$$\int_v \sigma : \delta\mathbf{d}dv - \int_\Gamma \mathbf{t}\delta\mathbf{v}d\Gamma = 0\,, \tag{2.6.13}$$

where $\delta\mathbf{d}$ is the virtual strain rate associated with the velocity field $\delta\mathbf{v}$ in

$$\delta\mathbf{d} = \frac{1}{2}(\delta\mathbf{l} + \delta\mathbf{l}^T) \qquad , \qquad \delta\mathbf{l} = \frac{\partial\delta\mathbf{v}}{\partial\mathbf{x}}\,. \tag{2.6.14}$$

By substituting the obtained virtual Eulerian strain in the equilibrium equation, the residual force by neglecting body forces of the system in the current configuration with volume λ and surface $\partial\lambda$ is determined through

$$\mathbf{R}(\check{\mathbf{u}}) = \int_\lambda (\nabla_{\mathbf{x}}\mathbf{N}_i)^T\boldsymbol{\sigma}dV - \int_{\partial\lambda}\mathbf{N}_i\,\mathbf{T}\,dS\,. \tag{2.6.15}$$

As observed, the equation itself is highly nonlinear which needs to be solved also through a numerical method such as the Newton-Raphson procedure to update the displacement

iteratively until the desired precision is reached. Following this technique results in

$$\check{\mathbf{u}}^{n+1} = \check{\mathbf{u}} - \left(\frac{\partial \mathbf{R}}{\partial \check{\mathbf{u}}}\right)_n^{-1} \mathbf{R}_n \tag{2.6.16}$$

and

$$\frac{\partial \mathbf{R}}{\partial \check{\mathbf{u}}} = \int_\lambda (\nabla_{\mathbf{x}} \mathbf{N}_i)^T \mathbf{D} (\nabla_{\mathbf{x}} \mathbf{N}_i)\, dV - \int_{\partial\lambda} (\nabla_{\mathbf{x}} \mathbf{N}_i)^T \otimes \boldsymbol{\sigma} (\nabla_{\mathbf{x}} \mathbf{N}_i)^T\, dS \tag{2.6.17}$$

which defines material stiffness tensor with

$$K_{mat} = \int_\lambda (\nabla_{\mathbf{x}} \mathbf{N}_i)^T \mathbf{D} (\nabla_{\mathbf{x}} \mathbf{N}_i)\, dV \tag{2.6.18}$$

and geometrical stiffness tensor as

$$K_\sigma = \int_{\partial\lambda} (\nabla_{\mathbf{x}} \mathbf{N}_i)^T \otimes \boldsymbol{\sigma} (\nabla_{\mathbf{x}} \mathbf{N}_i)^T\, dS\,. \tag{2.6.19}$$

The material stiffness tensor can appear in the calculations only if the large deformation is considered which indicates the crucial effects of considering this description.

At this point, crystal plasticity approaches are incorporated in order to obtain the relation of the stiffnesses and further implementations in the computational process. By solving the equilibrium equations over a discretized domain, the velocity corresponding to a material point within an element, $\mathbf{v}$ is approximated by the velocity of each integration point, $\hat{\mathbf{v}}_i$ through

$$\mathbf{v} = \sum_{i=1}^{k} N_i \hat{\mathbf{v}}_i\,, \tag{2.6.20}$$

where k is the number of nodes per element, i, and N the interpolation matrix, while

$$\mathbf{F} = \sum_{i=0}^{k} \mathbf{x}_i \otimes \nabla_{\mathbf{X}} N_i \,. \tag{2.6.21}$$

Thus, the velocity gradient is acquired with

$$\mathbf{l} = \sum_{i=1}^{k} \hat{\mathbf{v}}_\mathbf{i} \otimes \nabla_\mathbf{x} N_i = \nabla_{(\xi,\eta,\zeta)} N_i \Big[\sum_{i=1}^{k} \mathbf{x}_\mathbf{i} \otimes \nabla_{(\xi,\eta,\zeta)} N_i \Big] \hat{\mathbf{v}} \,, \tag{2.6.22}$$

where ξ, η, ζ are associated with the local coordinate system. By combining Eq.s 2.6.13, 2.6.14, and 2.6.22 the equilibrium equation becomes a nonlinear relation to be solved via numerical methods by defining the residual force, $\mathbf{R}$, in the current configuration as

$$\mathbf{R}(\hat{\mathbf{v}}) = \int_v (\nabla_x N_i)^T \sigma dv - \int_s N_i \mathbf{t} \delta d\Gamma = 0 \,. \tag{2.6.23}$$

The Newton-Raphson procedure is utilized to solve this nonlinear equation and update the velocity until the desired precision is attained, i.e.,

$$\hat{\mathbf{v}}^{n+1} = \hat{\mathbf{v}}^n - \Big(\frac{\partial \mathbf{R}}{\partial \hat{\mathbf{v}}} \Big)_n^{-1} \mathbf{R} \,, \tag{2.6.24}$$

where

$$\frac{\partial \mathbf{R}}{\partial \hat{\mathbf{v}}} = \underbrace{\int_v (\nabla_x N_i)^T D_{ep} (\nabla_x N_i) dv}_{\text{Material Stiffness}} + \underbrace{\int_v (\nabla_x N_i)^T \sigma \otimes (\nabla_x N_i) dv}_{\text{Geometrical Stiffness}} \,. \tag{2.6.25}$$

The first term of this equation is the material stiffness as a general term appeared in generic finite element methods while the second term is the geometric stiffness that only exists due to the consideration of large deformation. In other words, the approaches using infinitesimal strain methods ignore the significant effects of the geometrical resistance which is the origin of a variety of inconsistencies observed between the results and associated experimental data.

At this point, a constitutive model needs to be incorporated in order to obtain both stiffnesses through the plastic deformation gradient and proceed for further kinetics representations. The next section is dedicated to the discussion of the generic types of constitutive models.

2.7 Constitutive Models in Crystal Plasticity

In general, constitutive models are categorized into two main classes in terms of intrinsic variables; phenomenological and physics-based models. Phenomenological constitutive models are functions of the resolved shear stress introduced as the state variable for each slip system whereas the physics-based constitutive models rely on internal variables including dislocation densities.

2.7.1 Phenomenological Constitutive Models

One of the frequently used models in this category is the power-law model where the flow rule is a function of resolved shear stresses considering loading and hardening parameters for a given slip system [28] which can be stated as

$$\dot{\gamma}^{\alpha} = \dot{\gamma}_0 |\frac{\tau^{\alpha}}{\tau^{\alpha}_{cut}}|^{\frac{1}{m}} \text{sgn}(\tau^{\alpha}) \,, \tag{2.7.1}$$

in which $\dot{\gamma}^{\alpha}$ is the rate of plastic shear strain on the slip system α, τ^{α} the resolved shear stress, τ^{α}_{cut} the orthogonal slip resistance stress, $\dot{\gamma}_0$ the initial plastic strain rate, and m the material constant. τ^{α}_{cut} acts as the hardening factor and is a function of shear strain rate considered instantaneously on all slip systems to reflect self and latent hardening effects, that is,

$$\dot{\tau}^{\alpha}_{cut} = \sum_{\beta=1}^{N} \mathbf{h}_{\alpha\beta} |\dot{\gamma}^{\beta}| \,, \tag{2.7.2}$$

where $\mathbf{h}_{\alpha\beta}$ is the hardening parameter including self, α, and latent, β, hardening specified with

$$\mathbf{h}_{\alpha\beta} = \mathbf{q}_{\alpha\beta}\left[h_0\left(1 - \frac{\tau^{\alpha}_{cut}}{\tau_{sat}}\right)^{a}\right]. \tag{2.7.3}$$

Here, h_0^{β} is the initial hardening parameter, $q^{\alpha\beta}$ a magnitude for self and latent hardening, a a material constant, and τ^{β}_{sat} the saturation shear stress.

2.7.2 Physics-Based Constitutive Models

Physics-based constitutive models, particularly, dislocation density-based models involve internal variables such as dislocation densities. The advanced dislocation density-based constitutive models that consider the evolution of dislocation density followed by the calculation of associated plastic deformation commonly have a functional form of mobile dislocation density in terms of parallel and forest ones. In general, parallel and forest dislocation densities can be computed in terms of statistically stored dislocations or SSDs which evolve from random trapping processes during plastic deformation [29, 30]. The parallel dislocation densities, ρ^{α}_{F}, and forest dislocation densities, ρ^{α}_{P}, can be calculated as a function of statistically stored dislocation densities, ρ_{SSD}, with

$$\rho^{\alpha}_{F} = \sum_{\beta=1}^{N} \chi^{\alpha\beta}\rho^{\alpha}_{SSD}|\cos(n^{\alpha}, t^{\beta})| \tag{2.7.4}$$

and

$$\rho^{\alpha}_{P} = \sum_{\beta=1}^{N} \chi^{\alpha\beta}\rho^{\alpha}_{SSD}|\sin(n^{\alpha}, t^{\beta})|\,, \tag{2.7.5}$$

where n^{α} and $t^{\beta} = (m^{\beta} \times n^{\beta})$ are unit vectors for a given slip system and $\chi^{\alpha\beta}$ is the interaction strength coefficient. These relations, however, can be modified in order to capture size effects. Similar to anisotropy, the size effect cannot be addressed by classical plasticity due

to the lack of associated intrinsic variables. Thereby, CPFEMs are utilized by incorporating the related state variables embedded in the constitutive models in which, the size effect on the strengthening and the evolution of material hardening can be explained through modified dislocation-based descriptions.

Geometrically necessary dislocations (GNDs) appear in strain gradient fields due to geometrical constraints of a crystal lattice. Gradients in the plastic strain due to nonuniform plastic deformation and related size effects such as the presence of lattice curvature and distortions caused by precipitates, interface, and grain boundaries give rise to GND densities in order to maintain continuity and preserve lattice compatibility in a crystal. GNDs do not contribute to plastic strain but act as obstacles to the motion of other dislocations, accordingly, enhance the work hardening of the material. The GND densities are polarized entities accommodating the local plastic strain gradients [25] and can be obtained if the variation of plastic deformation on crystal planes is known. The formulation of GNDs first introduced by Nye [31] and extended by Ashby [32] and Kroner [33] giving a physical basis for strain gradient-dependent material behavior. Dislocation interaction models highlight the increased concentration of dislocations with size shrinkage inherent to the increased inhomogeneous deformation. GNDs are largely concentrated in the grain boundary, interface, and around precipitates where the lattice mismatch is most pronounced and can be calculated from Nye's tensor, Λ, as

$$\Lambda = -\frac{1}{b}\left(\bigtriangledown_X \times \mathbf{F}^{pT}\right)^T \ . \tag{2.7.6}$$

The rate of Nye's tensor can be obtained by summation of the rate of Nye's tensor over each activated slip system through

$$\dot{\Lambda} = \sum_{\alpha=1}^{N} \dot{\Lambda^{\alpha}} \ . \tag{2.7.7}$$

Here, GNDs can be decomposed into three components including one screw, $\dot{\rho}^{\alpha}_{GNDs}$, and two edge parts, tangential, $\dot{\rho}^{\alpha}_{GNDet}$, and normal, $\dot{\rho}^{\alpha}_{GNDen}$, which are derived from the material time derivative of Nye's tensor as

$$\dot{\rho}^{\alpha}_{GNDs} = \frac{1}{b}\left[\bigtriangledown_X \times \left(\dot{\gamma}^{\alpha}\mathbf{F}^{pT}n^{\alpha}\right)\right].m^{\alpha} \tag{2.7.8}$$

$$\dot{\rho}^{\alpha}_{GNDet} = \frac{1}{b}\left[\bigtriangledown_X \times \left(\dot{\gamma}^{\alpha}\mathbf{F}^{pT}n^{\alpha}\right)\right].t^{\alpha} \tag{2.7.9}$$

$$\dot{\rho}^{\alpha}_{GNDen} = \frac{1}{b}\left[\bigtriangledown_X \times \left(\dot{\gamma}^{\alpha}\mathbf{F}^{pT}n^{\alpha}\right)\right].n^{\alpha} \tag{2.7.10}$$

Considering these modifications, the parallel and forest dislocation densities given in Eqs. 2.7.4, 2.7.5 in the presence of GNDs are represented with

$$\begin{aligned}\rho^{\alpha}_{F} =& \sum_{\beta=1}^{N}\chi^{\alpha\beta}[\rho^{\alpha}_{SSD}|\cos(n^{\alpha},t^{\beta})| + \rho^{\alpha}_{GNDs}|\cos(n^{\alpha},m^{\beta})| \\ &+ \rho^{\alpha}_{GNDet}|\cos(n^{\alpha},t^{\beta})| + \rho^{\alpha}_{GNDen}|\cos(n^{\alpha},n^{\beta})|]\end{aligned} \tag{2.7.11}$$

$$\begin{aligned}\rho^{\alpha}_{P} =& \sum_{\beta=1}^{N}\chi^{\alpha\beta}[\rho^{\alpha}_{SSD}|\sin(n^{\alpha},t^{\beta})| + \rho^{\alpha}_{GNDs}|\sin(n^{\alpha},m^{\beta})| \\ &+ \rho^{\alpha}_{GNDet}|\sin(n^{\alpha},t^{\beta})| + \rho^{\alpha}_{GNDen}|\sin(n^{\alpha},n^{\beta})|]\,,\end{aligned} \tag{2.7.12}$$

where $\chi^{\alpha\beta}$ is the interaction strength coefficient. The mobile dislocation density is specified by $\rho^{\alpha}_{m} = c_m\sqrt{\rho^{\alpha}_{F}\,\rho^{\alpha}_{P}}$, where $c_m = \dfrac{c_0 K_B T}{Gb^3}$, with c_0 as a material constant and G shear modulus. Thus, the velocity of mobile dislocations used in Orowan equation will be

$$v^{\alpha} = v_0 \exp\left(-\frac{Q}{k_B T}\right)\sinh\left(\frac{|\tau^{\alpha}| - \tau^{\alpha}_{\text{pass}}}{\tau^{\alpha}_{\text{cut}}}\right)\text{sgn}(\tau^{\alpha}) \quad , \tag{2.7.13}$$

with $v_0 = \dfrac{c_1}{\sqrt{\rho^{\alpha}_{P}\rho^{\alpha}_{F}}}$ as the initial dislocation velocity expressed in terms of parallel and forest dislocation densities. The dislocation velocity depends upon the hardening parameters of passing

and cutting stresses which are determined through

$$\tau^{\alpha}_{\text{pass}} = c_2 Gb\sqrt{\rho^{\alpha}_{P} + \rho^{\alpha}_{F}} \quad , \quad \tau^{\alpha}_{\text{cut}} = \frac{c_3 k_B \theta}{b^2}\sqrt{\rho^{\alpha}_{F}}\,. \tag{2.7.14}$$

Here, c_2 and c_3 are material constants. Contributions to the total slip resistance are due to ρ^{α}_{SSD} including all dislocation mechanisms that can increase or decrease dislocation densities. At low temperature, two increasing mechanisms of lock and dipole formations and one decreasing mechanical of athermal annihilation are recognized. The lock formation is the immobilization of mobile dislocations defined as

$$\dot{\rho}^{\alpha}_{SSD_{lf}} = \frac{c_4}{b}\sqrt{\rho^{\alpha}_{F}}\dot{\gamma}^{\alpha} \tag{2.7.15}$$

and dipole formation with the increasing rate of

$$\dot{\rho}^{\alpha}_{SSD_{df}} = \frac{c_5}{b}\frac{\sqrt{3}Gb}{16\pi(1-\nu)}(|\tau^{\alpha}| - \tau^{\alpha}_{\text{pass}})^{-1}\rho^{\alpha}_{m}\dot{\gamma}^{\alpha}\,. \tag{2.7.16}$$

The athermal annihilation has a decreasing rate due to the interaction of mobile dislocations of one slip system with the immobile dislocations on the same one with the rate of

$$\dot{\rho}^{\alpha}_{SSD_{aa}} = -c_6\rho^{\alpha}_{SSD}\dot{\gamma}^{\alpha}\,. \tag{2.7.17}$$

In these equations c_4, c_5, and c_6 are material constants. Therefore, the rate of the density of SSDs is specified as

$$\dot{\rho}^{\alpha}_{SSD} = \dot{\rho}^{\alpha+}_{SSD_{lf}} + \dot{\rho}^{\alpha+}_{SSD_{df}} + \dot{\rho}^{\alpha-}_{SSD_{aa}} \tag{2.7.18}$$

Ultimately, the mobile dislocation density and the average velocity of glissile dislocations can be obtained for further analyses.

2.8 Crystal Plasticity Large Deformation Finite Element (CPFE)

Considering any type of constitutive models, phenomenological or physics-based, utilized in analytical and computational processes, in order to obtain the stiffness of a system, second Piola-Kirchhoff stress must be determined which is expressed in terms of deformation gradients and material elastic tensor, $\mathscr{C}$, as

$$\mathbf{S}(\tau) = \frac{\mathscr{C}}{2}\left[\mathbf{F}^{p-T}(\tau)\mathbf{F}^{T}(\tau)\mathbf{F}(\tau)\mathbf{F}^{p-1}(\tau) - \mathbf{I}\right]. \tag{2.8.1}$$

With Asaro equation [26], this relation is represented with

$$\begin{aligned}\mathbf{S}(\tau) =& \frac{\mathscr{C}}{2}\Bigg[\sum_{\alpha=1}^{nslip}\left(\mathbf{I} - \Delta\gamma^{\alpha}\left(\mathbf{m}_0^{\alpha}\otimes\mathbf{n}_0^{\alpha}\right)^{T}\right)\mathbf{F}^{p-T}(t)\mathbf{F}^{T}(\tau) \\ & \mathbf{F}(\tau)\mathbf{F}^{-p}(t)\sum_{\alpha=1}^{nslip}\left(\mathbf{I} - \Delta\gamma^{\alpha}\,\mathbf{m}_0^{\alpha}\otimes\mathbf{n}_0^{\alpha}\right) - \mathbf{I}\Bigg],\end{aligned} \tag{2.8.2}$$

where the time increment is defined as $\tau = t + \Delta t$. This relation in terms of the current and next time steps can be written in a general format of elastic and a functional of the second Piola-Kirchhoff stress, respectively, with

$$\mathbf{S}(\tau) = \mathbf{S}_{el} + f(\mathbf{S}(\tau)). \tag{2.8.3}$$

As noted, it is a nonlinear equation that needs to be solved through numerical approaches. Here, by defining unbalanced stress, $\mathbf{G}(\mathbf{S})$, the equation is solved through the following process.

$$\mathbf{G}(\mathbf{S}) = \mathbf{S}(\tau) - \mathbf{S}_{el} + \sum_{\alpha=1}^{nslip}\mathscr{C}^{\alpha}\,\Delta\gamma^{\alpha} \tag{2.8.4}$$

and

$$\mathbf{G}'(\mathbf{S}) = \mathbf{I} + \sum_{\alpha=1}^{nslip}\mathcal{H}(\alpha)\otimes\frac{\partial\Delta\gamma^{\alpha}}{\partial\mathbf{S}(\tau)}, \tag{2.8.5}$$

where

$$\frac{\partial\big(\Delta\gamma^{\alpha}\big)}{\partial\mathbf{S}}=\frac{\partial\big(\Delta\gamma^{\alpha}\big)}{\partial\tau^{\alpha}}\,\frac{\partial\tau^{\alpha}}{\partial\mathbf{S}}=\frac{\partial\big(\Delta\gamma^{\alpha}\big)}{\partial\tau^{\alpha}}\,\left(\mathbf{m}_0^{\alpha}\otimes\mathbf{n}_0^{\alpha}\right), \tag{2.8.6}$$

in which $\mathcal{H}(\alpha)$ is a nonlinear function of slip system, α. Now, by obtaining the plastic deformation gradients, Cauchy stress is achieved which leads to determining the geometrical stiffness in Eq. 2.6.25.

In order to find the material stiffness, the derivative of the Cauchy stress with respect to Lagrangian strain needs to to be obtained through

$$\frac{d\boldsymbol{\sigma}}{d\mathbf{E}}=\frac{1}{\det\mathbf{F}^{e}}\big[\frac{d\mathbf{F}^{e}}{d\mathbf{E}}\mathbf{S}\mathbf{F}^{\mathbf{e}T}+\mathbf{F}^{e}\frac{d\mathbf{S}}{d\mathbf{E}}\mathbf{F}^{\mathbf{e}T}+\mathbf{F}^{e}\mathbf{S}\frac{d\mathbf{F}^{\mathbf{e}T}}{d\mathbf{E}}-(\mathbf{F}^{e}\mathbf{S}\mathbf{F}^{\mathbf{e}T})\,tr(\frac{d\mathbf{F}^{e}}{d\mathbf{E}}\mathbf{F}^{\mathbf{e}-1}\big]\,. \tag{2.8.7}$$

By defining $\mathbf{P}=\frac{\partial\mathbf{F}^{e}}{\partial\mathbf{E}}$ and $\mathbf{Q}=\frac{\partial\mathbf{S}}{\partial\mathbf{E}}$, elastoplastic material stiffness, D_{ep}, is determined as

$$\mathbf{D}_{ep}=\frac{1}{\det\mathbf{F}^{e}}\big[\mathbf{P}\mathbf{S}\mathbf{F}^{\mathbf{e}T}+\mathbf{F}^{e}\mathbf{Q}\mathbf{F}^{\mathbf{e}T}+\mathbf{F}^{e}\mathbf{S}\mathbf{P}-\mathbf{F}^{e}\mathbf{S}\mathbf{F}^{\mathbf{e}T}tr(\mathbf{P}\mathbf{F}^{-1})\big]\,. \tag{2.8.8}$$

At this point, the material stiffness specified in Eq. 2.6.25 is also acquired which leads to a complete process in just a one-time step for each integration point. Taking into account that, at just one-time step, several nonlinear equations must be solved other than the nonlinear system equation through hundreds of iterations and also knowing that thousands of time steps are required to complete the process for each node in a whole domain that contains thousands of elements each with at least eight Gauss points, delineate the astronomical computational workload. Thereby, the public clusters generally do not suffice and another path must be taken to proceed. Consequently, a dedicated cluster is constructed to overcome this barrier as subsequently discussed.

2.9 Dedicated Cluster

Considering the amount of workload in the current study, a horizontal scaling approach is utilized to handle the computational process. The general structure of the cluster has gradually been evolving compatible with the technological availabilities, however, the base structure of the cluster facilitating platform follows a unified approach.

Here, the Kubernetes platform is utilized in order to manage the containers in several aspects including:

- Creating of applications and associated deployments.
- Preserving the operation speed and continuity.
- Floating the container images in the build and release processes.
- Monitoring the health, availability, and operating system level of containers.
- Diversifying running stacks over distributed gates without losing the agility.
- Determining and predicting the efficiency and performance of the possible running process and making decision-based on that

Therefore, the platform stabilizes the network traffic, distributes the required resources proportionally throughout each process among the nodes, and automates the process by replacing more adequate containers than the healing ones for deployments. A schematic structure of the cluster is shown in Fig. 2.8 consisting of one prime and several operative nodes where one operative node is illustrated due to the similarity of the architecture.
The prime node manages the operative nodes with its specific components. The API server is responsible for the general orchestration of the operative nodes through monitoring and enforcing the desired states of applications. The controller part monitors the nodes' current states, captures discrepancies with the application programming interface transports, and resolves the differences. The scheduler segment arranges the timetable via checking and assigning requests from API Server to healthy nodes, assessing nodes qualities and deploying PODs to best-suited nodes, and appointing pending states to proper containers. The key-value store compartments are in charge of storing the desired features and retrieving the image parameters of nodes, points of delivery, and containers.

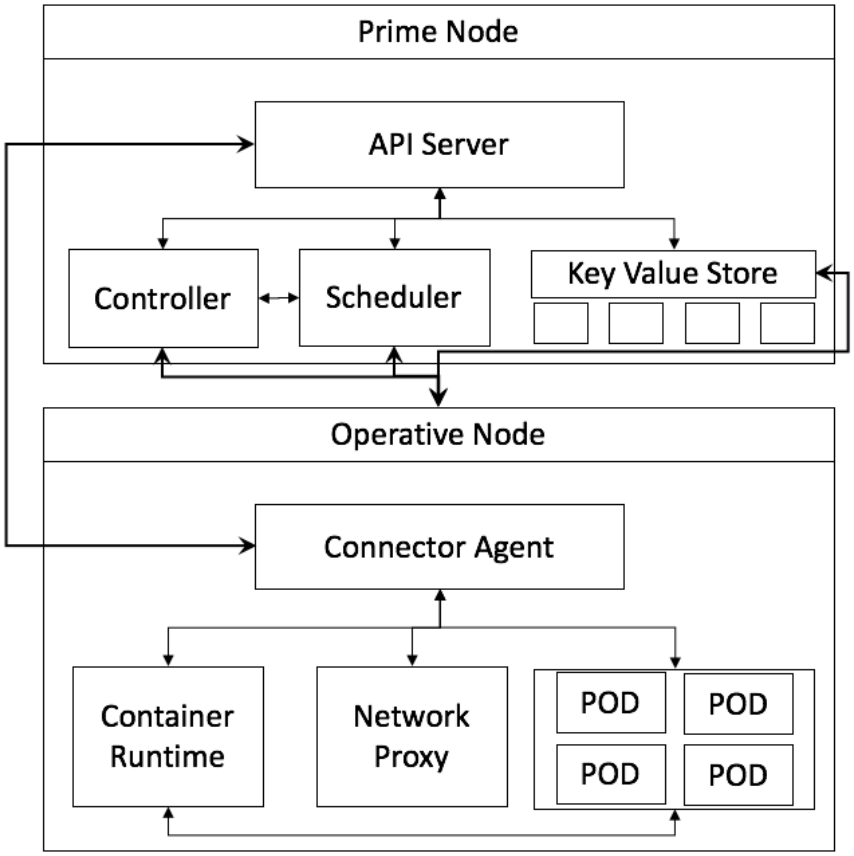

Figure 2.8: A schematic structure of the cluster consisting of one prime and operative nodes. Each segment of the nodes and associated connections are also displayed.

The operative nodes sustain running points of delivery (PODs) and supply the Kubernetes runtime environment through Kubelet as a connector agent of the API server by joining containers, PODs, and tasks to the whole cluster and assessing the task states. The container runtime section is responsible for running containers by starting and ending registry images. The network proxy sector generates internet proxy addresses and handles routing and traffic load-balancing. Finally, PODs are virtual gates illustrating a quality title for each node and directing tasks to healthy nodes.

2.10 Genetic Algorithms

Genetic algorithms (GAs) are stochastic, metaheuristic search approaches based on natural selection and genetics processes in biological evolution for solving both constrained and unconstrained

optimization problems. GA iteratively selects survival of the fittest string at random from the existing data to be parents and creates children for the next generation. Over successive generations through efficiently exploited historical information, the population evolves toward an optimal solution. The procedures of GAs are mostly utilized in circumstances that are not well suited for typical optimization approaches such as optimizing discontinuous, non-differentiable, stochastic, or highly nonlinear objective functions. Genetic algorithms are theoretically and empirically proven to provide robust search in complex spaces [34] with main characteristics of robustness and efficiency-efficacy balance [35].

Extensive applications of GAs in business, science, and engineering fields are due to the computational robustness, at the same time, adequate simplicity of these techniques which are independent of restrictive assumptions in a search space. There are several searching methods to be compared with GAs such as calculus-based and enumerative techniques. Calculus-based methods are inherently localized, highly dependent upon the starting points, and well-defined slope values in capturing the main peak, hence, exhibit extremely limited capabilities in discontinuous, multimodal, and noisy functions. Enumerative schemes are mostly incorporated within a finite or a discretized infinite search space by constantly obtaining objective function values at every point in the space which clearly disqualifies the approach due to the lack of efficiency especially for practical spaces with moderate to large starting data and complexities. Myriad conventional optimization techniques are utilized in vast problems; however, the increase of cases complexities necessitates hybrid combinations and permutations among those methods to the extent that a need for a more vigorous, efficient approach can be sensed.

Utilizing GA is a solution to the all said shortcomings over which optimal points are acquired through enhanced routes with the emphasis on convergence.

GAs are fundamentally different from typical optimization and search procedures in several behaviors as

- Working with the coding of the parameter set, not the parameters themselves;
- Searching from a population of points, not a single point.
- Using objective function information, not derivatives or other auxiliary knowledge;

- Utilizing probabilistic transition rules, not deterministic ones.

GAs start from a rich database and achieve many extremums in parallel using probabilistic transition rules; thus, the possibility of finding a false one is reduced over methods that go point to point. It employs random choice as a tool to guide a search toward regions of the search space with likely improvement [35].

The strings of artificial genetic systems are analogous to chromosomes in biological systems where one or more chromosomes combine to form the total genetic prescription for the construction and operation of some organisms. Accordingly, in an artificial system, a genetic algorithm is composed of three operators, namely, reproduction, crossover, and mutation. In the reproduction process individual decision strings, either numeric or non-numeric, are coded as a binary unsigned integer with weighting functions based on their contribution in the next offspring and the objective function values, f, to be optimized. Strings, S are, commonly, generated over the binary alphabet as $S = s_i; i = 1, 2, ..., l$, considering indicial notation for the length of strings, l. Afterwards, crossover proceeds by randomly matching reproduced strings and producing an integer position, k, along the string arbitrarily between 1 and the string length less one, $[1, l-1]$. Two new strings are created by swapping all characters between positions $k+1$ and l inclusively, as shown in Fig. 2.9.

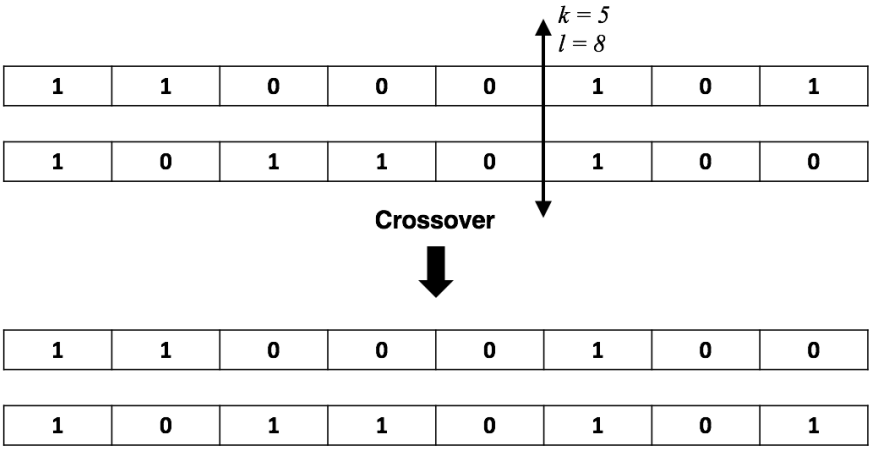

Figure 2.9: Crossover between two reproduced strings where $k = 5$ and $l = 8$.

Finally, the mutation operates at a small rate as a secondary mechanism after crossover. Now, the new population is generated which needs to be decoded into new strings and the whole process is performed until the desirable answer in terms of some tolerances is obtained.

3. CRYSTAL PLASTICITY AND DEEP–LEARNING ALGORITHMS IN MULTI-SCALE ANALYSES AND MODELING OF METALLIC NANO-LAYERS

The majority portions of this chapter have been under consideration in a journal for publication.

3.1 Introduction

Crystalline nano-layers are formed by alternating nanoscale metallic lamellae where the reduction of size to the order of nanometers instigates physicochemical attributes notably depart from those of the bulk counterparts. Metallic nano-systems exhibit exceptional mechanical properties in which the layer size is comparable with the electron or phonon mean free path [36]. Size effects are pivotal aspects in copiously modulated thermodynamically non-equilibrium metallic nano-composites where the rigid body relaxation as the relative translational motion of adjacent crystallites is limited due to the constraints of neighboring nano-phases [37]. The salient, differentiating traits in mechanical responses are assigned to the primary role of layer thicknesses and significant density of interfaces. These features are considered the controlling parameters to modify and modulate the strength and multi-functionality of metallic nano-structures [38] where the dynamic characteristics of the atomic energy with local non-equilibrium multi-valley potentials [39, 20] promote the performances of nano-metals to be governed and altered towards desired applications.

Typically, interfaces function as sources, sinks, and barriers for defects, particularly dislocations. Dislocations, with anisotropic mobility and spreading cores throughout interfaces, describe various aspects of metallic nano-layers physical properties [32, 40] and represent them as tunable structures with remarkable responses in extreme environments [41, 42]. Interfaces of distinct atomic structures supply glissile dislocations into contiguous building blocks throughout inelastic deformation. The reduction of activation volume induce dislocation mechanisms at a shorter distance [43, 44] where the amplified emission of interface dislocations and the onset of plasticity through interphases are of consequence. Reduced strain-hardening results from dislocation nucleation and dynamic annihilation-recovery at interfaces [45, 46]. These occurrences are mostly due to relatively suppressed dislocation densities and substructures leading to the nucleation of individual dislocations at grain boundaries, extension across, and migration into the opposite side [47, 48]. Consider-

able ductility is another attribute caused by non-equilibrium interfaces confining dislocations and blocking sever shear localization [49, 50].

The inverse dependence of strength on grain size refinement in metals and metallic alloys at micro-scale with an average size in the order of micrometers follows the Hall–Petch relation [18, 19] where deformation kinematics encompass dislocation pile-up against interfaces along with other trans-granular dislocation mechanisms. This quality remains intact regardless of synthesizing approaches such as physical vapor deposition (PVD) [51, 52] or accumulative roll bonding (ARB) [53]. However, in nano-scale once the average grain size is reduced to the order of nanometers evincing the participation of a fewer dislocations in a pile-up, the inadequacy of this relation conceivably emerges in a reduced Hall–Petch slope. Instead, it is governed by the Orowan mechanism [21] especially pronounced at heterophase boundaries [54].

Hereby, a more detailed governing relation including the main features of size and constituent effects must be accommodated to analyze metallic nanolamellars responses. In general, these types of models deliver verifiably solid results, however, with complex, nonlinear structures, hence, the elevated cost of computational processes. The multi-scale analysis is sought a proper resolution especially when nonlinearity is involved. In circumstances where size effects are crucial to final assessments, homogenized ensembles inherently possess the governing elements through the variation of the fundamental thermodynamics behaviors including internal energy and entropy that are intrinsically nonlinear and can be statistically generalized on a larger scale. In this sense, capturing temperature effects by homogenization approaches is a significant advantage considering limited experimental results due to a variety of encountered challenges throughout testing. These difficulties include rigorously controlling the atmosphere under which tests are performed to prevent specimens' chemical and microstructural alterations, precise management of thermal gradients between the sample and fixture during the process to avoid thermally misfit deformation and noise in the load and displacement sensors drifting the results, and challenges as such [55, 56].

This work centers on constructing a robust theoretical approach while alleviating computational encumbrance through curtailing partly dependent phenomena into optimized independent variables. The crystal plasticity finite element (CPFE) approach in the large deformation platform is utilized due to the high capacity of analyzing grain interactions, interface abrupt mechanical transitions,

mixed deformation mechanisms, complex boundary conditions, and diverse phenomenological and physics-based constitutive models [22, 23].

The multi-scale computational schemes are pursued leading to the development of multiple governing relations. At the nano-scale, a size-dependent constitutive model and a deep-learning approach named the single layer calibration (SLC) method with the ability to obtain generalized parameters applicable to a broad range of setups are developed. These models simulate, predict, and design the responses of metallic nano-layers in the range of 20 nm to 1 μm with any arbitrary geometrical combinations through a single process. A homogenized crystal plasticity-based model is established with parametric representations of the nano-structural features. The effective functional parameters and associated constants are obtained by metaheuristic genetic algorithms. The model is designed consistent with the nano-model backbone remarkably conducive in simulations of polycrystalline microstructures and significantly expediting computational processes by several (> 4) orders of magnitude, while retaining accuracy. Ultimately, a modified homogenized constitutive model is developed to determine the effects of temperature on the overall responses of metallic nanolamellars. The validation proceeds through the simulation of several copper-niobium, Cu/Nb, nano-layers and comparison with experimental data. Accordingly, the effects of size, loading patterns, layer type, and geometrical combination on overall responses are predicted and discussed. The rest of this work embraces the notion of homogenization in developing expeditious, yet, precise computational approaches to capture mechanical responses of metallic nano-layers under thermo-mechanical loading conditions. The developed size-dependent constitutive model in nano-scale is the explicit representation of the prominent size and constituent effects with the susceptibility of excessive time and energy consumption. The hierarchical framework is incorporated through the homogenization of lower scale reaction functions and development of higher scale constitutive relations. The model reflects the effect of interfaces through the rendition of critical parameters in the hardening laws, specifically, the saturation shear stress and initial hardening parameters. Thereby, a modified homogenized temperature-dependent model is represented with the ability to capture constitutive responses of metallic nanolamellars at ambient as well as elevated temperatures for which the model parameters are obtained for Cu/Nb cases and favorably verified with experimental results. In the end, multiple demonstrations of temperature effects on the said specimens are

analyzed and discussed.

The developed nano-scale size-dependent constitutive model, the deep-learning single layer calibration method, homogenized constitutive model, temperature-dependent constitutive model, numerical solvers, and process optimizers are implemented through three-dimensional crystal plasticity nonlinear finite element codes in the large deformation platform. A dedicated supervised cluster has been constructed with specific architecture and orchestration policies compatible with the current data processing and workloads.

3.2 Plastic Deformation Kinematics

Considering large plastic deformation in metallics nano-composites, finite strain kinematics are accommodated through a multiplicative decomposition of total deformation gradient, $\mathbf{F}$, into the elastic, $\mathbf{F}^e$, and plastic, $\mathbf{F}^p$, parts as

$$\mathbf{F} = \mathbf{F}^e\mathbf{F}^p \,. \tag{3.2.1}$$

The deformation gradient, $\mathbf{F} = \nabla_x X$, maps material tangent vectors, $\mathbf{X}$, into spatial ones, $\mathbf{x}$, with the quality of a two-point tensor involving points in two distinct configurations. $\mathbf{F}^p$ represents crystallographic slip in a relaxed, intermediate configuration where the lattice is in its reference orientation and $\mathbf{F}^e$ designates elastic distortion and rigid body rotation.
The rate dependence is manifested in the rate of the deformation gradient, $\dot{\mathbf{F}}$, through the velocity gradient,

$$\mathbf{l} = \dot{\mathbf{F}}\mathbf{F}^{-1} \,. \tag{3.2.2}$$

The plastic velocity gradient,

$$\mathbf{l}^p = \dot{\mathbf{F}^p}\mathbf{F}^{-p} \,, \tag{3.2.3}$$

involving plastic shear strain rate, $\dot{\gamma}^{\alpha}$, on the slip systems, α, [26, 28], specified with

$$\mathbf{l}^{p} = \sum_{\alpha=1}^{N} \dot{\gamma}^{\alpha} \mathbf{s}_{0}^{\alpha} \,, \tag{3.2.4}$$

are utilized to solve the indeterminate equation of $\mathbf{F} = \mathbf{F}^{e}\mathbf{F}^{p}$, where $s_{0}^{\alpha} = m_{0}^{\alpha} \otimes n_{0}^{\alpha}$ is the Schmid tensor in which m_{0}^{α} and n_{0}^{α} are the slip direction and normal, respectively.
The plastic shear strain rate for each slip system is calculated through the Orowan equation [27],

$$\dot{\gamma}^{\alpha} = \rho_{m}^{\alpha}\, b\, v^{\alpha} \,, \tag{3.2.5}$$

where ρ_{m}^{α} is the mobile dislocation density, b the Burgers vector, and v^{α} the average mobile dislocation velocity. The integration of $\dot{\mathbf{F}}^{p}$ determines $\mathbf{F}^{p}$ and, accordingly, $\mathbf{F^{e}}$ through $\mathbf{F^{e}} = \mathbf{F}\mathbf{F}^{-\mathbf{p}}$ which yields the second Piola-Kirchhoff stress, $\mathbf{S}$, in terms of Lagrangian strain,

$$\mathbf{E} = \frac{1}{2}(\mathbf{F}^{eT}\mathbf{F}^{e} - \mathbf{I}) \,, \tag{3.2.6}$$

and the anisotropic material elastic tensor, $\mathscr{C}$, with $\mathbf{S} = \mathscr{C}\mathbf{E}$.
Solving the equilibrium equation in the current configuration requires the calculation of Cauchy stress,

$$\boldsymbol{\sigma} = \frac{1}{|\mathbf{F}^{e}|}\mathbf{F}^{e}\mathbf{S}\mathbf{F}^{eT} \,, \tag{3.2.7}$$

and its derivative with respect to true strain to obtain the system stiffness. This relation holds due to plastic incompressibility, i.e., $\det\mathbf{F}^{p} = 1$. A constitutive model must be incorporated to acquire $\mathbf{F}^{p}$ and further kinetics representations. The next section describes the rationale behind the proposed constitutive model.

3.3 Entropic Kinetics and Constitutive Model in Nano-Scale

Considering metals and metallic alloys with nanoscale size under generic loading conditions, stress- and temperature-driven interface and surface evolution phenomena bear significance in me-

chanical responses. Dislocation-mediated deformations are entropy sources compelling a system towards a higher probability state independent of ordinary thermal fluctuations. Thus, a system kinematics must encompass dislocation-specific thermodynamics representation [57, 58].

Assuming quasi-static transitions in all configurations, the contributions due to total dynamic quantities are negligible, however, the system is not necessarily in thermodynamic equilibrium. Total entropy generation per unit time, $\Gamma(t)$, as the difference between the reference rate of change of entropy, $\dot{\mathcal{S}} = \frac{D\mathcal{S}}{Dt}$, and the rate of entropy input, $\dot{\mathcal{Q}}$, of a body with volume, Λ, and boundary surface, $\partial\Lambda$, follows the global format in the reference configuration with

$$\Gamma(t) = \frac{D\mathcal{S}}{Dt} - \dot{\mathcal{Q}} = \frac{D}{Dt}\int_{\Lambda} \eta(\lambda, t)\, dv + \int_{\partial\Lambda} \mathbf{H}(\lambda, t)\cdot \mathbf{n}\, ds - \int_{\Lambda} \mathbf{R}(\lambda, t)\, dv \geq 0\,, \tag{3.3.1}$$

and then

$$\Gamma(t) = \frac{D}{Dt}\int_{\Lambda} \eta(\lambda, t)\, dv + \int_{\partial\Lambda} \frac{\mathbf{Q}(\lambda, t)}{\Theta(\lambda, t)}\cdot \mathbf{n}\, ds - \int_{\Lambda} \frac{\mathbf{R}(\lambda, t)}{\Theta(\lambda, t)}\, dv \geq 0\,, \tag{3.3.2}$$

where $\eta(\lambda, t)$ is the entropy per unit volume as a function of material position vector, λ, and time, t, $\mathbf{H}(\lambda, t)$ the true entropy flux, $\mathbf{Q}(\lambda, t)$ the material heat flux, $\mathbf{n}$ the normal boundary surface vector, $\Theta(\lambda, t)$ the thermal scalar field, and $\mathbf{R}(\lambda, t)$ the entropy source. Since the rate of entropy change is always greater than the rate of entropy input, the total entropy generation is time- and direction-dependent specifying the irreversibility of thermodynamic processes [59, 60] including plastic deformation. The rate of thermal work involving the total heat flux and source is inversely related to the rate of entropy input through the thermal scalar field and first Piola-Kirchhoff stress, $\mathbf{P}(\lambda, t)$. Based on the divergence theorem, $\int_s \Psi\mathbf{v}\cdot\mathbf{n}ds = \int_v \nabla\cdot(\Psi\mathbf{v})dv$, the local form of the entropy inequality can be expressed as

$$\dot{\eta}(\lambda, t) - \frac{\mathbf{R}(\lambda, t)}{\Theta(\lambda, t)} + \frac{1}{\Theta(\lambda, t)}\nabla\cdot\mathbf{Q}(\lambda, t) - \frac{1}{\Theta^2(\lambda, t)}\mathbf{Q}(\lambda, t)\cdot\nabla\Theta(\lambda, t) \geq 0\,, \tag{3.3.3}$$

and

$$\Theta(\lambda, t)\,\dot{\eta}(\lambda, t) \; + \frac{1}{\Theta(\lambda, t)}\mathbf{Q}(\lambda, t)\cdot\nabla\Theta(\lambda, t) + \mathbf{P}(\lambda, t) : \dot{\mathbf{F}} - \dot{\mathfrak{e}} \geq 0\,, \tag{3.3.4}$$

in which the local form of balance of energy,

$$\dot{\mathfrak{e}} = \mathbf{P}(\lambda, t) : \dot{\mathbf{F}} - \nabla \cdot \mathbf{Q}(\lambda, t) + \mathbf{R}(\lambda, t) \,, \tag{3.3.5}$$

is considered, where ∇ is the differential operator. The heat conduction inequality,

$$\mathbf{Q}(\lambda, t) \cdot \nabla\Theta(\lambda, t) \leq 0 \,, \tag{3.3.6}$$

applies a constraint on the heat flux vector, i.e., there is no heat flux without a temperature. For elastoplastic behavior of a crystal, the local entropy production, Υ_{in}, is positive or at least zero where heat flux approaches to zero in reversible processes, i.e.,

$$\Upsilon_{in} = \mathbf{P}(\lambda, \mathbf{t}) : \dot{\mathbf{F}} - \dot{\mathfrak{e}} + \Theta(\lambda, t)\, \dot{\eta}(\lambda, t) \geq 0 \,. \tag{3.3.7}$$

Therefore, the internal dissipation stems from three sources; the rate of internal mechanical work per unit volume, the rate of internal energy, and the absolute temperature coupled with the rate of entropy, respectively. With the aid of the balance of energy, the lower bound of Eq. 3.3.7 can be represented by

$$\Theta(\lambda, t)\, \dot{\eta}(\lambda, t) = \Upsilon_{in} + \mathbf{R}(\lambda, t) - \nabla \cdot \mathbf{Q} \,. \tag{3.3.8}$$

The constitutive relation $\mathbf{Q}(\lambda, t) = \varkappa \nabla\Theta(\lambda, t)$ relates the the material heat flux to the temperature gradient with thermal conductivity, $\varkappa$, as a function of deformation and temperature where $\varkappa\nabla^2\Theta(\lambda, t) \geq 0$ signifying the elliptical nature of the equation for which the solutions are accordingly to be realized. For an adiabatic thermodynamic process, $P_{(a)}$, the thermal power and the rate of entropy input are zero since thermal energy can not traverse the system boundary surfaces, be generated, or destroyed. In this circumstance, no decay in the total entropy is possible while that is not the case for point-wise entropy that degenerates the energy balance equation and annihilates

that for an additional reversibility condition, $P_{(a,r)}$ [61].

$$\begin{cases} \Theta(\lambda,t)\dot{\eta} = \Upsilon_{in} & ; \ P_{(a)} \\ \Theta(\lambda,t)\dot{\eta} = 0 & ; \ P_{(a,r)} \end{cases} \tag{3.3.9}$$

Considering the anisotropic elastoplastic behavior of crystalline materials, internal variables need to be independently assimilated in any thermodynamical approaches, hence, the Helmholtz free-energy function, $\mathscr{H}(\mathbf{F},\Theta(\lambda,t),\mathscr{V}_i)$, is defined as a function of deformation gradient, thermal field, and internal variables, $\mathscr{V}_i; i = 1,...,n$, respectively. Here, $\mathscr{V}_i$ represents plastic deformation mechanisms, associated with any admissible inelastic phenomena, n, for presumed external thermomechanical loading conditions. Thus, the Helmholtz free-energy function can be described in terms of the internal dissipation inequality as

$$\Upsilon_{in} = \mathbf{P}(\lambda,\mathbf{t}) : \dot{\mathbf{F}} - \dot{\mathscr{H}}(\mathbf{F},\Theta(\lambda,t),\mathscr{V}_i) - \dot{\Theta}(\lambda,t)\,\eta(\lambda,t),\mathscr{V}_i) \geq 0\,, \tag{3.3.10}$$

where the chain rule time differentiation of the Helmholtz free-energy function yields

$$\begin{aligned} \dot{\mathscr{H}}(\mathbf{F},\Theta(\lambda,t),\mathscr{V}_i) = &\left(\frac{\partial\mathscr{H}(\mathbf{F},\Theta(\lambda,t),\mathscr{V}_i)}{\partial\mathbf{F}}\right)_{\Theta,\mathscr{V}_i} : \mathbf{F} + \left(\frac{\partial\mathscr{H}(\mathbf{F},\Theta(\lambda,t),\mathscr{V}_i)}{\partial\Theta}\right)_{\mathbf{F},\mathscr{V}_i} \dot{\Theta}(\lambda,t) \\ &+ \sum_{i=1}^{n}\left(\frac{\partial\mathscr{H}(\mathbf{F},\Theta(\lambda,t),\mathscr{V}_i)}{\partial\mathscr{V}_i}\right)_{\mathbf{F},\Theta} : \dot{\mathscr{V}}_i \ . \end{aligned} \tag{3.3.11}$$

The acquired constitutive equation involves stress, thermal flux, and internal entropy associated with plastic deformations through internal strain rates, $\dot{\mathscr{V}}_i$, for which

$$\Upsilon_{in} = \sum_{i=1}^{n} \mathscr{D}_i : \dot{\mathscr{V}}_i \geq 0 \ \ ; \ \ \mathscr{D}_i = -\left(\frac{\partial\mathscr{H}_i(\mathbf{F},\Theta(\lambda,t),\mathscr{V}_i)}{\partial\mathscr{V}_i}\right)_{\mathbf{F},\Theta}\,, \tag{3.3.12}$$

is deduced in terms of internal dissipations, $\mathscr{D}_i$. For the stretch type deformation, compatible with dislocation mechanisms, considering symmetric internal variables, $\mathscr{U}_i$, and stretch tensor, $\mathbf{C}$,

Eq. 3.3.12 becomes

$$\sum_{i=1}^{n} \frac{\partial \mathscr{H}_i(\mathbf{C}, \Theta(\lambda, t), \mathscr{U}_i)}{\partial \mathscr{U}_i} : \dot{\mathscr{U}}_i \leq 0 \,, \tag{3.3.13}$$

where the rate of the symmetric internal variables, $\dot{\mathscr{U}}_i$, evolves in irreversible mechanisms with a designated function, $\mathscr{E}$, through

$$\dot{\mathscr{D}}_i = \mathscr{E}(\mathbf{C}, \Theta(\lambda, t), \mathscr{U}_1, \mathscr{U}_2, ..., \mathscr{U}_n) \,. \tag{3.3.14}$$

The second Piola-Kirchhoff stress, $\mathbf{S}$, is involved in the evolution equations due to its dependence on the free energies of either reversible or irreversible processes which represents that as a function of external variables as

$$\mathbf{S} = \mathscr{S}(\mathbf{C}, \Theta(\lambda, t)) \,. \tag{3.3.15}$$

The internal states of disorder in a crystalline solid contain the majority of barriers including point defects, grain boundaries, junctions, intersections, locks, stacking faults, or combinations of those in dislocation dynamic annihilations and recoveries [58]. The average velocity of dislocations, v_d, and the time spent between obstacles, t_d, both are functions of applied stress, τ, and absolute temperature, T, which define the dislocation mean free path with

$$l_d = t_d(\tau, T)\, v_d(\tau, T) \,. \tag{3.3.16}$$

The probability function indicating the possible states of slip due to thermal fluctuation and applied loading is

$$\mathscr{P}_s = \exp\left(-\frac{\Delta \mathscr{G}}{k_B T}\right) \,, \tag{3.3.17}$$

where $\Delta\mathscr{G}$ is the activation free enthalpy and k_B the Boltzmann constant. If a dislocation is effectively vibrating with the frequency of f_d, it successfully overcomes barriers at a rate of

$$\dot{\mathscr{P}}_s = f_d \exp\left(-\frac{\Delta\mathscr{G}}{k_B T}\right) , \tag{3.3.18}$$

therefore, the dislocation velocity associated with the mean free path for each conquered obstacle with the presence of thermal fluctuation will be

$$v_d = l_d f_d \left[\exp\left(-\frac{\Delta\mathscr{G}}{k_B T}\right)\right] . \tag{3.3.19}$$

The dependence of flow strength on temperature and applied stress is determined based on the required energy to overcome any types of barriers while dislocations slip. In a general nonlinear temperature-dependent case it can be demonstrated in terms of the Helmholtz free energy as

$$\Delta\mathscr{G} = \Delta\mathscr{H}\left[1 - \left(\frac{|\tau^\alpha| - \tau_r^{\parallel}}{\tau_r^{\perp}}\right)^p\right]^q , \tag{3.3.20}$$

where τ^α is the resolved shear stress and $\tau_r^{\parallel}$ and $\tau_r^{\perp}$ are the resistance stresses parallel and orthogonal to slip surface, respectively. The exponents, p and q, can be initially identified with mechanistic assessments and finalized through calibration processes. The rate of Helmholtz energy in Eq. 3.3.11 is a function of external and internal dissipative variables. Consequently, the energy needed to overcome hinderances is manifested in deformation mechanisms controlled by thermal activation and applied loading [62, 63]. Considering the alternating directions of dislocation motion over an obstacle, thermally activated plastic shear strain rate for each slip system can be expressed as

$$\dot{\gamma} = \rho_m^\alpha \, b \, l_d^\alpha \, f_d^\alpha \sinh\left(-\frac{V_a}{k_B T}(|\tau^\alpha| - \tau_r^{\parallel})\right) \exp\left(-\frac{\Delta\mathscr{H}}{k_B T}\right) , \tag{3.3.21}$$

where V_a is the activation volume and b the Burgers vector. The pre-exponential terms can be merged into the initial plastic strain rate, $\dot{\gamma}_0^\alpha = \rho_m^\alpha b l_d^\alpha f_d^\alpha = \rho_m^\alpha b^2 f_D$, where f_D denotes the Debye frequency of constituents. This term is considered a slow variable since the change of mobile dislocation density is not decisive relative to that of free energy, yet, not completely uneventful.

The obstacles surmounted by thermal energy and mechanical work are described [57] by

$$(|\tau^{\alpha}| - \tau_r^{\|})\, V_a\,. \tag{3.3.22}$$

In metals with nano-range sizes, activation volumes decline significantly due to diminished local volumes involved in the depinning of a propagating dislocation [64], thermally activated mechanism generating interface mediated dislocations [65], and so forth. Thereby, considering an increase in a system entropy due to thermal fluctuations, internal and external state variables, statistical probabilities of dislocation positions, and unidirectional dislocation jumps, a constitutive model is developed at the size spectrum of 20 nm to 1 μm encapsulating size and constituent effects in abrupt variations of activation volumes, stress concentration, and complex dislocation mechanisms with

$$\dot{\gamma}^{\alpha} = \begin{cases} \dot{\gamma}_0^{\alpha} \exp\left\{-\frac{Q_{active}}{k_B T}\left[1 - \left(\frac{(\tau_{\text{eff}}^{\alpha})^2}{\tau_{\text{cut}}^{\alpha}} \frac{c_s \pi}{\mu b}\, d\right)^{p}\right]^{q}\right\} \operatorname{sgn}(\tau^{\alpha}) & \tau_{\text{eff}}^{\alpha} > 0 \\ 0 & \tau_{\text{eff}}^{\alpha} \leq 0 \end{cases} \tag{3.3.23}$$

The model is constructed based on exclusively addressing size effects in d as the layer thickness and the constituent type and morphology through c_s as the material shape parameter. The effective shear stress is defined as $\tau_{\text{eff}}^{\alpha} = |\tau^{\alpha}| - \tau_{\text{pass}}^{\alpha}$, where passing, $\tau_{\text{pass}}^{\alpha}$, and cutting, $\tau_{\text{cut}}^{\alpha}$, stresses are athermal and thermal shear resistances, respectively, Q_{active} is the activation energy, and μ the shear modulus. Long-range athermal resistances stem from the composition, heat treatment, and dislocation structure of the material including the stress fields of other dislocations and incoherent inclusions, while short-range thermal barriers involve sources such as the Peierls-Nabarro force, stress fields of coherent inclusions, cross slip, climb, and dislocations intersections. Plasticity initiation is recognized when the effective shear stress is positive while elastic behavior is resumed otherwise. The athermal resistance is designed with an evolution in terms of contrasting slip systems, β, by

$$\dot{\tau}_{pass}^{\alpha} = \sum_{\beta=1}^{N} \mathbf{h}^{\alpha\beta} |\dot{\gamma}^{\beta}|\,, \tag{3.3.24}$$

where $\dot{\gamma}^{\beta}$ specifies the effect of other N slip systems and $\mathbf{h}^{\alpha\beta}$ includes both self and latent hardening with

$$\mathbf{h}^{\alpha\beta} = \begin{cases} \sum_{\beta=1}^{N} h_0^{\beta} \left| 1 - \dfrac{\left|\left|\tau_{cut}^{\beta} + \tau_{pass}^{\beta}\right|\right|_2}{\tau_{sat}^{\beta}} \right|^{r} \left[q^{\alpha\beta} + (1 - q^{\alpha\beta})\delta^{\alpha\beta} \right] & \left|\left|\tau_{cut}^{\beta} + \tau_{pass}^{\beta}\right|\right|_2 \leq \tau_{sat}^{\beta} \\ 0 & \left|\left|\tau_{cut}^{\beta} + \tau_{pass}^{\beta}\right|\right|_2 > \tau_{sat}^{\beta} \end{cases} \tag{3.3.25}$$

in which $|| \, x \, ||_2$ denotes the Euclidean norm, h_0^{β} is the initial hardening, $q^{\alpha\beta}$ a magnitude for self and latent hardening considered 1.0 for coplanar slip systems and 1.4 otherwise, r the hardening exponent, and $\delta^{\alpha\beta}$ the slip systems Kronecker delta function. τ_{sat}^{β} is the saturation shear stress defined as $\tau_{sat} = c_{sat}\, d^{m}$ where c_{sat} and m are the saturation coefficient and exponent, respectively. In order to utilize the constitutive model in crystal plasticity procedures and solve system equations, derivation techniques and computational approaches are required to be carried out as delineated in appendices A and B. Inevitably, multiple parameters in the model must be realized before any further analysis for which the next section is assigned.

3.4 Deep-Learning Single Layer Calibration (SLC) Method

In order to acquire constitutive parameters a deep-learning single-layer calibration (SLC) method is developed. This technique is able to reduce the experimental data, recognize and distinguish dominant and trivial patterns, and efficiently decide trade-offs between bias and variance paths along with some other optimization, recognition, and decision capabilities. In the following section, deep-learning algorithms utilized to classify the acquired data from computational processes and allocate the most compatible paths to the acquired values are demonstrated. Subsequently, the application of the SLC method in the parameter calibration of Cu/Nb nano-layers is evinced.

3.4.1 Training and Learning Techniques in The SLC Approach

This approach is based on adaptive boosting technique [66] over a committee of models. The operation proceeds through combining classifiers, $M_j \; ; \; j = 1, 2, ..., m$, by sequentially training n models and concluding the final prediction based on the ultimate outcome. One of the main

advantages of this procedure is obtaining favorable results even if the base classifiers are not strong learners. However, the possibility of achieving solid outcomes exponentially increases in the cases of moderate or advanced classifiers that are believed characterizes the current work features. Boosting can be extended to regression problems [67] which in some optimization stages is employed as well. The classifiers are trained using a weighted array in which the coefficient values depend on the performances of the previous classifiers. The descending sorted coefficients are proportional to the level of the misclassification of data and are key in the final decision. At the beginning, each of n weighting coefficient, $c_w^{(i)}$, in the array is uniformly initialized based on the data point vectors, $\mathbf{v}_i$, and binary target values, $t_i \in \{-1, 1\}$, $i = 1, 2, .., n$, among the classifiers as $c_w^{(i)(j)} = \frac{1}{n}$. Then, each model is trained while the associated weighted error function,

$$e_j = \sum_{i=1}^{n} c_w^{(i)(j)} \mathcal{N}(M_j(\mathbf{v}_i) \neq t_n) \,, \tag{3.4.1}$$

is minimized, where

$$\mathcal{N}(M_j(\mathbf{v}_i), t_n) = \begin{cases} 1 & M_j(\mathbf{v}_i) \neq t_n \\ \\ 0 & M_j(\mathbf{v}_i) = t_n \end{cases} \tag{3.4.2}$$

is the indicator function. After training the first classifier, $M_1(\mathbf{v}_i)$, weighting coefficients are continuously adjusted for succeeding models by a modifier,

$$\psi_j = \left(\frac{1 - \sum_{i=1}^{n} c_w^{(i)(j)} \mathcal{N}(M_j(\mathbf{v}_i) \neq t_n)}{\sum_{i=1}^{n} c_w^{(i)(j)}} \right) \,, \tag{3.4.3}$$

allocating larger weighting values to more precise classifiers and updates the weighting coefficient array by

$$c_w^{(i+1)(j)} = c_w^{(i)(j)} \left(\frac{\sum_{i=1}^{n} c_w^{(i)(j)}}{\sum_{i=1}^{n} c_w^{(i)(j)} \mathcal{N}(M_j(\mathbf{v}_i) \neq t_n)} - 1 \right)^{\mathcal{N}(M_j(\mathbf{v}_i) \neq t_n)} \,. \tag{3.4.4}$$

The exponential error function [68] is defined as

$$\mathcal{E} = \frac{1}{2} \sum_{i=1}^{n} \sum_{j=1}^{m} \exp\left[-t_i \psi_j M_j(\mathbf{v}_i)\right] \ , \tag{3.4.5}$$

which is sequentially minimized in terms of ψ_j and $M_j(\mathbf{v}_i)$. This relation holds with the assumptions of fixed base classifiers and their modifiers. The boosting framework is illustrated schematically in Fig. 3.1 where each base classifier is trained according to the assigned weighted function acquired in terms of the precision of previous classifiers in data allocation with the error function between two consecutive classifiers as

$$\mathcal{E} = \sum_{i=1}^{n} \sum_{j=1}^{m} \exp\left(-\frac{1}{2}\left[t_i \psi_{j-1} M_{j-1}(\mathbf{v}_i) - t_i \psi_j M_j(\mathbf{v}_i)\right]\right). \tag{3.4.6}$$

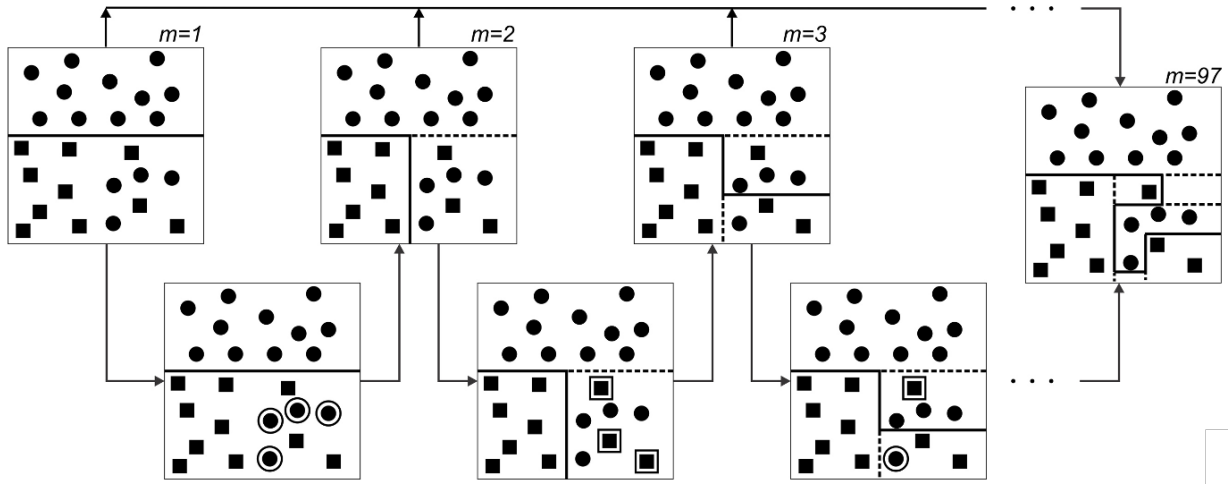

Figure 3.1: Demonstration of adaptive boosting technique where base classifiers with simple thresholds are trained according to the assigned weighted function acquired relative to the precision of the previous classifier in data allocation. Each sample shows the number of classifiers, m, trained up to that point. The solid and dashed lines in the domains are the the decision made and revised choices, respectively, based on the weight of the misplaced data illustrated with expanded boundaries.

If data points are divided into proper, C_j^+, and improper, C_j^-, categories, Eq. 3.4.6 can be specified by

$$\mathcal{E} = \sqrt{\psi_j - 1} \sum_{i \in C_j^+} c_w^{(i)(j)} + \sqrt{\frac{1}{\psi_j} - 1} \sum_{i \in C_j^-} c_w^{(i)(j)} \,, \tag{3.4.7}$$

and accordingly with

$$\mathcal{E} = \left(\sqrt{\psi_j - 1} - \sqrt{\frac{1}{\psi_j} - 1} \right) \sum_{i=1}^{n} c_w^{(i)(j)} \mathcal{N}(M_j(\mathbf{v}_i) \neq t_n) + \sqrt{\frac{1}{\psi_j} - 1} \sum_{i=1}^{n} c_w^{(i)(j)} \,. \tag{3.4.8}$$

Thus, from Eqs. 3.4.6 , 3.4.8 and

$$t_i M_j(\mathbf{v}_i) = 1 - 2\mathcal{N}(M_j(\mathbf{v}_i) \neq t_n) \,, \tag{3.4.9}$$

weighting coefficients are modified as

$$c_w^{(i+1)(j)} = c_w^{(i)(j)} \exp\left(-\frac{1}{2} t_i \psi_j M_j(\mathbf{v}_i) \right) = c_w^{(i)(j)} \sqrt{\psi_j - 1} \left(\frac{1}{\psi_j} - 1 \right)^{\frac{\mathcal{N}(M_j(\mathbf{v}_i) \neq t_n)}{2}} \,. \tag{3.4.10}$$

Finally, when the training of the classifiers are completed, the sign of the combined function for each data point vector is obtained with

$$\mathrm{SGN}(\mathbf{v}_i) = \mathrm{sgn}\left[M_j(\mathbf{v}_i) \, \ln\left(\frac{\sum_{j=1}^{m} c_w^{(i)(j)}}{\sum_{i=1}^{n} c_w^{(i)(j)} \mathcal{N}(M_j(\mathbf{v}_i) \neq t_n)} - 1 \right) \right] . \tag{3.4.11}$$

3.4.2 Application of The SLC Approach

The presented deep-learning SLC approach utilizes the single crystal stress-strain curve of each constituent and delivers generalized parameters via a single process applicable to a broad scope of setups that are entirely different than those of the calibration ones.

Here, several Cu and Nb nano-layers are separately simulated for which elastic constants are Initially obtained through analytical processes and databases displayed in Table 5.2.

Table 3.1: Material constants of copper and niobium acquired from analytical processes and databases.

Material Elastic Constants	Cu	Nb
C_{11}(GPa)	168.4	246.0
C_{12}(GPa)	121.4	134.0
C_{44}(GPa)	75.4	28.7
μ(GPa)	48.0	38.0
Q_{active}(J)	$8.05e{-19}$	$8.9e{-19}$
b(m)	$2.56e{-10}$	$2.86e{-10}$

Subsequently, the constitutive parameters are obtained, Table 3.2, via experimental data of single crystalline Cu [6] and Nb [69].

Table 3.2: Material constants of copper and niobium acquired from analytical processes and databases.

Material Parameters	Cu	Nb
$\dot{\gamma}_0^\alpha$	5.0e6	6.0e6
p	0.98	1.01
q	1.12	1.14
r	1.115	1.121
c_s	0.2	0.002
c_{sat}	70,000.0	76,741.0
m	-0.50	-0.50
τ^α_{cut}(MPa)	4.80	6.30
$\tau^\alpha_{\text{pass-init}}$(MPa)	5.20	7.10
h_0^β (MPa)	3,000.0	20,000.0

To illustrate the capabilities of the developed models in generic perspectives, sequential modeling steps from an actual metallic nano-layer image to a three-dimensional Cu/Nb nano-layer unit cell discretized into hexahedral elements are demonstrated in Fig. 3.2. The simulation is performed utilizing the parameters in Table 3.2.

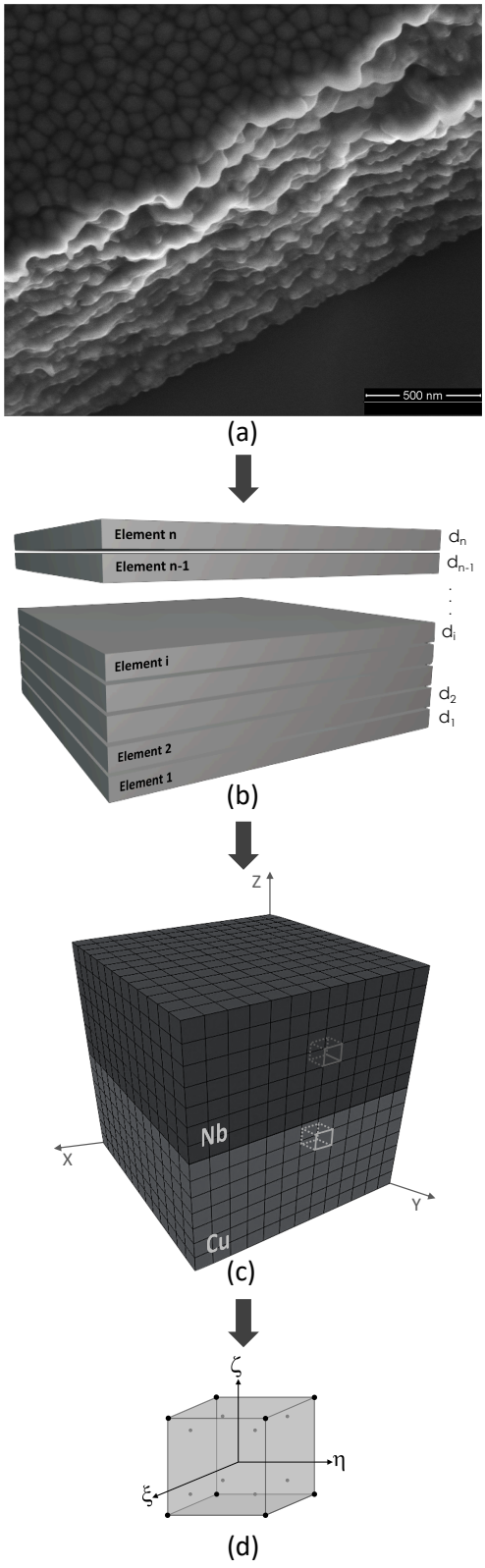

Figure 3.2: (a) A high resolution scanning electron microscopy image of a metallic nano-layer. (b) A generalized representative structure of a metallic nano-layer with n elements/layers. (c) A 3-dimensional Cu/Nb nano-layer unit cell discretized into (d) hexahedral elements.

The responses of the specimens in the form of true stress-strain curves are compared with the experimental results in [8, 1], Fig. 3.3, having entirely different setups than those of the calibrations in [6, 69]. The engineering stress-strain curves in [8] are obtained for the average layer thicknesses of 16 nm, 34 nm, and 63 nm under the constant strain rate of $10^{-3}/sec$ while a true stress-strain curve is achieved in [1] involving the average layer thickness of 40 nm with $2 \times 10^{-4}/sec$ strain rate. The experimental and simulations are performed with the Kurdjumov-Sachs (KS) orientation relationships, {111}Cu||{110}Nb.

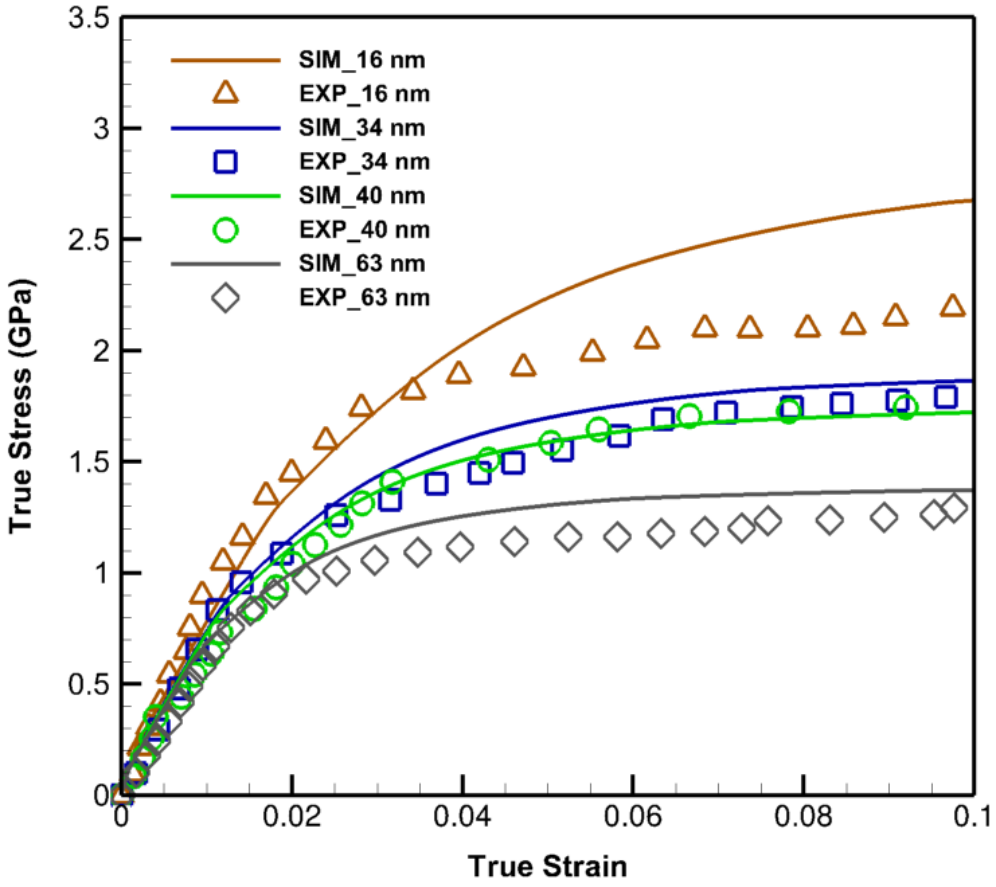

Figure 3.3: The verification of the size-dependent constitutive model and deep-learning SLC results plotted by "SIM" and solid lines with the experimental data [8, 1] designated by "EXP" and symbolic points.

Since the developed models yield true stress-strain responses, an excellent agreement with 40 nm experimental data is observed due to the similarity of formats. Small divergences between the rest of the curves are related to the nature of the reported results, being engineering stress-strain,

which naturally placed them in the lower positions than the true ones. The general trend of the computationally predicted properties is in agreement with the experimental data, however, the amount of deviation from 16 nm is related to the softening phenomenon at the sizes lower than about 20 nm [70, 71] due to which this work is appointed its nano-scale size range from 20 nm to 1 μm.

3.5 Nano-scale Results and Discussions

In this section, further analyses are performed on Cu/Nb nano-layers under the strain rate of $10^{-3}/sec$ and the KS orientation relationships.

Emphasizing the size and geometrical effects, four thickness combinations of 34 nm and 63 nm along with their uniform average thickness of 48.5 nm are simulated with otherwise identical settings. The outcomes are presented in Fig. 3.4a.

As noted, the strongest pattern is the one with the smallest similar thicknesses signifying the predominant influence of size over the other traits. Among the rest, with a total thickness of 97 nm, the samples with the lower and higher thickness of niobium exhibit the strongest and weakest response, respectively. The curve with the equal average thickness reveals a trend between the upper and lower bound, however, close to the latter. It is inferred that in cases of bilayers with two different crystal structures, one of the constituents has more influence on the overall mechanical properties than the other. Here, the effect of the body-centered cubic niobium with lower activation volumes is more decisive and almost twice as of the face-centered cubic copper on the whole responses either in the reduction or promotion of thicknesses. These effects are better recognized through the equivalent plastic strain defined as

$$E^p_{eq} = \sqrt{\frac{2}{3}(\mathbf{E}^p : \mathbf{E}^p)}\,, \tag{3.5.1}$$

where

$$\mathbf{E}^p = \frac{1}{2}(\mathbf{F}^{pT}\mathbf{F}^p - \mathbf{I})\,, \tag{3.5.2}$$

and plotted in Fig. 3.4b for each case. In the general trends and magnified region, the equivalent strain curves demonstrate the inverse relation with the layer strengths captured in Fig. 3.4a and indicate the largest values for the weakest and smallest ones for the strongest case.

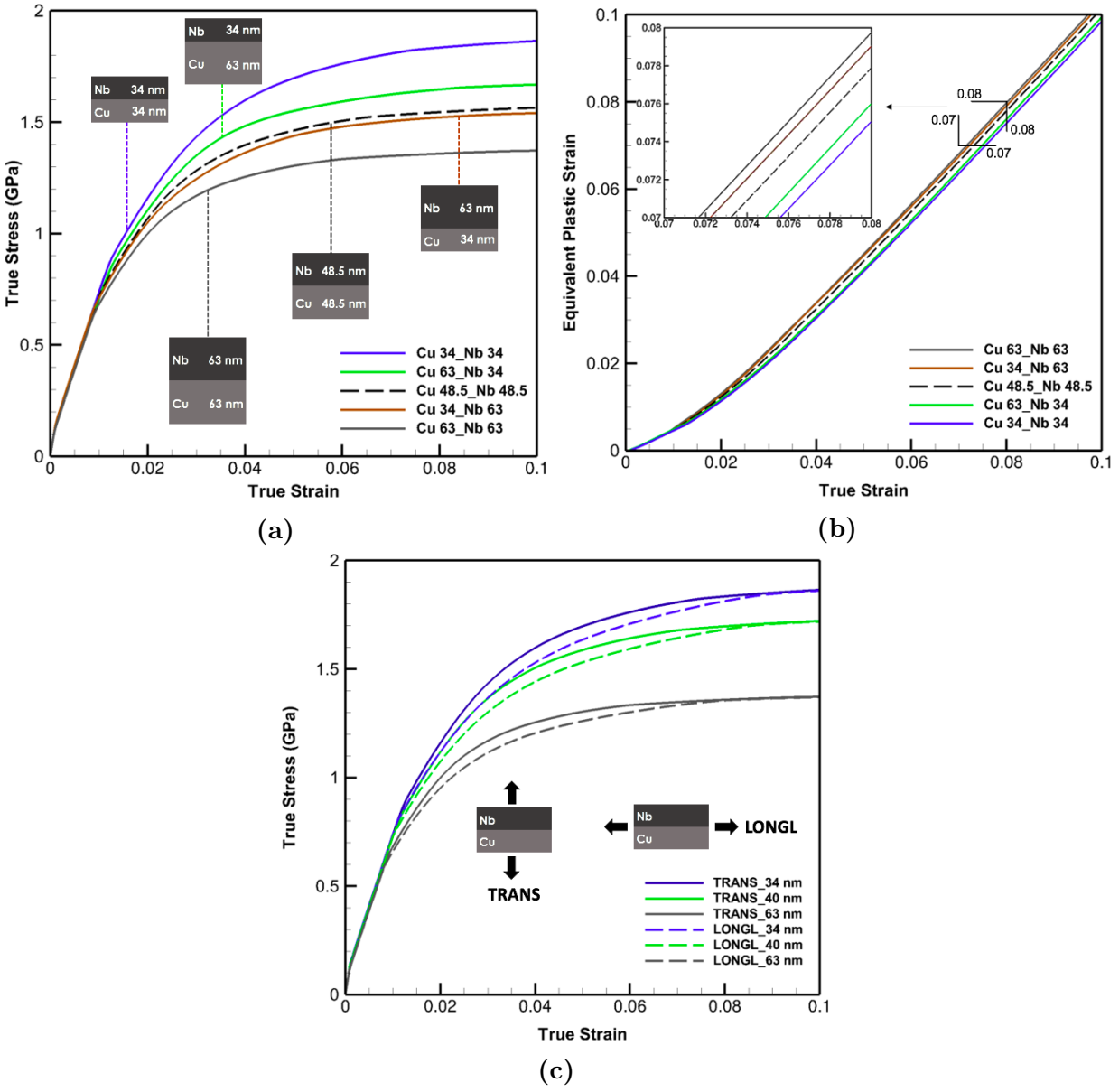

Figure 3.4: (a) True stress-strain curves for 4 thickness combinations of 34 nm and 63 nm as well as 48.5 nm Cu/Nb multi-layers illustrating the effect of layer combinations on the plastic deformation and flow strength. (b) Equivalent plastic strain versus true strain curves for the cases in (a) clarifying the size and layer geometrical order effects. (c) True stress-strain curves of 34 nm, 40 nm, and 63 nm Cu/Nb multi-layers demonstrating the effects of transverse (TRANS) and longitudinal (LONGL) loading directions plotted with solid and dash lines, respectively.

To investigate the load or layer direction effects, the simulations are performed for laminates of 34 nm, 40 nm, and 63 nm under both longitudinal and transverse loading directions, displayed in Fig. 3.4c. Slight differences at the beginning stages of the plasticity are detected increasing with subsidence in layer spacing. However, the identical results in the extended plastic region demonstrate the inconsequential impacts of variations in the loading or layer orientation especially for detecting the flow strength of bilayers.

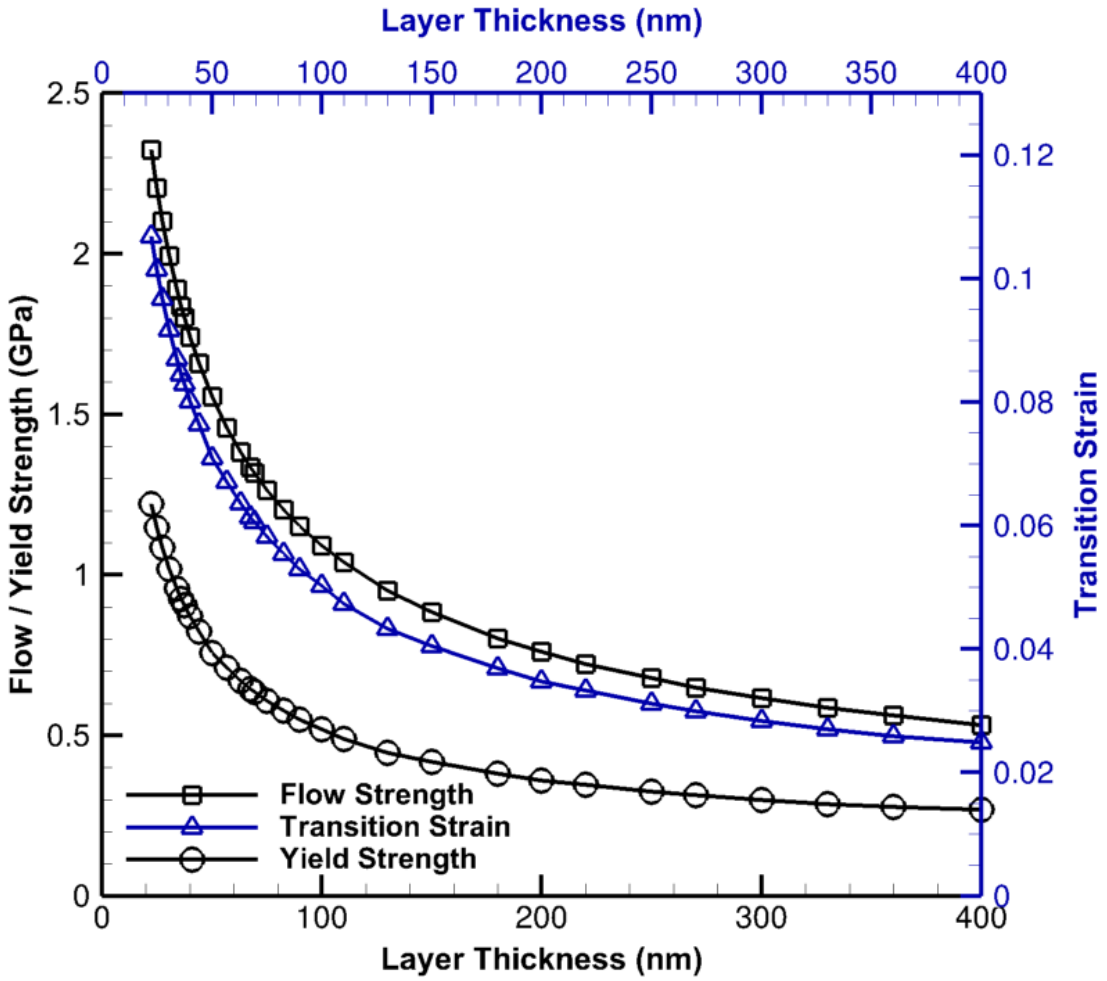

Figure 3.5: The variation of flow and yield strength (left vertical axis) as well as transition strain (right vertical axis), respectively, with respect to layer thickness in the range of 25 nm to 400 nm. The true stress-strain curves in this range is attached to the top right corner to clarify the overall constitutive behavior.

The significance of size effects is delineated in Fig. 3.5 where the flow and yield strength as well as the transition strain in a wide nano-scale interval, 25 nm to 400 nm, are plotted. Considering the

transition strain as the strain sustained from the yield to the onset of flow, a nonlinear descending trend of flow and yield strength is noted as layer spacings decline. The increase in strain transition is primarily due to mechanical thresholds and dislocation structure evolutions aligned with low strain hardening and dynamic annihilation-recovery mechanisms. A small variation in thickness results a dramatic change in the flow and yield strength at the thicknesses of $\lessapprox$100 nm.

This bias has a descending followed by an asymptotic trend whilst the thickness approaches 1 μm. The similar trajectory in transition strain is indicative of an extended prehardening phenomenon pronounced especially at this range that continues to shrink and assume a higher curvature nearing 1 μm.

Considering the demonstrated tends, it is noteworthy to have a comparison between the acquired results from the size-dependent constitutive model and Hall-Petch predictions. Fig. 3.6 illustrates the change of yield strength obtained from the size-dependent constitutive model with respect to $\frac{1}{\sqrt{d}}$, where d is layer thickness. A straight line is plotted near the data points for the trend distinction. As observed, the nonlinear trend of the plotted data displays the inadequacy of the Hall-Petch relation in predicting the yield responses of metallic multi-layers at nano-scale.

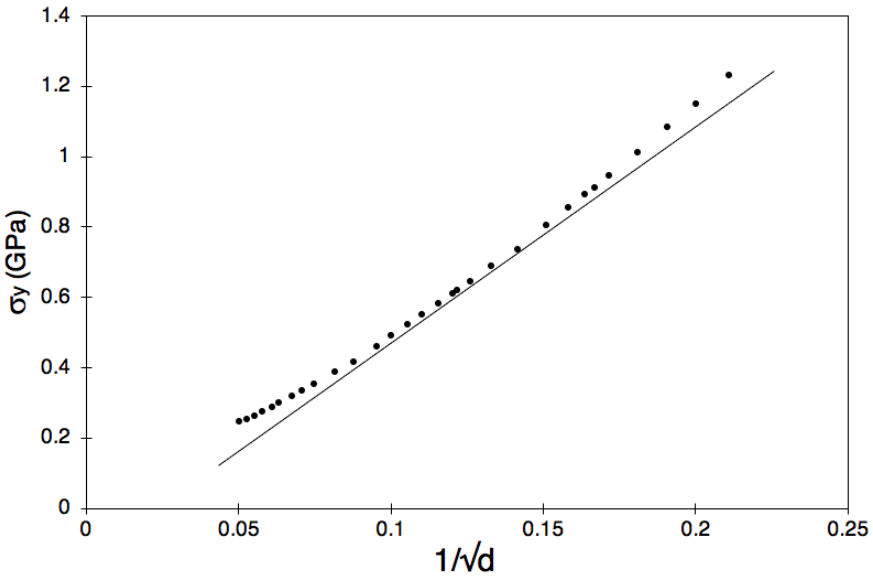

Figure 3.6: The variation of yield strength with respect to $\frac{1}{\sqrt{d}}$, where d is layer thickness, in the range of 25 nm to 400 nm. A straight line is plotted near the points for the trend distinction. Nonlinear trend of the plotted data demonstrate inadequacy of the Hall-Petch relation in predicting the yield responses of metallic multi-layers at nano-scale.

Although the developed models satisfyingly capture metallic nano-layers responses over a broad length scale, the time- and energy-consuming feature of the analysis is a hurdle to be overcome for which the multi-scale concept is sought and implemented as discussed in the next section.

3.6 Statistical Analyses and Homogenized Crystal Plasticity Constitutive Model

The notion of multi-scale modeling has been of constant interest in the realm of computational mechanics and materials. Despite diverse length-scale-dependent methods, hierarchical systems are able to resolve the geometrical and physical details of the underlying mechanisms in lower-scale with higher speed of computation, yet, reasonable precision and simplicity. The reliability extent of acquired responses is evaluated by the adequacy of lower scales assessments, that is, these levels exhibit momentous complementary effects. Classical thermodynamics relations need to be revised for homogenized solids due to the fundamental differences in the degrees of freedom with gases and fluids especially when the goal is eliminating fast atomic degrees of freedom and attaining a homogenization theory. In the case of crystals, elimination is related to the dynamics of crystal defects, particularly dislocations, leading to an additional coarse-graining with the system of governing equations that is no longer Hamiltonian, but dissipative. Unlike ergodic systems characterized by macrovariables and energy parameters, dissipative systems are extremely diverse [72] for which developing frameworks is possible with specific considerations.

Here, the statistical mechanics of the microcanonical ensemble [73] are utilized for the lower scale since the upper scale kinematics are to be characterized considering dissipative transport and nonlinear geometrical models of dislocations [33] along with the independent point-wise temperature. The Clausius-Duhem inequality is incorporated to link the scales through entropy flux where the probability of a phase-space invariant measure with probability density function is assumed plausible.

Dislocation positions are not statistically independent and affect the overall energy of a nanostructure, however, since the precise instantaneous locations associated with the initially considered dislocations can not be identified as deformation evolves, energy is considered as an independent additional characteristic of a dislocation geometrical network [74]. Thereby, the total number of

the dislocations, N_d, and associated energy, E_d, are the independent features of the dislocation network with the priori of equal probability of the ensemble sub-states.

If $\mathbf{x}$ denotes the position of a material point in a system at time t with the continuum mass density, $\rho(\mathbf{x},t)$, divided into N_{ns}, total sub-nano-systems, with identical masses, m_{ns}, and individual volumes, V_{ns}^i, in the total spatial volume, Λ, the system average velocity is defined as

$$\langle \mathbf{v} \rangle = \frac{1}{N_{ns}} \sum_{i=1}^{N_{ns}} \mathbf{v}_{ns}^i \, . \tag{3.6.1}$$

Velocity fluctuation is determined through

$$\tilde{\mathbf{v}}_{ns}^i = \langle \mathbf{v} \rangle - \mathbf{v}_{ns}^i \, , \tag{3.6.2}$$

where $\mathbf{v}_{ns}^i$ is the velocity of each sub-system. The dissipative nature of a system is characterized via the velocity fluctuation of each sub-system, hence, the system disorder manifests itself in the total energy of a system from the lower-scale standpoint as

$$\mathcal{S} = \frac{m_{ns}}{2} \left(\langle \mathbf{v} \rangle \cdot \langle \mathbf{v} \rangle + \sum_{i=1}^{N_{ns}} \tilde{\mathbf{v}}_{ns}^i \cdot \tilde{\mathbf{v}}_{ns}^i \right) + U \Big|_{U_{ns}^i \, ; \, \varepsilon^i} \, , \tag{3.6.3}$$

where U is the total potential energy acquired from the subsystems. The internal energy, U_{ns}^i, is determined over a surrounding volume, V_{ns}^i, such that the deviation at each infinitesimal part of the volume surface, ε^i, depends on the long- and short-range interactions considered among dislocations therein, thus, varies by time evolution, heat flux, and active deformation mechanisms. This relation is associated with the total energy of an ensemble stated by

$$\int_{\Lambda} \rho(\mathbf{x},t) \left(\frac{1}{2} \check{\mathbf{v}} \cdot \check{\mathbf{v}} + \mathfrak{e} \right) dv \, , \tag{3.6.4}$$

with $\check{\mathbf{v}}$ as the velocity and $\mathfrak{e}$ the internal energy density of the system. Consequently, the Helmholtz free energy,

$$\mathscr{H} = U_s \Big|_{U_{ns}^i \, ; \, \varepsilon^i} + \frac{m_{ns}}{2} \sum_{i=1}^{N_{ns}} \tilde{\mathbf{v}}_{ns}^i \cdot \tilde{\mathbf{v}}_{ns}^i = U - T\mathcal{S} \, , \tag{3.6.5}$$

is obtained in which the entropy, $\mathcal{S}$, is associated with the subsystems velocity fluctuations.

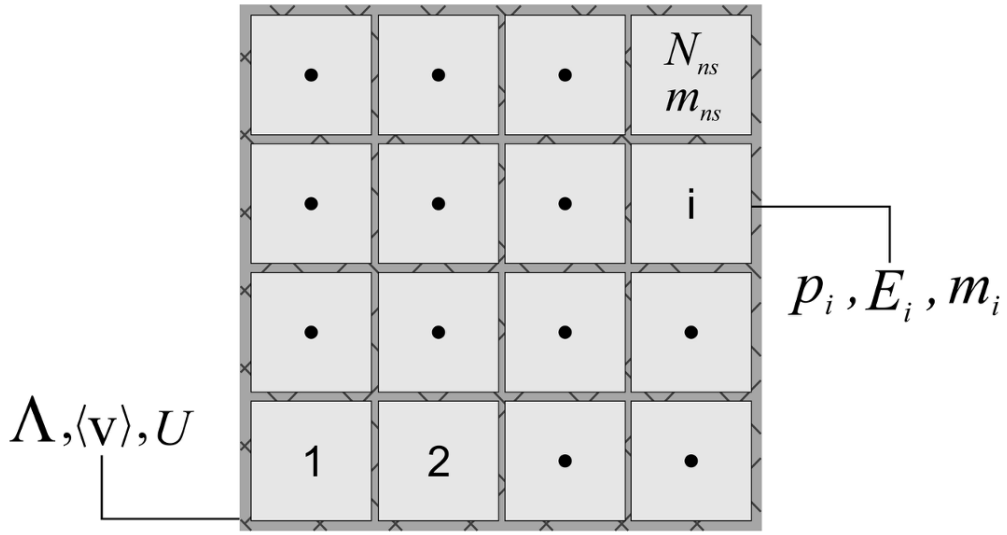

Figure 3.7: Schematic representation of a microcanonical ensemble with equal probability of state, p_i and energy, E_i of each subsystem in the total volume, Λ, with the average velocity of $\langle \mathbf{v} \rangle$ and energy U.

In order to link the lower and upper scale, the statistical Boltzmann entropy principle is utilized as

$$\mathcal{S} = -k_B \sum_i p_i \ln p_i \,, \tag{3.6.6}$$

in which

$$p_i = \frac{\exp(-\frac{E_i}{k_B T})}{\sum_i \exp(-\frac{E_i}{k_B T})} \,, \tag{3.6.7}$$

where p_i is the probability of the ith subsystem with E_i energy as displayed in Fig. 3.7. The hypothesis of an ensemble with a uniform probability distribution in phase-space necessitates the confinement of a subsystem in a particular volume with constant total energy, hence, the system entropy has the format of

$$\mathcal{S} = -k_B \sum_i \frac{\exp(-\frac{E_i}{k_B T})}{\sum_i \exp(-\frac{E_i}{k_B T})} \ln \left(\frac{\exp(-\frac{E_i}{k_B T})}{\sum_i \exp(-\frac{E_i}{k_B T})} \right) \,, \tag{3.6.8}$$

which results in

$$\mathcal{S} = -k_B \sum_i \frac{\exp(-\frac{E_i}{k_B T})}{\sum_i \exp(-\frac{E_i}{k_B T})} \left(-\frac{E_i}{k_B T}\right) + k_B \sum_i \frac{\exp(-\frac{E_i}{k_B T})}{\sum_i \exp(-\frac{E_i}{k_B T})} \ln \sum_i \exp(-\frac{E_i}{k_B T}) \,. \tag{3.6.9}$$

Comparing Eq. 3.6.9 with Eq. 3.6.5 results

$$U = \sum_i E_i \, p_i = \langle E \rangle \,, \tag{3.6.10}$$

where $\langle E \rangle$ corresponds to the average energy of the subsystems. Here, boundary conditions of the homogenized medium presume no relative fluctuations, thus, the extensive variables in the upper scale follow the average principles whose the plausibility is proven.

The homogenized crystal plasticity-based model is founded upon the continuum slip theory of generalized Taylor scale-transition [75, 76]. It contains parameterized representation of the nano-structure features with embedded rate-dependence and latent hardening effects accounting for thermomechanical properties in both elastic and plastic responses. The concept of the representative volume element (RVE) statistically representing the nano-system is incorporated based on retaining the relative dimensions between the homogenized ensemble and nano-structures as well as the underlying deformation mechanisms and dominant features. The hierarchical homogenization analysis follows the Hill-Mandel principle of macro-homogeneity [77, 78] where the volume average of the work increment applied on an RVE is considered equal to the variation of the work on the homogenized system. In the absence of body forces and inertia, the energy consistency is stated in terms of the Eulerian strain rate, $\dot{\mathbf{e}}$, and Cauchy stress with

$$\frac{1}{V_n} \int_\Lambda \boldsymbol{\sigma}_n : \dot{\mathbf{e}}_n \, dV_n = \boldsymbol{\sigma}_H : \dot{\mathbf{e}}_H \,, \tag{3.6.11}$$

where V_n is the volume of the RVE and subscripts n and H correspond to nano and homogenized systems, respectively. Considering the quasi-static applied strain rates, the self-equilibrated spatial stress field is achieved by

$$\nabla \cdot \boldsymbol{\sigma} = 0 \,, \tag{3.6.12}$$

In order to solve the boundary value problem in Eq. 3.6.11 and equilibrium equations, a homogenized crystal plasticity-based constitutive model with the identical nano-scale model backbone, yet, a simplified structure is developed as

$$\dot{\gamma}^{\alpha} = \dot{\gamma}_0^{\alpha} \exp\left[-\frac{Q_{active}}{k_B T}\left(1 - \frac{\tau_{\text{eff}}^{\alpha}}{\tau_{\text{cut}}^{\alpha}}\right)\right] \text{sgn}(\tau^{\alpha}) \,. \tag{3.6.13}$$

Considering previously defined parameters, the CPFE approach is utilized to solve the equilibrium equation as described in appendices A and B. The constitutive parameters are formulated in terms of structural variables and calibrated through the computational homogenization of the lower scale model and the RVE that consists of layer thicknesses of stacked nano-layers.

Prior to plasticity, the elastic responses of a homogenized system must be realized, thus, the equivalent elastic constants, $\check{C}_{ij}$, are attained as a combination of the constituents elastic constants, C_{ij}, with respect to their thicknesses, d_k, in a multi-nano-layer as

$$\check{C}_{ij} = \sum_{k=0}^{N_{mat}} C_{ij} \frac{d_k}{d} \,, \tag{3.6.14}$$

where d is the total thickness of the specimen and N_{mat} the number of constituents. The rate dependence feature is modified for the homogenized ensemble with the total N_l layers by

$$\mathbf{l}^p = \sum_{i=1}^{N_l} \lambda^i \, \dot{\gamma}^i \, (m_0^i \otimes n_0^i) \,, \tag{3.6.15}$$

in which $\lambda^i = \frac{V_i}{V_{total}}$ signifies the layer volume fraction.

3.6.1 Parameters in The Homogenized Constitutive Model

Sensitivity analyses detect two influential constitutive functionals to be calibrated from the lower scale; saturation shear stress, τ_{sat}, and initial hardening, h_0. These are functions of each constituent layer thickness, e.g., $\tau_{sat}(d_{Cu}, d_{Nb})$ and $h_0(d_{Cu}, d_{Nb})$ for Cu/Nb nano-layers. In order to obtain the relations of the effective functionals in terms of each material, several cases with different layer thicknesses of Cu and Nb are made. Two sets of nano-layers are considered in which the thickness of one material is fixed at 34 nm, 63 nm, and 100 nm while the other one varied

from 25 nm to 400 nm and vice versa. Then, the simulations are performed based on the size-dependent constitutive model at nano-scale regime, Eq. 3.3.23. The τ_{sat} and h_0 calibration plots are demonstrated in Fig. 3.8. The variation of τ_{sat} with constant d_{Cu} and varying d_{Nb} is plotted in Fig. 3.8a where the best fitted function for simulated data has the form of

$$\alpha_1 + \frac{\alpha_2}{\sqrt{d_{Nb}}} \,. \tag{3.6.16}$$

The same process for Nb yields the similar functional structure with

$$\alpha_3 + \frac{\alpha_4}{\sqrt{d_{Cu}}} \,, \tag{3.6.17}$$

plotted in Fig. 3.8b. However, the best fitted functions for h_0 is different and has the format of

$$\beta_1 + \frac{\beta_2}{\sqrt[3]{d_{Cu}}} \,, \tag{3.6.18}$$

when d_{Nb} is fixed and

$$\beta_3 + \frac{\beta_4}{\sqrt[3]{d_{Nb}}} \,, \tag{3.6.19}$$

while d_{Cu} is constant as illustrated in Figs. 3.8c, 3.8d, respectively. Consequently, the final formulations of the effective functionals are derived as

$$\tau_{sat} = \left(\alpha_1 + \frac{\alpha_2}{\sqrt{d_{Cu}}}\right)\left(\alpha_3 + \frac{\alpha_4}{\sqrt{d_{Nb}}}\right), \tag{3.6.20}$$

and

$$h_0 = \left(\beta_1 + \frac{\beta_2}{\sqrt[3]{d_{Cu}}}\right)\left(\beta_3 + \frac{\beta_4}{\sqrt[3]{d_{Nb}}}\right) \,, \tag{3.6.21}$$

for generalized circumstances when both d_{Cu} and d_{Nb} are changing. These equations have four unknowns to be calibrated. Due to the high nonlinearity of the acquired equations, determining α_i , β_i necessitates a thorough, compatible optimization scheme. Thus, a metaheuristic genetic

algorithm approach is utilized to attain the parameters which results in the following equations as

$$\tau_{sat} = \left(12.6169 + \frac{0.0028}{d_{Cu}}\right)\left(9.0473 + \frac{0.0032}{d_{Nb}}\right) \tag{3.6.22}$$

$$h_0 = \left(48.3222 + \frac{0.4358}{\sqrt[3]{d_{Cu}}}\right)\left(23.4275 + \frac{0.7791}{\sqrt[3]{d_{Nb}}}\right) \tag{3.6.23}$$

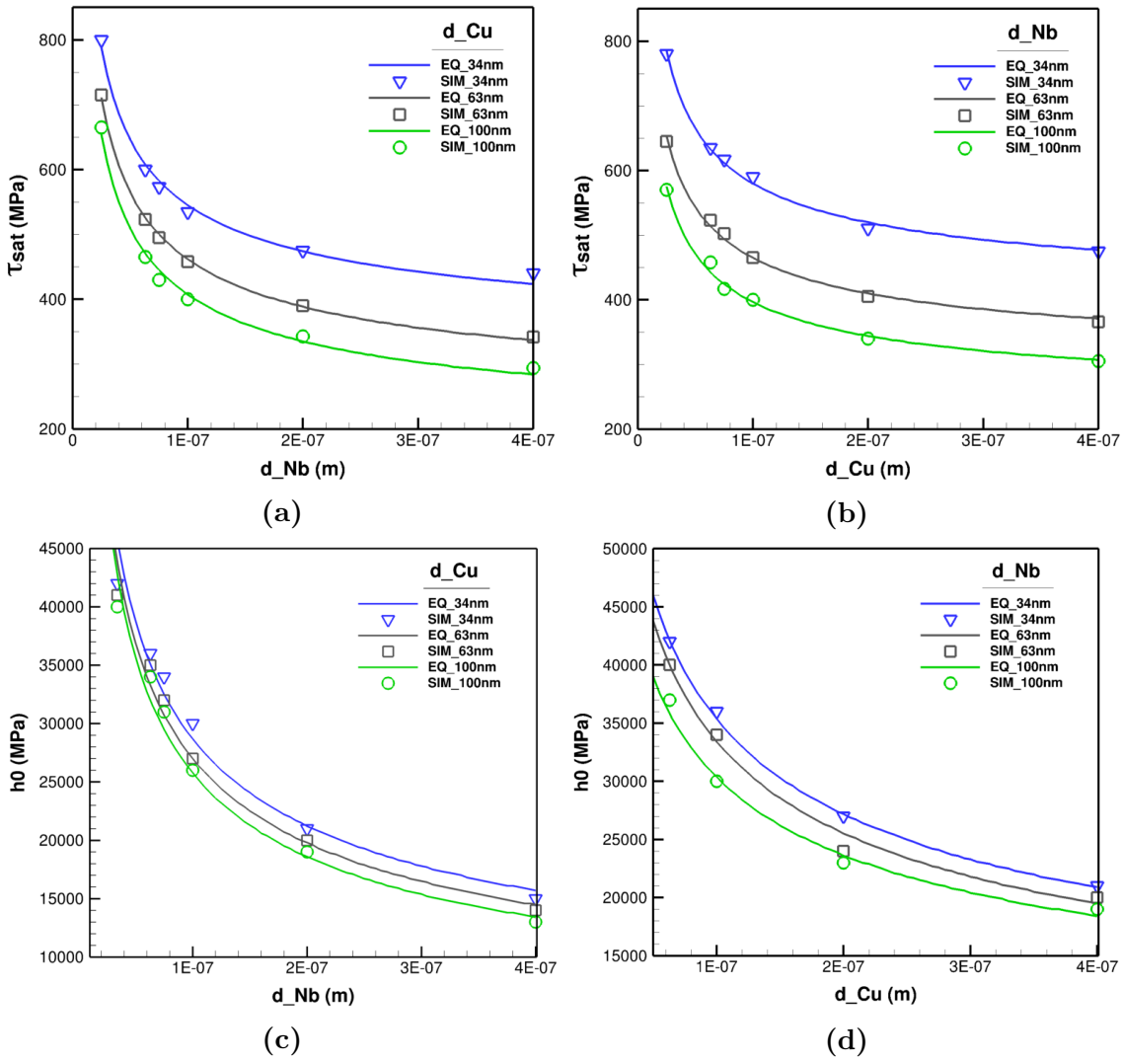

Figure 3.8: Variations of effective parameters in homogenized constitutive model with layer thicknesses where one layer thickness is fixed while the other one changes. Symbolic points signify simulation (SIM) results and solid lines the best fitted equivalent curves (EQ). Variations of τ_{sat}, for (a) fixed Cu layer spacing, d_Cu, and (b) fixed Nb layer spacing, d_Nb. Variations of h_0, for (c) fixed Cu layer spacing, d_Cu, and (d) fixed Nb layer spacing, d_Nb.

The homogenized constitutive model enhances the efficacy of computational processes in diverse aspects. Hereby, five random microstructures with different layer thicknesses are simulated; first, with the size-dependent constitutive model at nano-scale develped in Eq. 3.3.23, and second, through the homogenized constitutive model established in Eq. 3.6.13.

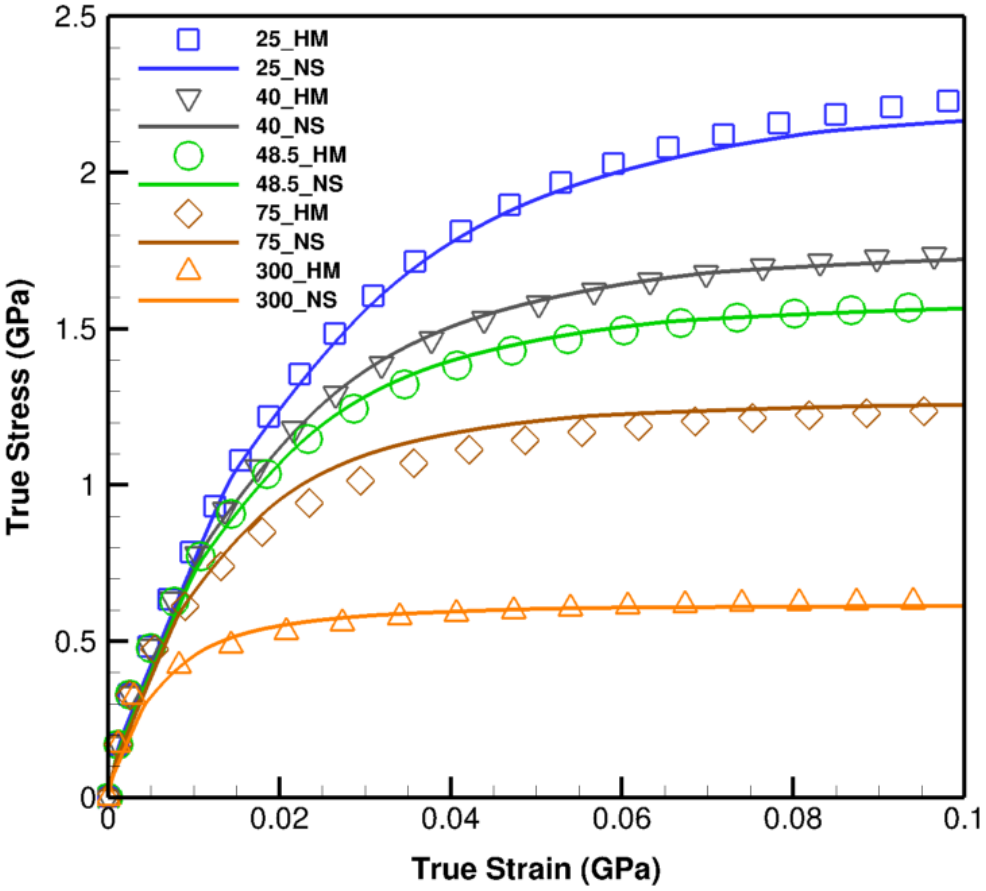

Figure 3.9: Verifications of the homogenized with nano-scale constitutive models through 25 nm, 40 nm, 48.5 nm, 75 nm, and 300 nm Cu/Nb laminates. Symbolic points denote homogenized (HM) and solid lines the nano-scale (NS) model results.

The lower scale simulations proceed through the model with the explicit representation of layer thickness while the homogenized model is executed by the implicit impact of size given in Eqs. 3.6.22 and 3.6.23. The results and comparisons shown in Fig. 3.10 exhibit cogent agreements between two models, albeit, the homogenized constitutive model significantly reduces the computational time and cost by several (> 4) orders of magnitude.

3.7 Temperature-Dependent Homogenized Constitutive Model

In general, the elevated temperature induces relative diffusive mass flux due to energy gradients. Diffusional creep is considered the main deformation mechanism at the vicinity of the melting point, T_m, in metallic nano-layers [79] where the stress-driven diffusion of vacancies along grain boundaries compels atomic diffusion of the grain interiors in the opposite direction. This effect is alleviated by atomic diffusion along grain boundaries at lower temperature [80] while the dislocation glide along grain boundaries becomes the dominant mechanism at intermediate and low homologous temperatures. Cu/Nb cases, at temperatures up to 800°C, exhibit dislocation-based plastic deformation where diffusion creep can be ignored due to generated thermally stable structures [9]. Being cognizant of the experimental difficulties mentioned in Sec. 3.1 for obtaining mechanical responses of metallic nano-layers at elevated temperatures, a temperature-dependent homogenized model is developed with the advantages of acquiring responses through fast and cost-effective performances. Behaviors of metallic nano-layers at elevated temperatures are experimentally observed in multiple fields such as radiation tolerance [52], morphology evolution, and high thermal stability up to 700°C and 800°C [81, 82], respectively, in sputtered and ARB Cu/Nb nano-layers in which morphological deformations are observed identical at room temperature and about 400°C.

Table 3.3: Elastic parameters of copper and niobium acquired from the calibration process.

Cu				Nb			
χ_{11}(GPa)	184.13	ω_{11}(GPa/K)	-0.05	χ_{11}(GPa)	262.70	ω_{11}(GPa/K)	-0.06
χ_{12}(GPa)	133.32	ω_{12}(GPa/K)	-0.04	χ_{12}(GPa)	143.33	ω_{12}(GPa/K)	-0.03
χ_{44}(GPa)	88.15	ω_{44}(GPa/K)	-0.04	χ_{44}(GPa)	40.18	ω_{44}(GPa/K)	-0.01
m_1(GPa)	52.95	m_2(GPa/K)	-0.02	m_1(GPa)	30.88	m_2(GPa/K)	-0.01

The homogenized constitutive model in Eq. 3.6.13 works with a mild variation of ambient temperature; however, generic temperature variations require additional changes in some of the material constants and constitutive parameters. The elastic constants can be written as a function of absolute temperature [83] by

$$C_{ij} = \chi_{ij} + \omega_{ij} T \,, \tag{3.7.1}$$

and shear modulus with

$$\mu = m_1 + m_2 T \,, \tag{3.7.2}$$

where the constants, χ_{ij} , ω_{ij} , m_1 , m_2 are designated in Table 3.3 for Cu/Nb nano-layers.

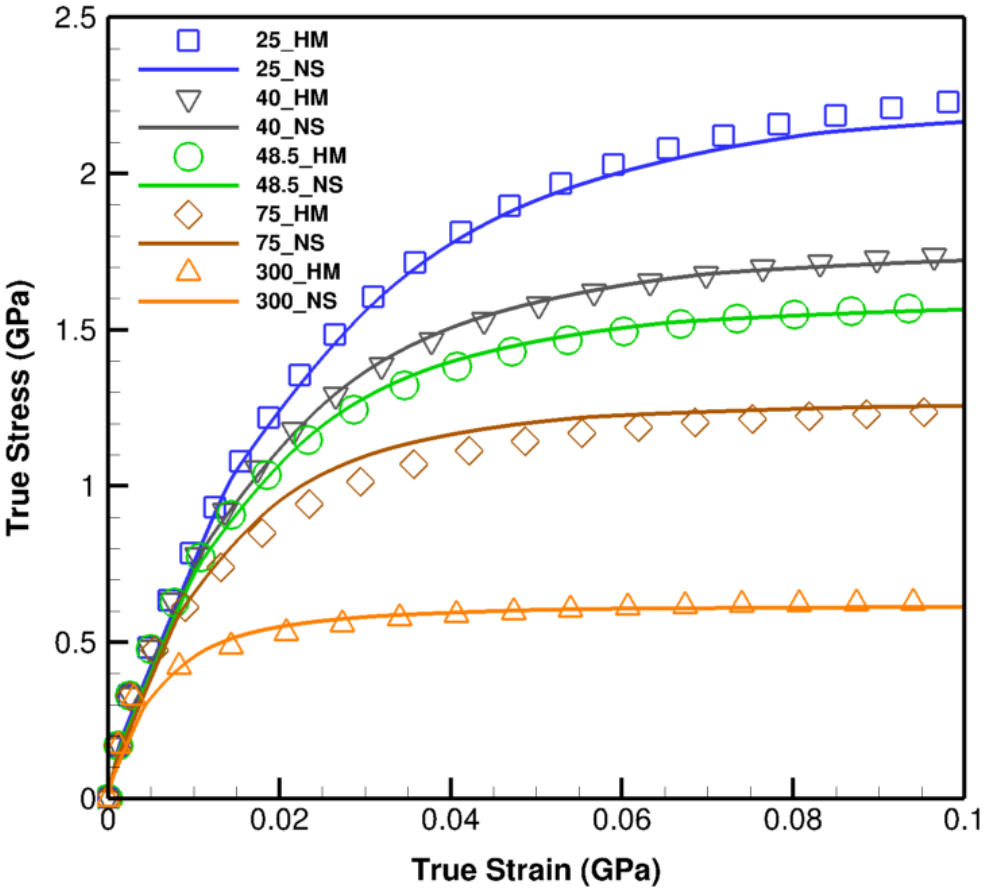

Figure 3.10: Verifications of the homogenized with nano-scale constitutive models through 25 nm, 40 nm, 48.5 nm, 75 nm, and 300 nm Cu/Nb laminates. Symbolic points denote homogenized (HM) and solid lines the nano-scale (NS) model results.

The effective parameters, saturation shear resistance and initial hardening, also change in terms of temperature. To achieve the general format of these functionals and obtain the associated parameters, experimental data in [8, 9] are incorporated through the deep-learning SLC and metaheuristic

genetic algorithms. Thus, effective temperature-dependent functionals are obtained as

$$\tau_{sat} = \left[\psi_0 \exp\left(\frac{\zeta}{T - T_c}\right) + \psi_1\right] \left(12.6169 + \frac{0.0028}{d_{Cu}}\right) \left(9.0473 + \frac{0.0032}{d_{Nb}}\right) , \tag{3.7.3}$$

along with

$$h_0 = (\eta_0 + \eta_1 T) \left(48.3222 + \frac{0.4358}{\sqrt[3]{d_{Cu}}}\right) \left(23.4275 + \frac{0.7791}{\sqrt[3]{d_{Nb}}}\right) , \tag{3.7.4}$$

and the associated parameters of ψ_0 , ψ_1 , ζ , T_c , η_0 , η_1 are calibrated as shown in Table 3.4.

Table 3.4: Saturation shear resistance and initial hardening parameters.

ψ_0	ψ_1	ζ	T_c	η_0	η_1
7.31	-5.72	100.00	1450.00	1.42	-0.0014

For verification, simulations are performed for Cu/Nb multi-layers with thicknesses of 34 nm, 60 nm, and 63 nm at $25°C$, $400°C$, and $500°C$ as demonstrated in Fig. 3.11a. As observed, the simulations and experimental results exhibit solid agreements in which dramatic decline in flow stresses by increasing temperature is plainly detected.

Further illuminating this phenomenon, Cu/Nb multi-layers with 25 nm, 50 nm, 75 nm, and 100 nm thicknesses are modeled from room temperature up to $700°C$ where the variation of flow strengths in terms of temperature is displayed in Fig. 3.11b. Each curve is indicative of slight variation in flow stress at initial stages while revealing an appreciable drop as temperature grows. For instance, in 25 nm specimen, the flow stress notably, about 80%, drops from room temperature to $700°C$. From another angle, the increase of temperature degrades the mechanical responses of a thin metallic nano-layer to a thicker one at room temperature; this can be clearly perceived in Fig. 3.11a where a 34 nm Cu/Nb at $400°C$ exhibits the strength of a 63 nm Cu/Nb at $25°C$.

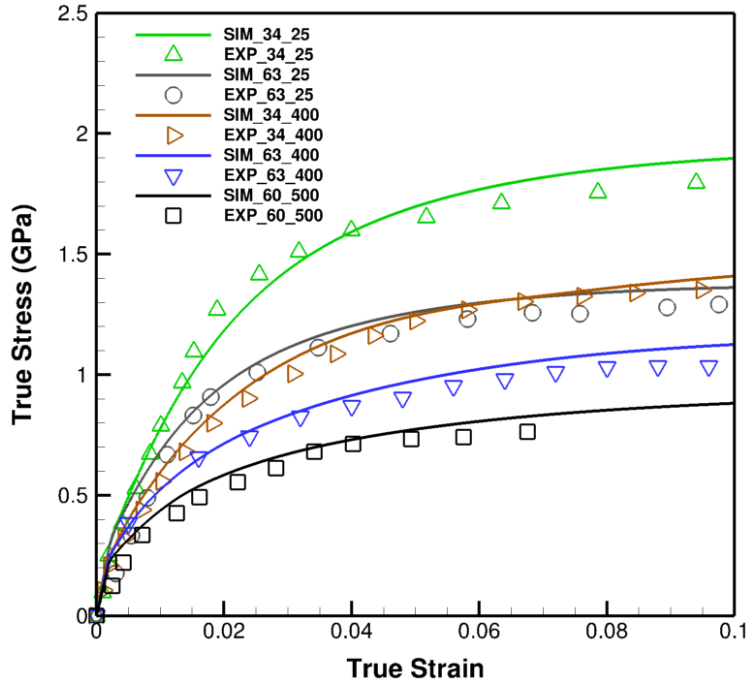

(a)

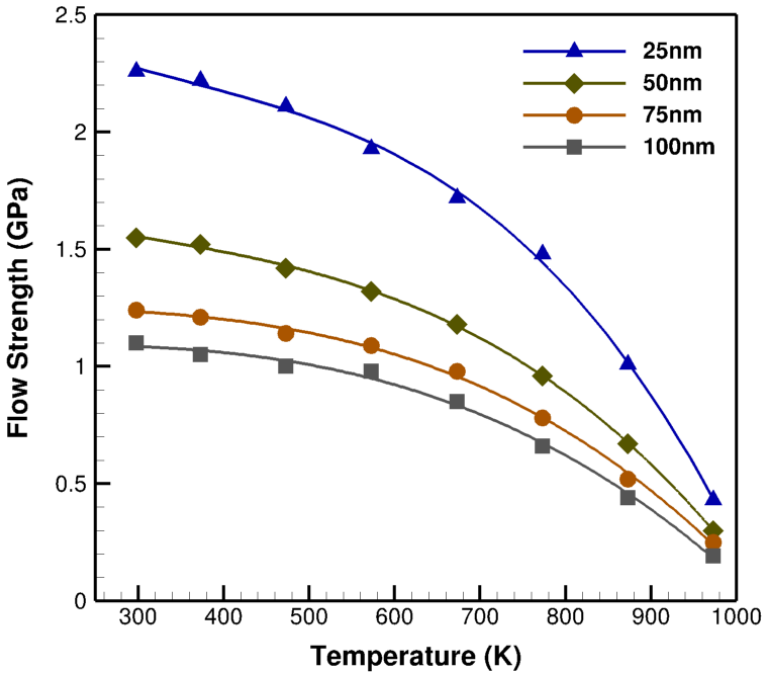

(b)

Figure 3.11: (a) The validation of the temperature-dependent homogenized constitutive model with 34 nm 60 nm, and 63 nm Cu/Nb laminates at $25°C$, $400°C$, and $500°C$. Symbolic points are the experimental (EXP) [8, 9] and solid lines the simulation (SIM) data. (b) Flow strength versus temperature curves of 25 nm, 50 nm, 75 nm, and 100 nm Cu/Nb laminates at $25°C$ up to $700°C$ demonstrating the nonlinear effects of temperature growth on flow strength.

4. SENSITIVITY ANALYSIS

4.1 Background

Sensitivity analysis (SA) determines the uncertainty levels in the outputs of a model in relation to the variation of the model inputs [84]. It is utilized to recognize the input variables that contribute the most to an output behavior, the non-influential ones, and to learn interaction effects among them. A related practice is uncertainty analysis (UA), which focuses rather on quantifying uncertainty in model output and commonly incorporated along SA to acquire sufficient information about the effects of inputs on the model properties. The main difference between uncertainty and sensitivity analysis is that the former focuses on just quantifying the uncertainty in a model output while the latter is the study of the relative importance of different input factors on the model output.

The SA process involves the analysis of the sensitivity or importance indices of the input variables with respect to a given quantity of interest in the model results. Importance measures of each uncertain input variable on the response variability provide a deeper understanding of the modeling in order to reduce the response uncertainties in the most effective way [85]. For instance, putting more effort into the knowledge of influential inputs, parameters whose specific value can significantly influence the behavior mode of the system such as exponential growth, asymptotic growth, S-shaped growth, oscillation, etc., will reduce their uncertainties. The underlying goals for SA are model calibration, validation, and assisting with the decision-making process.

SA processes involve the main concepts of model, input, and output which need to be well understood. Fig. 4.1 demonstrates the role of SA in a scientific procedure. The area on the left display a problem field that exists with assumingly governing equations and rules which if harvested the left region is constructed as a model with the acquired rules and hypothesis. The model, now, accepts some data to show how it can yield results identical to the real problem as input and output, respectively.

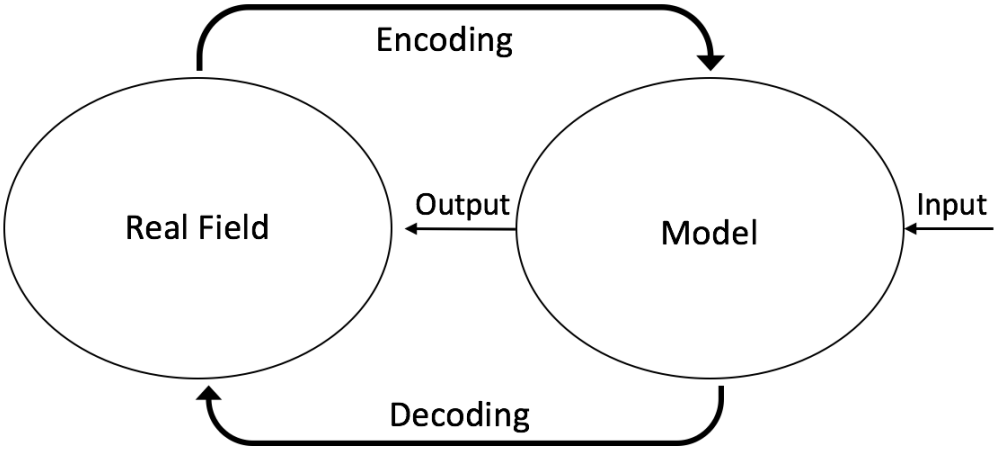

Figure 4.1: The visualization of real field, model, input, and output concepts.

Thereby, as long as any model outputs are compatible with the real field observation provided their governing equations are physics and/or phenomenological based, those can be considered as the models representing a mathematical interpretation of the real problem. In fact, the idea of the world into models is conditionally a true statement, however, the most applicable models are the ones with the least possible complexities and intractabilities.

Another concept to deal with is uncertainty, an obstacle to creating a proper model [86]. Philosophically speaking, models are not to be validated but proved through numerous tests to be defensible and corroborated, that is, the models can explain and predict the real problem behavior consistent with the observed properties, albeit up to the capacities of the models. Since models are part of a scientific interpretation of real phenomena, thus, subjected to epistemological debate with post-normal science (PNS) as demonstrated in Fig. 4.2.

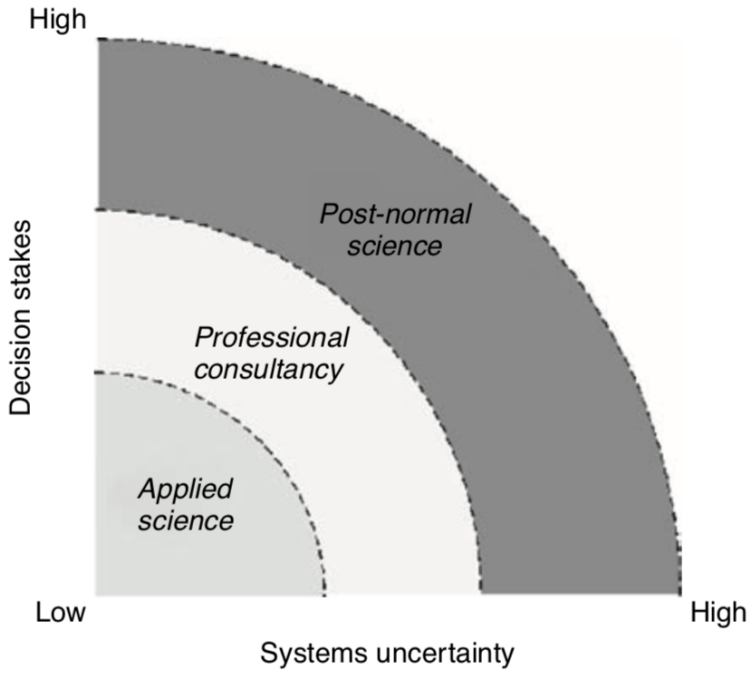

Figure 4.2: The uncertainty-stakes diagram for categorizing scientific models [10].

Based on the system's uncertainties and the stakes involved, three types of modeling are realized.

- Applied science, when a model is created and used by scientists as the sole users of the model;
- Professional consultancy, when the model is utilized for scientific and industrial projects;
- PNS, when the model is incorporated to provide evidence under circumstances of conflicting stakes and beliefs.

The nature of models is also another factor in classifying them. Models can be diagnostic and/or prognostic, that is, understands and/or predicts a real field behavior, respectively. Also, models can be data-driven and/or law-driven, meaning, functions based on statistical observed data and/or combines the applicable rules on the modeled system, respectively. Each of said models has its benefits and disadvantages which, commonly, optimized in terms of the system delicacy to be simulated.

4.2 Theory and Application of Sensitivity Analysis

In order to describe the practical usage of these assessments, the method itself needs to be divided into specific classes in terms of the sensitivity and volatility of data and the employed approach to deal with them.

4.2.1 Local and Global Sensitivity Analysis

In terms of output variations, SA can be categorized into two major groups, namely, local and global.

1. Local SA investigates small input perturbations that occur around nominal values, the mean of a random variable, for instance, on the model output [11]. This method assesses the partial derivatives of the model at a specific point of the input variable space in a deterministic way, that is, there are linearity and normality assumptions along with using local variations. These defaults, however, are limitations of these types of methods.

2. Global SA overcomes the limitations of local SA for studying the effects of small variations in inputs around a given value on the outputs. It does not distinguish any initial set of model input values but considers the numerical model in the entire domain of possible input parameter variations [87]. Thus, the global SA is utilized to study a mathematical model as a whole rather than one of its solution around parameters specific values [88].

4.2.2 Sensitivity Analysis Objective

The main step at the beginning is clearly specifying the objectives before performing an SA [89] including:

1. Preliminary assessments of variables and outputs, such as real output observations, constraints, etc.

2. The factor prioritization setting to identify the significant factors. The ones, if subjected to slight perturbations, instigate the utmost uncertainty of outputs.

3. The factor fixing setting to reduce the number of uncertain inputs by fixing unimportant factors. The ones, if subjected to slight or medium perturbations, do not initiate the significant uncertainty of outputs.

4. The variance cutting setting as a part of a risk assessment study to reduce the output uncertainty from its initial value to a lower pre-established threshold value.

5. The factor mapping setting, to identify the main inputs in a specific domain of the outputs specifying the combination of factors that generate output values above or below a given threshold.

4.3 Sensitivity Analysis in Practice

Two frameworks are utilized when analyzing a model, deterministic and probabilistic. In a deterministic framework, specific inputs are considered to analyze the model where statistical approaches are utilized in order to ascertain the uncertain inputs. In a probabilistic framework, the inputs are considered as random variables $\mathbf{x} = x_i\,; i = 1, 2, ..., n$ for which the model, $G(x_i)$, outputs are assessed. If a scalar value, y, is appointed to each variable vector $\mathbf{x}$, it is assumed random as well, however, with unknown distribution. SA statistical methods involve designing inputs and outputs through approaches such as the Monte Carlo techniques and modern statistical learning methods.

As an example, a local SA is utilized through a graphical tool that can be applied on an initial sample with three inputs and one output, $(x_1, y), (x_2, y), (x_3, y)$. Simple scatterplots lead to the initial assessments between input/output variables as illustrated in Fig. 4.3.

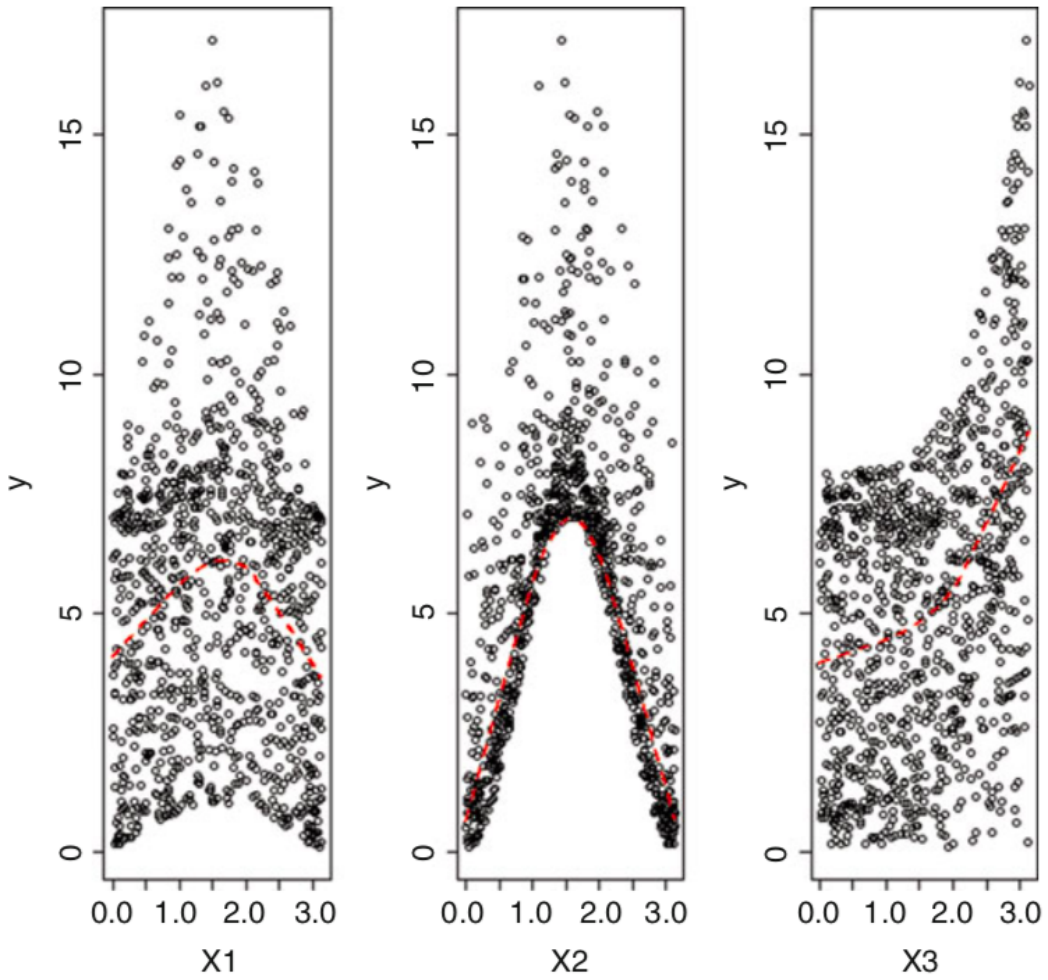

Figure 4.3: Scatterplots of 200 simulations on a numerical model with three inputs in horizontal axes and one output in the vertical axes. Dotted curves are local-polynomial-based smoothers [11].

As it is noted, the interactions between inputs cannot be inferred from these plots, thus, the cobweb or parallel coordinate plots [90] can be used. These plots, as shown in Fig. 4.4, link the variable and associated outcome common among the inputs together. As observed, the smallest values of the model output are highlighted in red corresponding to the combinations of small and large values of the inputs.

A global SA can also be incorporated for these types of problems via sampling-based sensitivity analysis methods; however, the number of sample sizes must be adequately large, greater than the input variables.

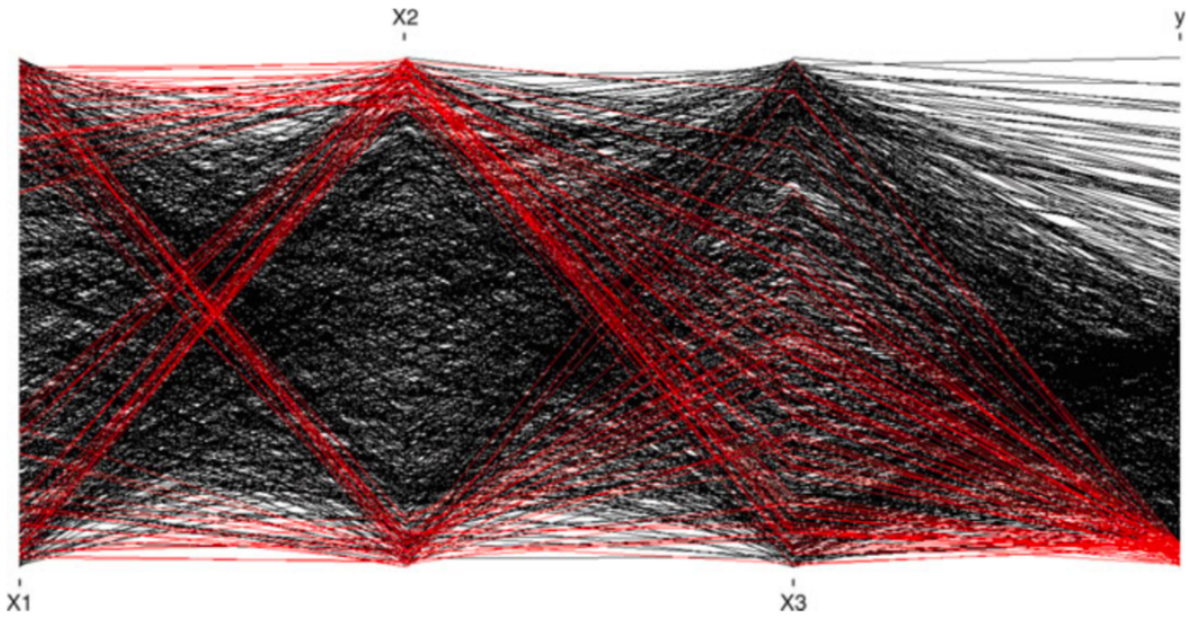

Figure 4.4: Cobweb plot of 200 simulations of a numerical model with three inputs, first three columns, and one output, last column [11].

In these approaches, a linear model explaining the behavior of output is obtained and the standard regression coefficients are defined as

$$SRC_j = \beta_j \sqrt{\frac{\text{var}(x_j)}{\text{var}(y)}}\,, \tag{4.3.1}$$

where β_j is the linear regression coefficient of x_j.

Most SA methods introduce a trade-off between the number of computational sensitivity analysis and the model complexity, that is, selecting an SA method and the number of computations is contingent on the complexity of the target model and the number of inputs, albeit, the computational costs, most of the time, are controlling factors in this matter. In summary, the selection of an SA approach follows the subsequent trajectory:

- General assessments related to the model complexity and regularity;
- Distinguishing the type of information provided by each SA method, global, local, and their derivatives;
- Identifying SA methods through prior knowledge about the model behavior.

The most adaptable SA method chosen accordingly is the most practical one, which means for a costly computational approach a complicated detailed based SA technique is not necessarily a proper choice.

4.4 Sensitivity Analysis in Size-Dependent Constitutive Model

The crystal plasticity size-dependent constitutive model has as many as ten parameters to be calibrated and validated based on the experimental data. The model is considered as diagnostic-prognostic since it has the ability to signify the underlying mechanisms in deformation processes and predict the associated behavior.

The model exhibits several nonlinear convoluted equations in each time step requiring hundreds of iteration for each one to be solved, thereby, due to the complexity of the model and the computational workload, local sensitivity analysis is performed on the model where for each calibrated parameter slight tolerances of ±10& are considered and accordingly the model responses are captured. Subsequently, factor prioritization setting is performed in order to identify the significant parameters which can create a clear insight of the extent of sensitivity to the arranged parameters as well.

The chart in Fig. 4.5 demonstrates the effects of the variation of all parameters on the overall behavior of the model due to the said tolerances averaged over the main features including yield and flow strength, transition strain, and hardening. Each deviation percentage specifies the share of each parameter in the total deviation from the exact response of the model.

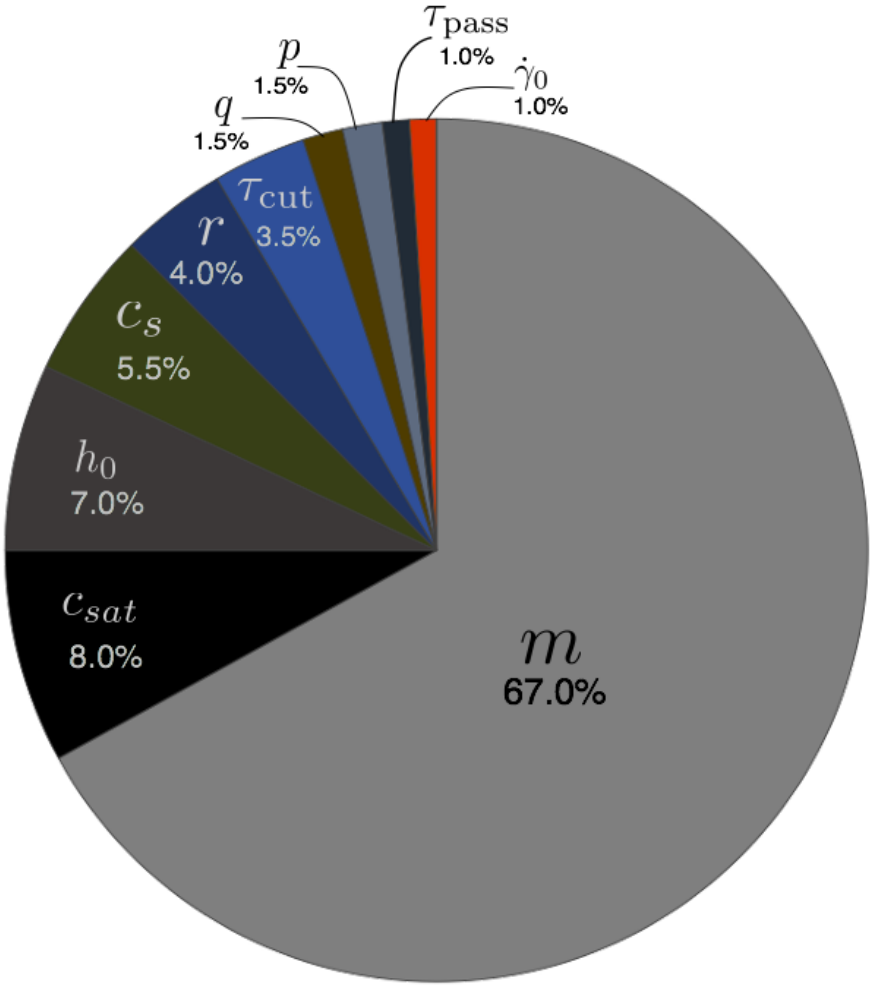

Figure 4.5: Sensitivity analysis of the crystal plasticity size-dependent constitutive model for ten parameters. Each deviation percentage specifies the share of each parameter in the total deviation from the exact response of the model.

As it is observed, not all parameters are identically influential. In order to optimize the number of inputs for further computational processes, the factor prioritization setting is executed where six parameters are recognized as prominent factors for additional analysis. To categorize the parameters in more detail, the model response is divided into four main sections, namely, yield, transition, hardening, and flow with the same concepts discussed in previous chapters. With this arrangement, the effect of individual parameter indicated as the deviation percentage, d %, from the precise response of that section on each part, is assessed in the three-dimensional plot, Fig. 4.6, for comparison purposes.

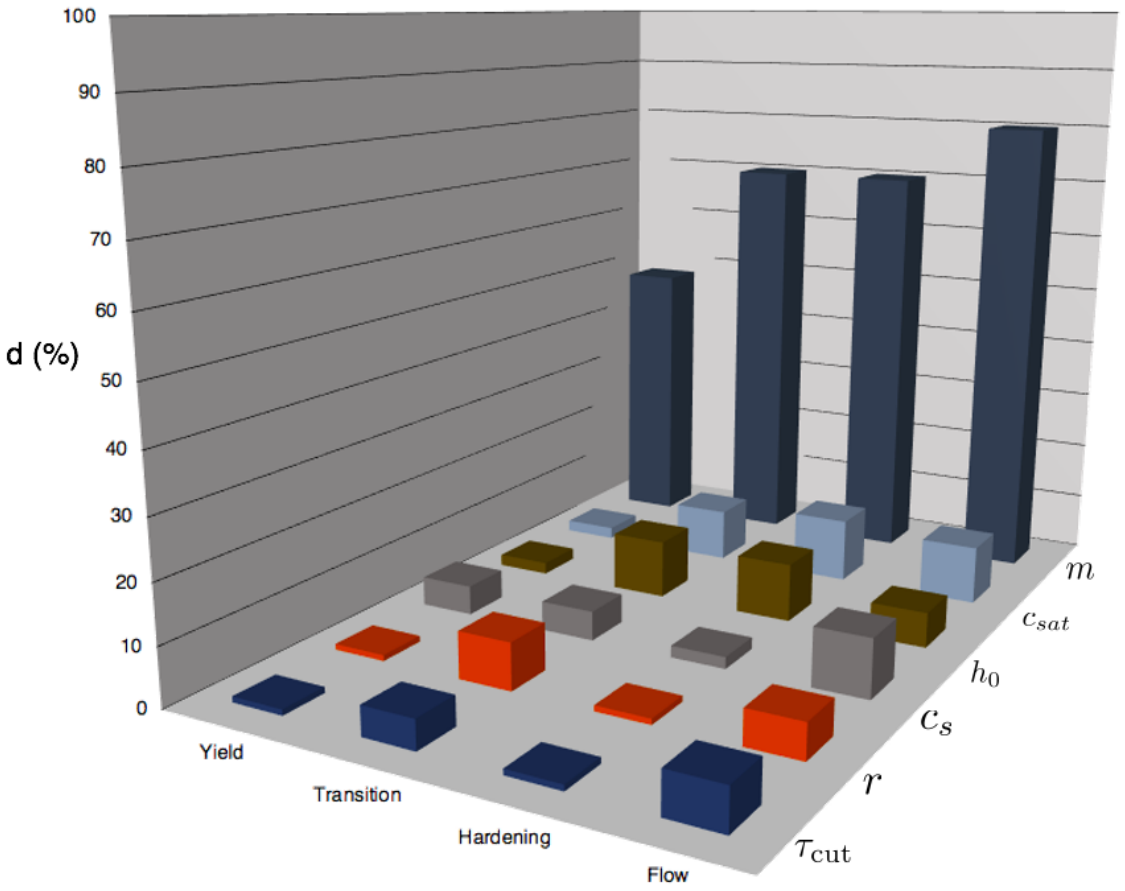

Figure 4.6: Sensitivity analysis performed on the prioritized parameters, indicated as the deviation percentage, d %, from the precise response of yield, transition, hardening, and flow sections.

The plot displays that even among the prioritized parameters some of those are more influential on a specific repose section than the others which serves the purpose of reducing the analysis inputs, albeit for a particular output section. In order to clarify this trend, the deviation percentage for each response section is separated in terms of the arranged parameters.

As noted in Fig. 4.7, for the yield section, parameters m and c_s, in Fig. 4.8, for the transition section, parameters m, c_{sat}, h_0, and r, in Fig. 4.9, for the hardening section, parameters m, c_{sat}, and in Fig. 4.10, for the flow section, m, c_{sat}, and c_s are the dominant factors.

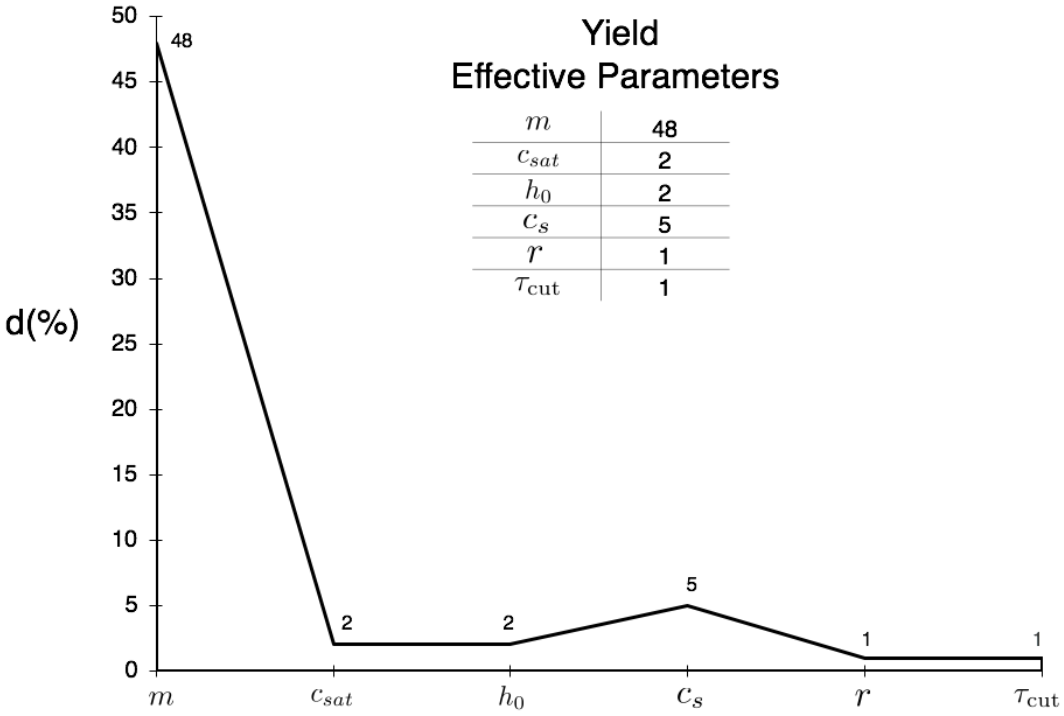

Figure 4.7: The deviation percentage of the prioritized parameters on the yield strength.

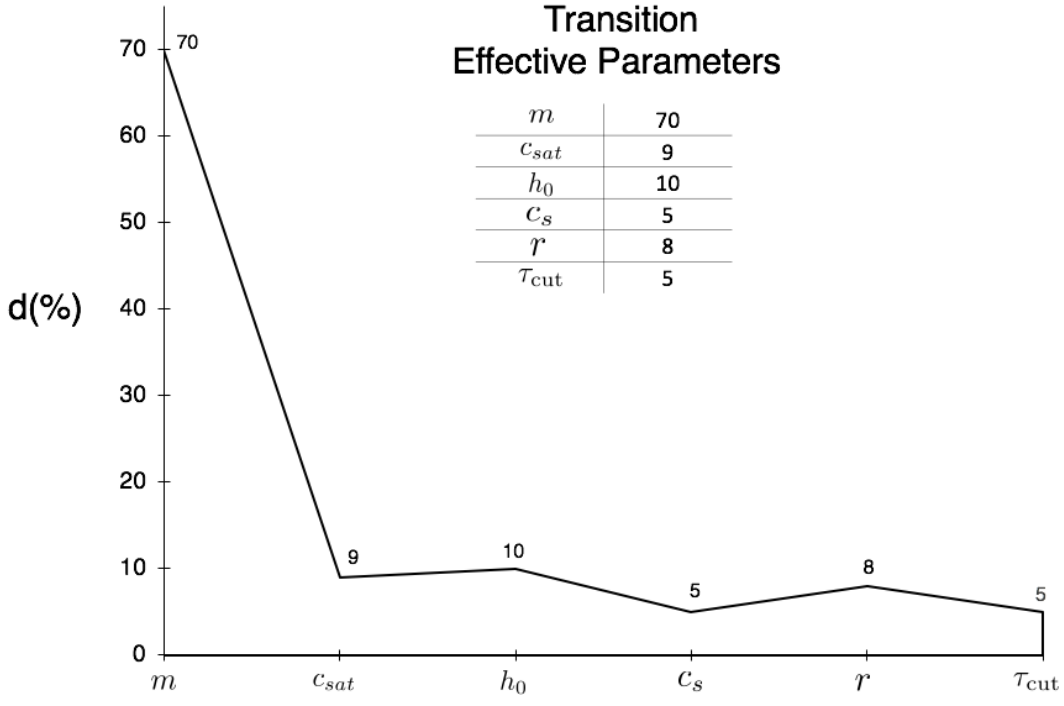

Figure 4.8: The deviation percentage of the prioritized parameters on the transition strain.

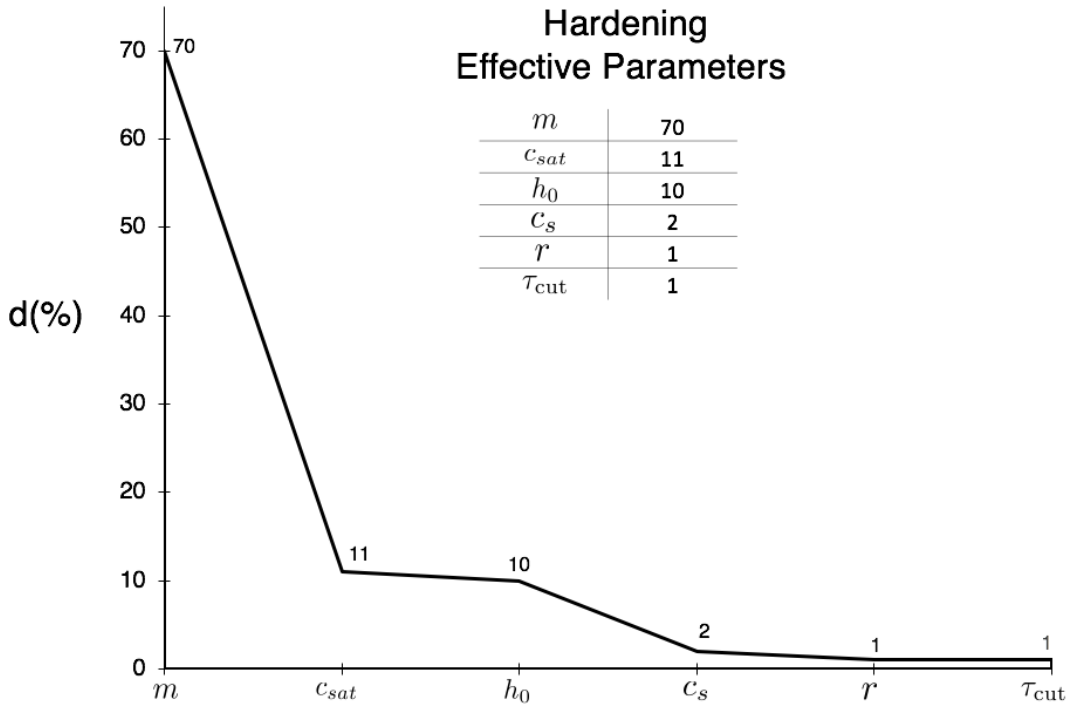

Figure 4.9: The deviation percentage of the prioritized parameters on the hardening.

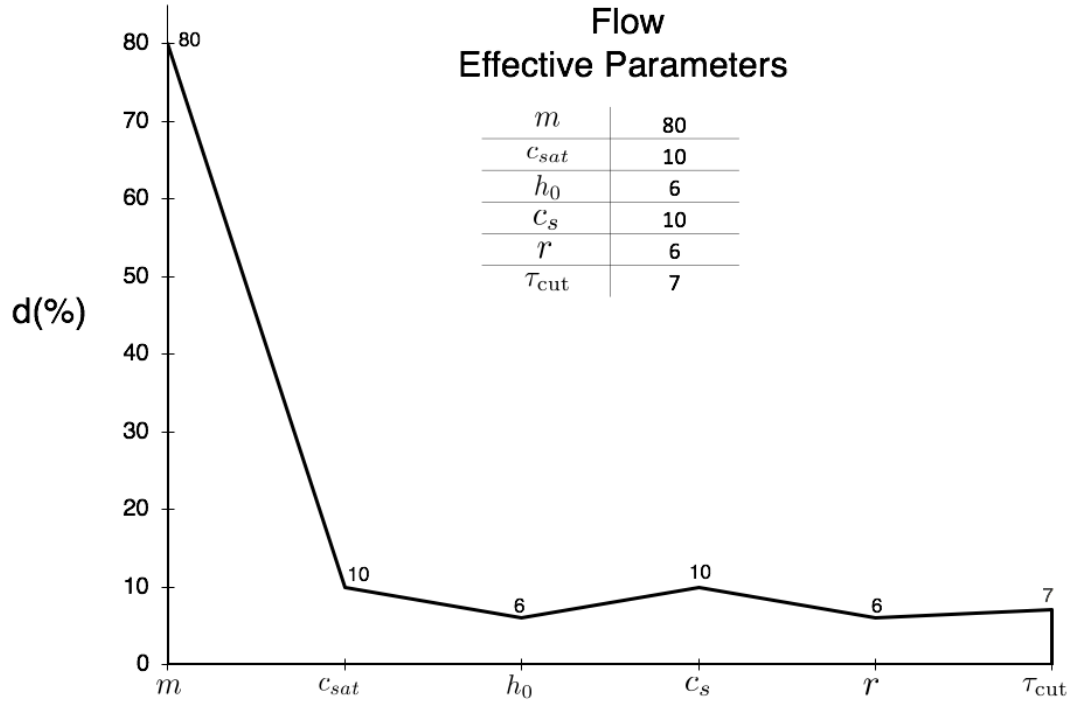

Figure 4.10: The deviation percentage of the prioritized parameters on the flow strength.

5. MICRO-SCALE CRYSTAL PLASTICITY ANALYSIS

5.1 Micro-scale Constitutive model

In general, the significant effects of size on responses of metallic lamellars at micro-scale, especially on yield strengths, σ_y, follow the Hall–Petch relation [91, 19], $\sigma_y = \sigma_0 + kd^{-n}$, where σ_0 is the friction stress and k a constant. The exponent n varies from 0.3 to 0.7 depending on the constituents microstructure. In this study, the Hall-Petch relation is considered as an auxiliary correspondence to represent the governing equations in metallic thin films. By utilizing the same backbone of the size-dependent constitutive model developed in the nano-scale, retaining the consistency of the models, the continuity of acquiring responses in metallic nano- and micro-layers are assured. Thereby, with the congruent logics in the micro range of entropic kinetics and the assessments for obtaining the level of influence for each prime features, the constitutive model in micro-scale is proposed as

$$\dot{\gamma}^{\alpha} = \begin{cases} \dot{\gamma}_0^{\alpha} \exp\left\{-\frac{Q_{active}}{k_B T}\left[1-\left(\frac{|\tau^{\alpha}|-\tau^{\alpha}_{\text{pass}}}{\tau^{\alpha}_{\text{cut}}}\right)^{p}\right]^{q}\right\} \text{sgn}(\tau^{\alpha}) & |\tau^{\alpha}| > \tau^{\alpha}_{\text{pass}} \\ 0 & |\tau^{\alpha}| \leq \tau^{\alpha}_{\text{pass}} \end{cases} \tag{5.1.1}$$

in which

$$\dot{\tau}^{\alpha}_{pass} = \sum_{\beta=1}^{N} \mathbf{h}^{\alpha\beta} |\dot{\gamma}^{\beta}| \tag{5.1.2}$$

and

$$\mathbf{h}^{\alpha\beta} = \begin{cases} \sum_{\beta=1}^{N} h_0^{\beta} \left| 1 - \frac{\left|\left|\tau^{\beta}_{\text{cut}} + \tau^{\beta}_{\text{pass}}\right|\right|_2}{\tau^{\beta}_{sat}} \right|^{r} \left[q^{\alpha\beta} + (1-q^{\alpha\beta})\delta^{\alpha\beta}\right] & \left|\left|\tau^{\beta}_{\text{cut}} + \tau^{\beta}_{\text{pass}}\right|\right|_2 \leq \tau^{\beta}_{\text{sat}} \\ 0 & \left|\left|\tau^{\beta}_{\text{cut}} + \tau^{\beta}_{\text{pass}}\right|\right|_2 > \tau^{\beta}_{\text{sat}} \end{cases} \tag{5.1.3}$$

where the parameters have the same descriptions as in the nano-scale.

The size effect is considered through an implicit impact by defining the thermal shear resistance as

a function of size through

$$\tau^{\alpha}_{\text{cut}} = \tau^{\alpha}_{\text{cut-init}} + k_{HP}\, d^{-0.5}\,, \tag{5.1.4}$$

where $\tau_{\text{cut-init}}$ denotes the initial values of the cutting stress.

5.2 Constitutive Parameters

As observed in the developed micro-scale constitutive model and auxiliary relations, nine parameters, as demonstrated in Table 5.1, must be calibrated for each material prior to any further analyses.

Table 5.1: Constitutive parameters to be calibrated for the micro-scale constitutive model.

Constitutive Parameters in Micro-Scale								
$\dot{\gamma}^{\alpha}_{0}$	p	q	r	k_{HP}	τ_{sat}	$\tau_{\text{cut-init}}$	$\tau_{\text{pass-init}}$	h^{β}_{0}

As an instance, Cu/Nb multi-layers are considered in subsequent evaluations for which elastic constants are obtained through analytical processes and databases displayed in Table 5.2.

Table 5.2: Material elastic constants of copper and niobium acquired from analytical processes and databases.

Material Elastic Constants	Cu	Nb
C_{11}(GPa)	168.4	246.0
C_{12}(GPa)	121.4	134.0
C_{44}(GPa)	75.4	28.7
μ(GPa)	48.0	38.0
Q_{active}(J)	$8.05e{-19}$	$8.9e{-19}$
b(m)	$2.56e{-10}$	$2.86e{-10}$

Subsequently, the developed micro-scale constitutive model and the deep-learning SLC method are employed to calibrate and validate the parameters via experimental data.

5.2.1 Copper Parameter Calibration and Validation

For copper, the experimental results from [12] are utilized where two curves are considered for calibration and the other one for validation processes. Each calibration process needs about five to ten runs and each run takes approximately eighty to one hundred and fifty hours with the current (2020) computational accommodations.

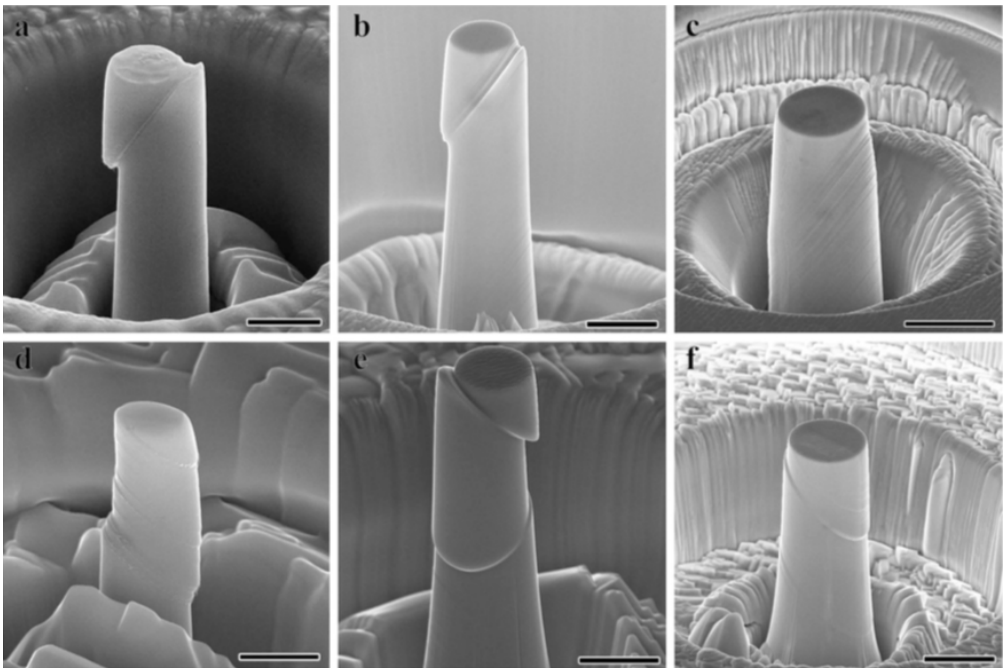

Figure 5.1: Scanning electron microscopy images of micro-pillar compression tests performed on single crystalline copper samples with different sizes. Slip morphologies of the SC1 pillars with (a) 1 μm, (b) 5 μm and (c) 10 μm and the SC2 pillars with (d) 1 μm, (e) 5 μm and (f) 10 μm sizes. The scale bars are the same as each specimen size [12].

The experimental data include the stress-strain curves of two monocrystal copper pillars named SC1 and SC2 with the orientations of $\langle 345 \rangle$ and $\langle 136 \rangle$, respectively, under compression loading with strain rates of 3 to 5 $/sec$ and the sizes of 1 μm, 5 μm and 10 μm as illustrated in Fig. 5.1. Representative compressive stress-strain curves indicating the growth of flow stress with size are

demonstrated in Fig. 5.2. The compression test is performed for two specimens with similar thicknesses as "size of the sample – number of the sample", e.g., 1-1 and 1-2 specify 2 samples with 1 μm thicknesses.

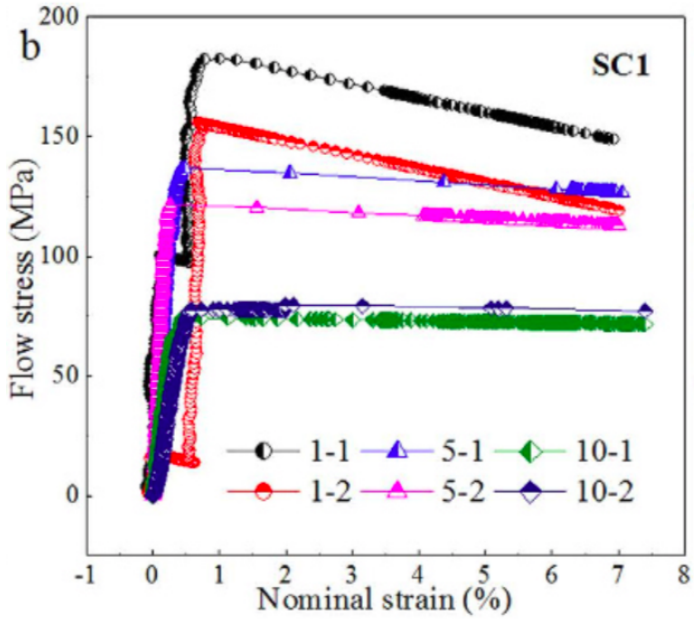

(a)

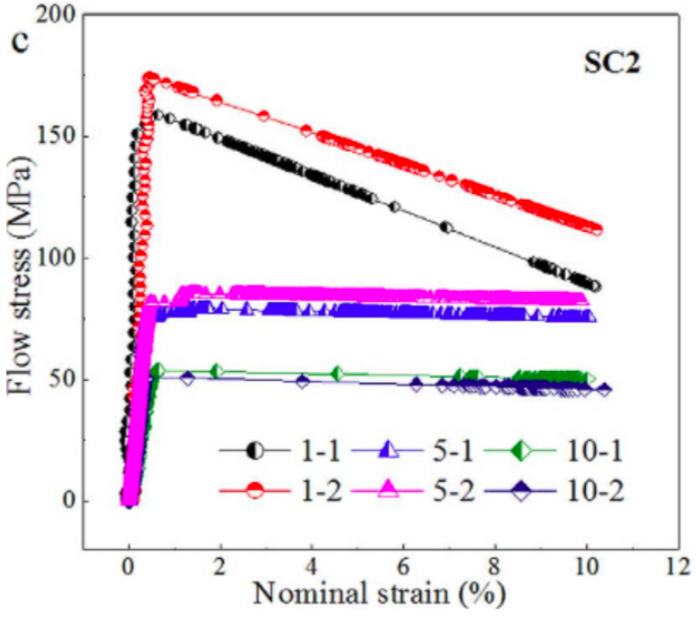

(b)

Figure 5.2: (a) Stress-strain curves of two copper single crystalline samples, SC1 and SC2, with two orientations of (a) ⟨345⟩ and (b) ⟨136⟩ [12]. These curves along with the developed micro-scale constitutive model and the deep-learning SLC method are employed to calibrate and validate the constitutive parameters.

The exhibited curves are utilized in calibration process for which two curves of each orientation is considered and the results are displayed in Fig. 5.3.

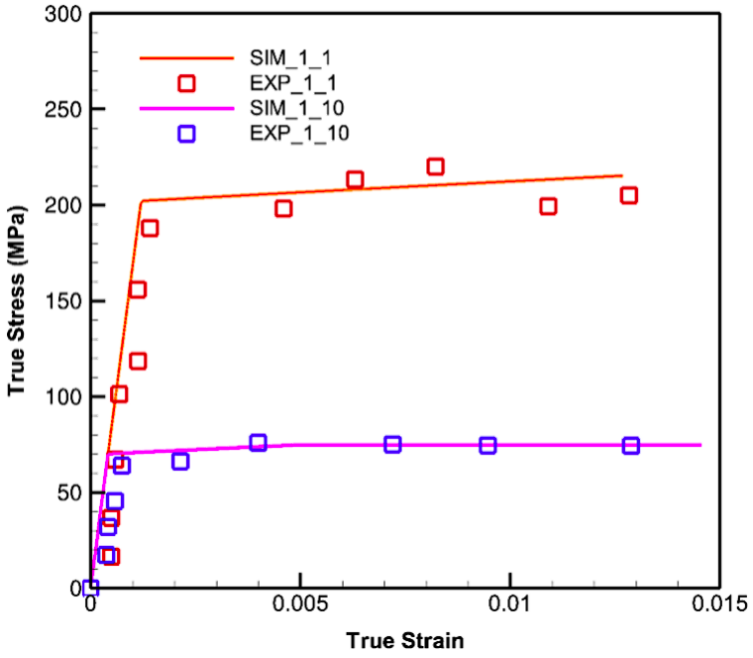

(a)

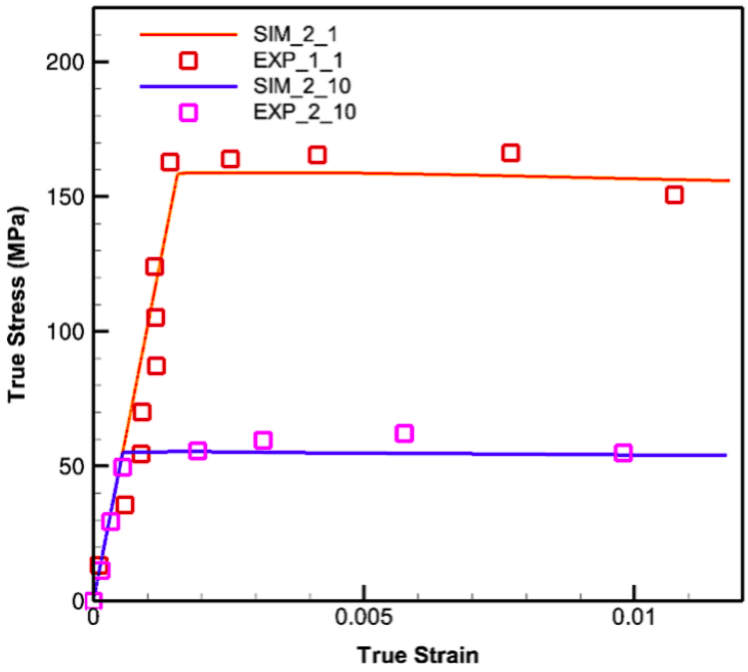

(b)

Figure 5.3: Calibration curves with the developed micro-scale constitutive model and the deep-learning SLC by the experimental data [12] for (a) SC1 and (b) SC2 specimens.

Accordingly, the calibrated parameters are shown in Table 5.3.

Table 5.3: Calibrated parameters of copper through the developed micro-scale constitutive model, deep-learning SLC, and experimental data.

Copper Calibrated Constitutive Parameters	
$\dot{\gamma}_0^{\alpha}$	5.0e6
p	1.0
q	1.0
r	1.115
k_{HP}	60,000.0
τ_{sat}(MPa)	50.0
$\tau_{\text{cut-init}}$(MPa)	15.0
$\tau_{\text{pass-init}}$(MPa)	15.0
h_0^{β}	50.0

At this point, the parameters are validated by the rest of the curves in SC1 and SC2 specimens as illustrated in Fig. 5.4 with favorable agreements.

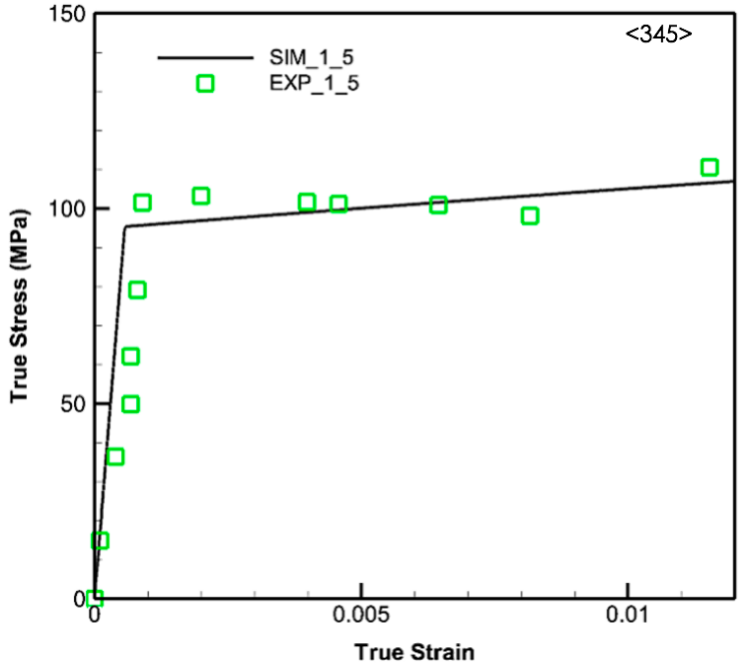

(a)

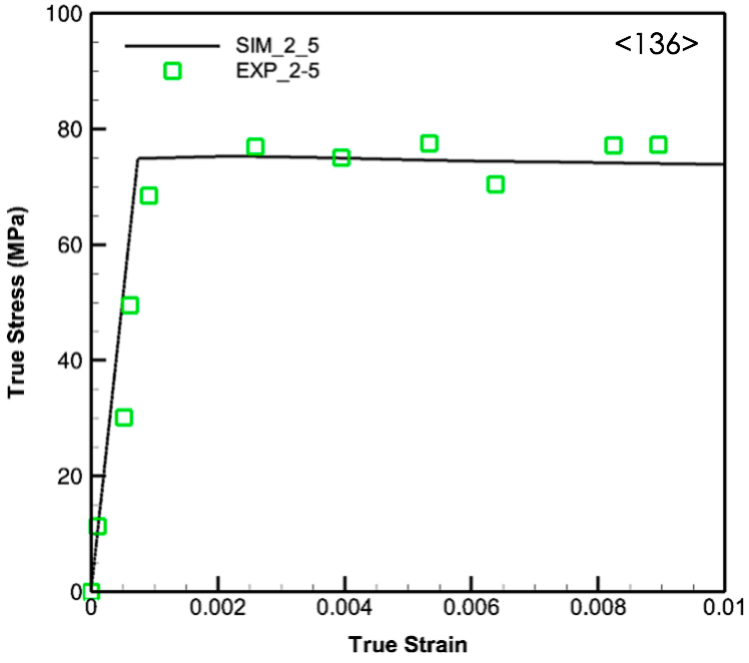

(b)

Figure 5.4: Validation curves of the calibrated parameters in Table 5.3 with the rest of the curves in (a) SC1 and (b) SC2 with solid agreements.

5.2.2 Niobium Parameter Calibration and Validation

For niobium, the experimental results from [13] are utilized where two curves of 1800 μm and 5000 μm are considered for calibration and 2300 μm for validation processes. Each calibration process needs about five to ten runs and each run takes approximately eighty to one hundred and fifty hours with the current (2020) computational accommodations.

The experimental data include the stress-strain curves of single-crystalline niobium pillars with the orientation of $\langle 001 \rangle$ under compression loading with stress rates of 33 ± 23 MPa/sec as illustrated in Fig. 5.5.

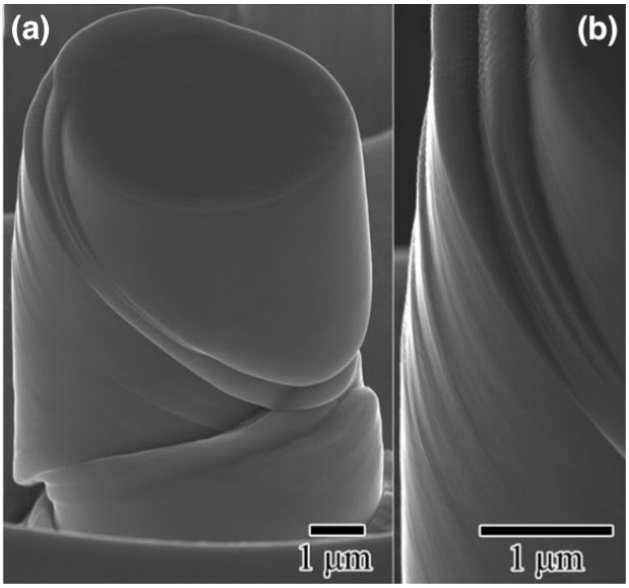

Figure 5.5: Scanning electron microscopy images of micro-pillar compression tests performed on a single crystalline niobium sample with (a) 5000 μm size generating (b) inclined slip morphologies [13].

Representative compressive stress-strain curves indicating the growth of flow stress with size are displayed in Fig. 5.6 specifying the higher extent of size effects on the overall responses of niobium at lower length spectrum as discussed in the nano-scale regime.

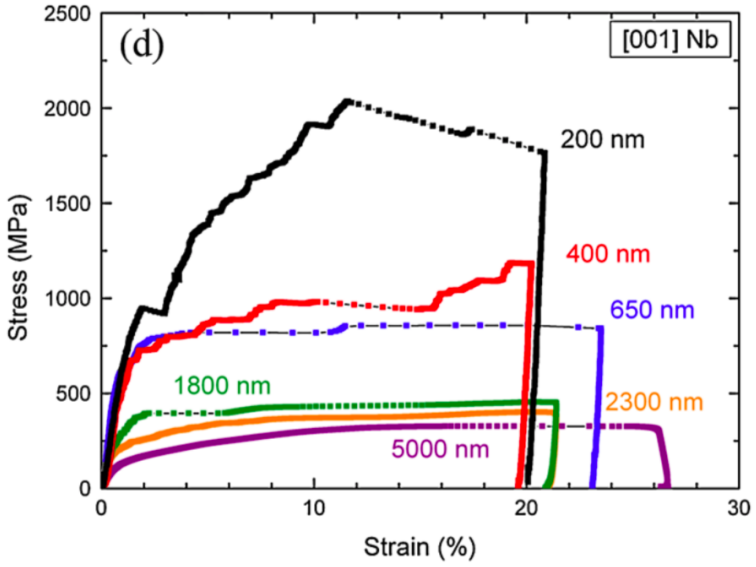

Figure 5.6: Stress-strain curves of micro-pillar compression tests performed over single-crystalline niobium samples [13].

The micro curves, 1800 μm, and 5000 μm are utilized for the calibration process through the developed micro-scale constitutive model and deep-learning SLC where the result plots are displayed in Fig. 5.7.

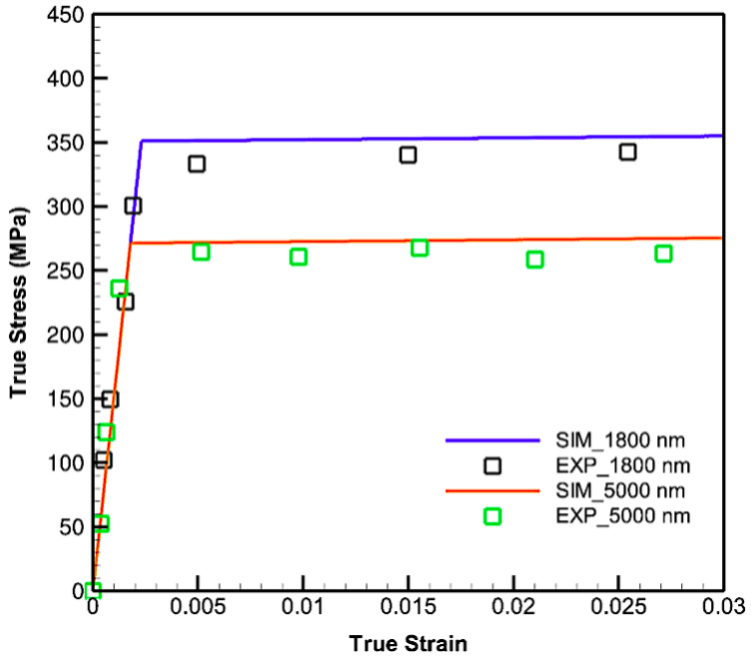

Figure 5.7: Calibration curves with the developed micro-scale constitutive model, the deep-learning SLC, and experimental data [13] of 1800 μm and 5000 μm specimens.

Consequently, the calibrated parameters are shown in Table 5.4.

Table 5.4: Calibrated parameters of niobium through the developed micro-scale constitutive model, deep-learning SLC, and experimental data.

Niobium Calibrated Constitutive Parameters	
$\dot{\gamma}_0^{\alpha}$	5.0e6
p	1.0
q	1.0
r	1.115
k_{HP}	125,000.0
τ_{sat}(MPa)	200.0
$\tau_{\text{cut-init}}$(MPa)	10.0
$\tau_{\text{pass-init}}$(MPa)	70.0
h_0^{β}	50.0

At this point, the parameters are validated by a 2300 nm curve as illustrated in Fig. 5.8 with favorable agreements.

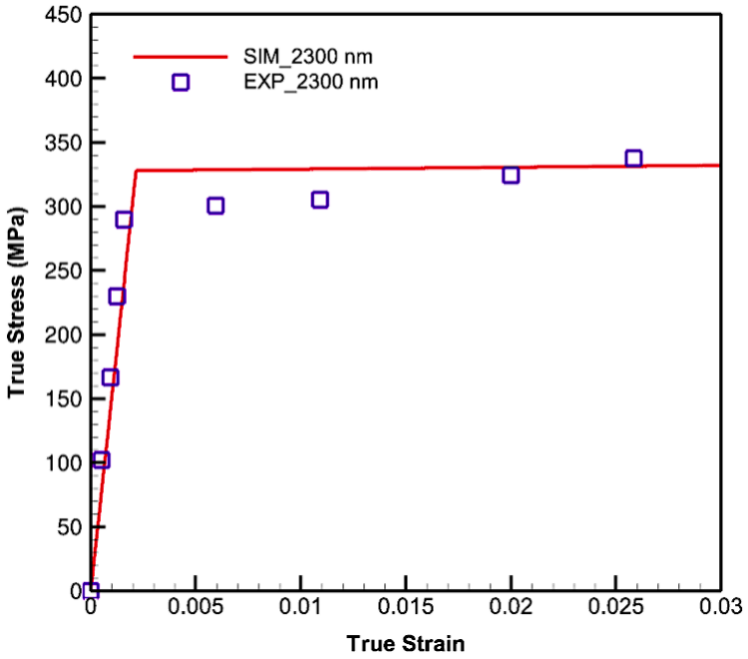

Figure 5.8: Validation curves with the calibrated parameters demonstrated in Table 5.4 with the 2300 nm curve.

6. PRECIPITATE STRENGTHENING

6.1 Introduction

Precipitates are dispersed second-phase particles within the original phase matrix of metals or metallic alloys enhancing associated mechanical responses. Precipitates are generally spread inside a lattice by several volume fractions through synthetic positioning, powder pressing and sintering, heat treatments, and so forth.

The associated strengthening mechanism as an increase in the stress required to cause plasticity due to previous inelastic deformation is originated by dislocations interacting with barriers that impede their motion through the crystal lattice via creating back-stresses [92].

The most important contribution to the interaction between a point or volume defect and dislocation is usually due to hindrance of dislocation glide [93] and a distortion produced in the surrounding crystal which interacts with the stress field of the dislocation to raise or lower the elastic strain energy of the crystal.

6.2 Ellipsoidal Inclusion

A generic model of an inclusion is illustrated in Fig. 6.1 [94] based on Eshelby's method [95]. If S is the surface separating the matrix and inclusion, and n_i its outward normal, Eshelby suggested to solve the problem which is summarized by the following steps.

1. Remove the inclusion and let it undergo the strain of ε_{ij}^T without altering its elastic constants. The stress for small kinematics will be

$$\sigma_{ij}^T = \check{\lambda}\varepsilon_{kk}^T\delta_{ij} + 2\check{\mu}\varepsilon_{ij}^T \,, \tag{6.2.1}$$

   where $\check{\lambda}$ and $\check{\mu}$ are Lame's constants and δ_{ij} is the Kronecker delta function. At this stage, the stress in the inclusion and matrix is zero.

2. Apply surface tractions $\sigma_{ij}^T n_j$ to the inclusion. This brings it back to the shape and size it had before the transformation. Put it back in the matrix and reweld across S. The surface forces have now become a layer of body force spread over S.

3. Let these body forces relax, or, what comes to the same thing, apply a further distribution $\sigma_{ij}^T n_j$ over S. The body is now free of external force but in a state of self-stress because of the inclusion transformation.

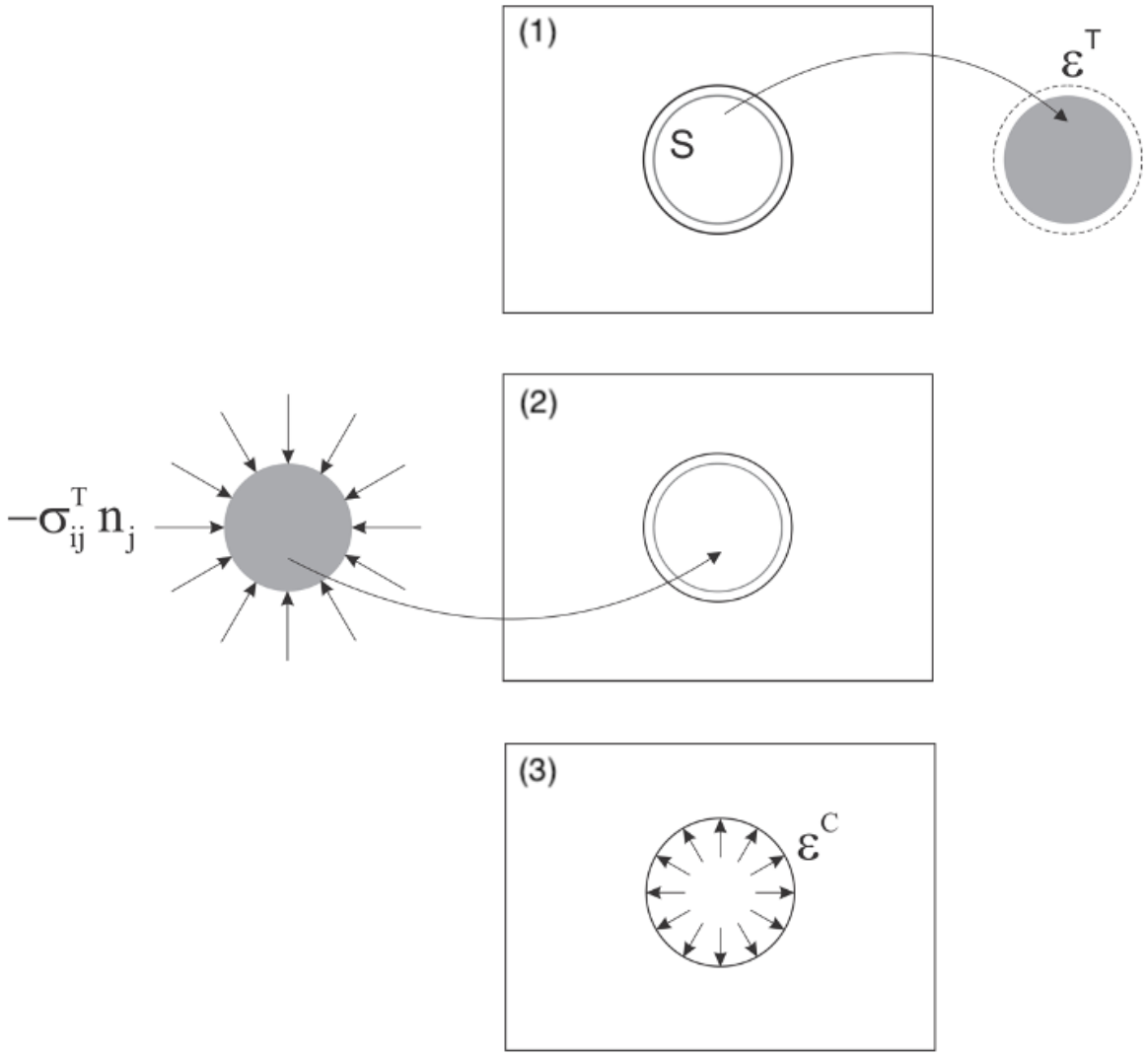

Figure 6.1: General Inclusion theory based on Eshelby's Method.

Since the displacement at a distance, $\mathbf{r}$, due to a point-force F_i is [96]

$$U_j(\mathbf{r}-\mathbf{r\prime}) = \frac{1}{4\pi\breve{\mu}}\frac{F_j}{|\mathbf{r}-\mathbf{r\prime}|} - \frac{1}{16\pi\breve{\mu}(1-\nu)}F_l\frac{\partial^2}{\partial x_l \partial x_j}|\mathbf{r}-\mathbf{r\prime}|\,, \tag{6.2.2}$$

the displacement impressed on the material in stage 3 will be

$$u_i^C(\mathbf{r}) = \int_S \sigma_{jk}^T U_j(\mathbf{r} - \mathbf{r\prime}) dS_k \,, \tag{6.2.3}$$

where ν is the Poisson's ratio. Assuming the end of the stage II as a state of zero displacement since the stress and strain in the matrix are zero and the inclusion has the original geometrical form, u_i^C is the actual displacement in the matrix and inclusion. Thus, the strain in matrix or inclusion can be determined with

$$\varepsilon_{ij}^C = \frac{1}{2}\left(u_{i,j}^C + u_{j,i}^C\right) \,. \tag{6.2.4}$$

Considering that the inclusion had the stress of $-\sigma_{ij}^T$ before stage 3, the net inclusion stress is

$$\sigma_{ij}^I = \sigma_{ij}^C - \sigma_{ij}^T = \check{\lambda}(\varepsilon_{kk}^C - \varepsilon_{kk}^T)\delta_{ij} + 2\check{\mu}(\varepsilon_{ij}^C - \varepsilon_{ij}^T) \,. \tag{6.2.5}$$

At this point, by incorporating Gauss theorem, the displacement in the matrix can be rewritten as

$$u_i^C(\mathbf{r}) = \frac{1}{16\pi\check{\mu}(1-\nu)}\sigma_{jk}^T \Psi_{,ijk} - \frac{1}{4\pi\check{\mu}}\sigma_{ik}^T \Phi_{,k} \,, \tag{6.2.6}$$

where for the volume boundary, V,

$$\Psi = \int_V \frac{dV}{|\mathbf{r} - \mathbf{r\prime}|} \quad , \quad \Phi = \int_V |\mathbf{r} - \mathbf{r\prime}| dV \,. \tag{6.2.7}$$

For a pure dilatation when $\varepsilon_{ij}^C = \frac{1}{3}\varepsilon\delta_{ij}$, the strain becomes

$$\varepsilon_{il}^C = \frac{1}{4\pi}\,\frac{(1+\nu)}{3(1-\nu)}\varepsilon\Phi_{il} \,. \tag{6.2.8}$$

In a special case when a uniform inclusion misfit is considered, as shown in Fig. 6.2, the point defect is assumed an elastic sphere of natural radius $r_a(1+\delta)$ and volume V_s, which is inserted into a spherical hole of radius r_a and volume V_h in an elastic matrix.

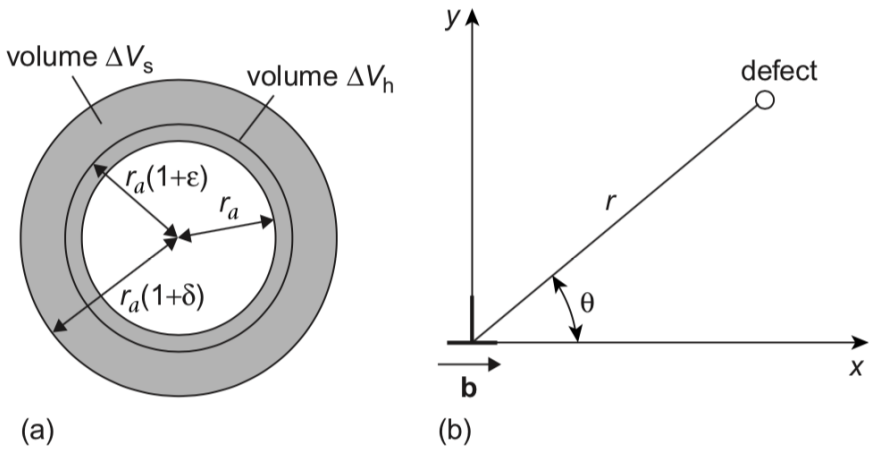

Figure 6.2: (a) Elastic model for a defect of natural radius $r_a(1+\delta)$ inserted in a hole of radius r_a. The final radius is $r_a(1+\varepsilon)$. (b) Geometry for the interaction of a defect with a dislocation lying along the z axis [14].

The sphere and matrix are isotropic with the same shear modulus, μ, and Poisson's ratio, ν. The difference between the defect and hole volumes can be defined as

$$V_{mis} = V_s - V_h = \frac{4}{3}\pi r_a^3(1+\delta)^3 - \frac{4}{3}\pi r_a^3\,, \tag{6.2.9}$$

which in the case of infinitesimal misfit ($\delta << 1$), it can be approximated by

$$V_{mis} \approx 4\pi r_a^3 \delta\,. \tag{6.2.10}$$

The misfit parameter δ is positive for oversized defects and negative for under-sized ones. On inserting the sphere in the hole, a final defect radius of $r_a(1+\varepsilon)$ is generated that changes V_h by ΔV_h as

$$\Delta V_h = \frac{4}{3}\pi r_a^3(1+\varepsilon)^3 - \frac{4}{3}\pi r_a^3\,, \tag{6.2.11}$$

which in the case of infinitesimal strain ($\varepsilon << 1$), it can be approximated by

$$\Delta V_h \approx 4\pi r_a^3 \varepsilon\,. \tag{6.2.12}$$

Comparing Eqs. 6.2.8,6.2.10, and 6.2.12, the relation between misfit strain and parameter can be specified with

$$\varepsilon = \frac{1+\nu}{3(1-\nu)}\,\delta \tag{6.2.13}$$

and

$$\Delta V_h = \frac{1+\nu}{3(1-\nu)} V_{mis}\,. \tag{6.2.14}$$

6.3 Orowan Mechanism

The degree of precipitate strengthening depends on the distribution and shape of particles in a matrix. The second-phase dispersion can be described by specifying the volume fraction, average particle diameter, and mean inter-particle spacing. These factors are all interrelated so that one factor cannot be changed without affecting the others. For example, for a given volume fraction of the second phase, reducing the particle size decreases the average distance between particles and for a given size particle, the distance between particles decreases with an increase in the volume fraction.

The precipitates, in general, intersect slip planes in a random fashion and can appear as dense, impenetrable particles where dislocations can move around them by sharp changes in their line curvature, or as coherent ones through which dislocations can pass at stress levels higher than those required to move in the matrix phase. A dislocation will adopt the mechanism offering the lowest resistance. Therefore, dislocations motions are opposed by the precipitates in two distinct ways, cutting and bypassing.

This study centers on the bypassing dislocation mechanism, where cutting particles becomes unfavorable, and instead dislocations move around them. This phenomenon is commonly associated with non-coherent particles with larger numbers of constituent atoms, $N > 10^5$. In these cases, the Orowan mechanism [97] is the dominant governing relation as displayed in Fig. 6.3. Stage 1 shows a straight dislocation line approaching two particles. At stage 2 the line is beginning to bend, and at stage 3 it has reached the critical curvature. Now the dislocation can move forward without further decreasing its radius of curvature.

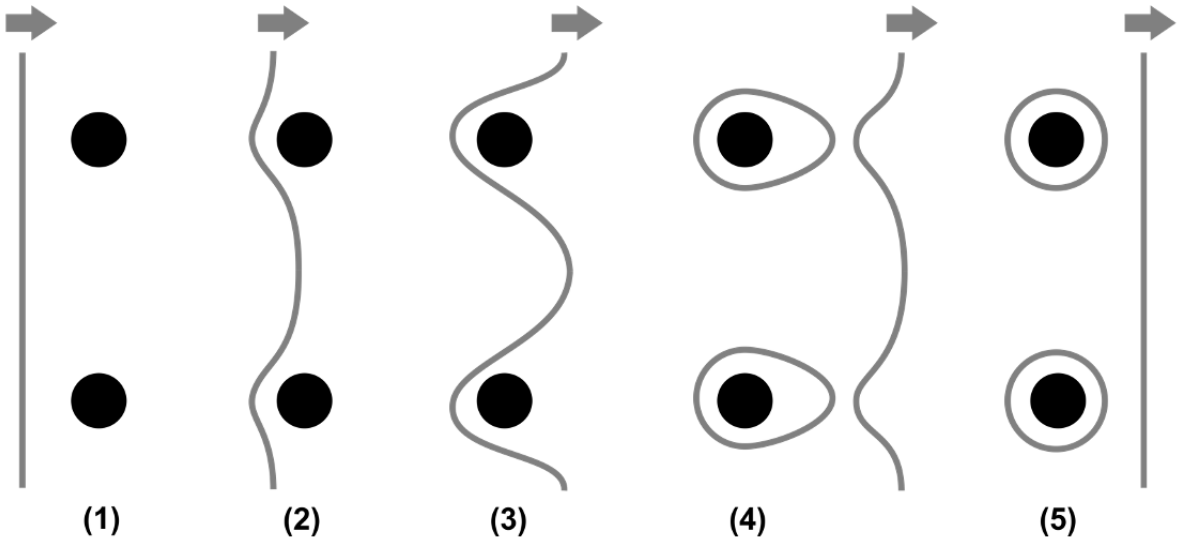

Figure 6.3: Stages in precipitate strengthening through dislocation motion between widely separated obstacles based on Orowan's mechanism of dispersion hardening.

When a uniform shear stress, τ, acts on a dislocation line, moves it forward as demonstrated in Fig. 6.4. Here, the dislocation line travel in the direction of its Burgers vector, b, and a line element of the dislocation, ds, displaces by dl distance along the slip direction. The area swept out by the line element is $ds\,dl$ corresponding to an average displacement of the crystal above to the crystal below the slip plane, i.e., $(dsdl/A)b$, where A is the area of the slip plane.

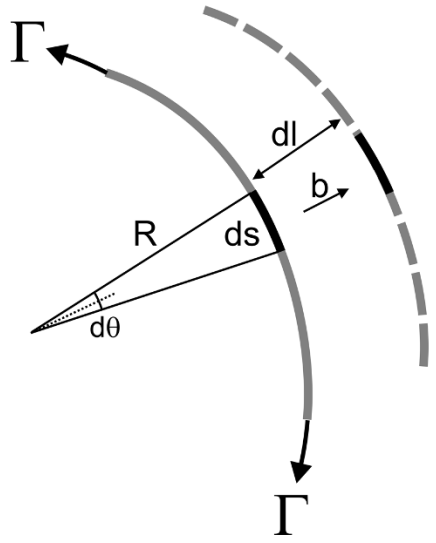

Figure 6.4: The motion of a dislocation line under applied forces.

The applied force creating the shear stress is τA, thus, the work done when the increment of slip occurs is

$$dW = \tau A \left(\frac{dsdl}{A} \right) b \, . \tag{6.3.1}$$

Thereby, the force per unit length of a dislocation line will be

$$F = \frac{dW}{dsdl} = \tau b \, . \tag{6.3.2}$$

This force is normal to the dislocation line at every point along its length toward the unslipped part of the glide plane. Since the Burgers vector is constant along a curved dislocation line, if τ is constant, the value of F will be the same at any point along while its direction is normal to the dislocation line. As a result, the force on a dislocation is not necessarily in the same direction as the applied stress. Since the strain energy of a dislocation line is proportional to its length, increasing dislocation line is opposed by a line tension, Γ, to minimize its energy via shortening and straighten out its length. Thus, in order for a dislocation line to remain at a radius of curvature, R, the following relation according to Fig. 6.4 must be satisfied.

$$\Gamma d\theta = \tau b ds \, , \tag{6.3.3}$$

which yields

$$\tau = \frac{\Gamma}{bR} \, , \tag{6.3.4}$$

where the angle subtended by the line element, ds, is $d\theta = \frac{ds}{R}$, the outward force on the dislocation line is $\tau b ds$, and the opposing inward force due to the line tension for small values of $d\theta$ is considered $\Gamma d\theta$. Due to the fact that Γ is an energy per unit length, a good approximation can be made with

$$\Gamma \approx \frac{\mu b^2}{2} \, , \tag{6.3.5}$$

with μ as the shear modulus. Thereby, the shear stress required to bend a dislocation to radius R can be specified through

$$\tau \approx \frac{\mu b}{2R} \,. \tag{6.3.6}$$

Going back to the Orowan mechanism in Fig. 6.3, at stage 3, the dislocation can then move forward without further decreasing its radius of curvature. By defining interparticle spacing, λ, as

$$\lambda = \frac{4r(1-f)}{3f} \,, \tag{6.3.7}$$

where f is the volume fraction of spherical particles of radius r, or

$$\lambda = \frac{a}{f_a^{\frac{1}{3}}} \,, \tag{6.3.8}$$

where a is the interatomic spacing and f_a the atomic fraction, the stress required to force the dislocation between the obstacles is expressed with

$$\tau_{Orowan} = \alpha \frac{\mu b}{\lambda} \,, \tag{6.3.9}$$

where α is a constant can approximately be considered in the range of $(0.8 - 2)$. If the spacing of incoherent precipitates is not large in comparison with their size, this relation is modified as

$$\tau_{Orowan} = \alpha \frac{\mu b}{(\lambda - 2r)} \,, \tag{6.3.10}$$

This relation can also be modified by introducing more detailed estimates of the dislocation line tension, the mean free path, and dislocation segments interactions on either side of the particle as

$$\tau_{Orowan}^{modified} = \frac{0.13\mu b}{\lambda} \ln \frac{r}{b} \,. \tag{6.3.11}$$

At stage 4, the segments of the dislocation that meet on the other side of the particle are of opposite sign, so they can annihilate each other over part of their length, leaving a dislocation loop around

each particle. Finally, stage 5 displays the original dislocation that is free to move on. Another expression for the stress required to bow a dislocation between particles is identical to the equation for the operation of a Frank-Read source [98] that considers λ as the mean distance between two precipitates and postulates the equality between the force on the dislocation, $\tau b\lambda$ and twice the line tension, $2\mu b^2$, as

$$\tau = 2\left(\frac{\mu b}{\lambda}\right) , \tag{6.3.12}$$

Every dislocation gliding over the slip plane builds up dislocation loops around the particles which exert a back-stress on dislocation sources to be overcome for the additional slip. The Orowan loop reduces the effective spacing, $(\lambda - 2r)$ whose impacts can be mathematically observed in modified Orowan equations. The presence of opposing stress necessitates an increase in shear stress which is considered the reason that dispersed particles cause the matrix to strain-harden rapidly. In addition, these repulsive loops effectively decrease the value of particle spacing which also aid the increase in the required applied stress to pass.

For a given volume fraction, the average precipitates distance decreases with finer particles. An estimate of the effect of particle size can be made by assuming the particles intersecting the slip plane are arranged in a square pattern as it is cut on the slip plane. Then the area fraction equals the volume fraction, $f = \frac{\pi r^2}{d^2}$ or $d = r\frac{\pi}{f}$. By substituting this into Eq. 6.3.12 it yields

$$\tau = 2\left(\frac{\mu b}{r}\right)\left(\frac{f}{\pi}\right)^{\frac{1}{2}} . \tag{6.3.13}$$

Because the increase of yield strength, σ_y, caused by the precipitate particles is proportional to the shear stress, it can be expressed with

$$\sigma_y = \beta\left(\frac{\mu b}{r}\right) f^{\frac{1}{2}} , \tag{6.3.14}$$

where β is a constant. This predicts that the strength increases with increasing volume fraction and decreasing particle size.

6.4 Precipitate Strengthening in Metallic Nano-Layers Case Studies

In this section, the effects of precipitates on the mechanical properties of metallic nano-layers are studied through Cu/Nb cases with tungsten precipitates where the developed nano-scale constitutive model, SLC method, and back-stresses induced by tungsten precipitates based on the Orowan mechanism are considered.

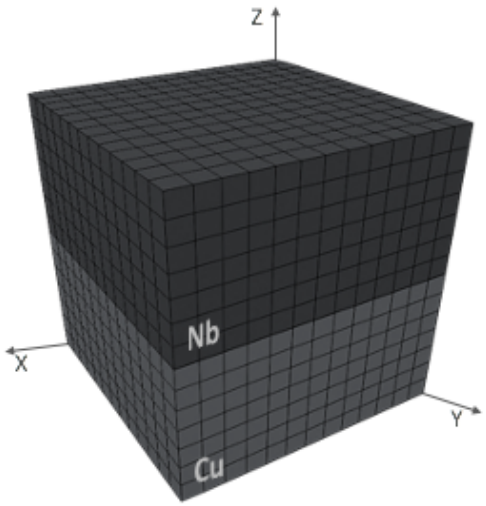

Cases	W Precipitates Percentage	
	Layer (Cu)	Layer (Nb)
Case NP	0	0
Case LP-1	2	0
Case LP-2	0	2
Case LP-3	2	
Case MP-1	5	0
Case MP-2		5
Case MP-2	5	
Case HP-1	15	
Case HP-2		15
Case HP-2	15	

Loading Direction	Z
Layer Thickness	63 nm
Strain Rate	10^{-3} /sec
Orientation Relation	Kurdjumov-Sachs

Figure 6.5: Information summary of the simulated case studies for precipitate strengthening.

The results are demonstrated in the forms of stress contours and stress-strain curves where different precipitates volume fractions are considered in each and both layers. The Kurdjumov-Sachs (KS) orientation relationships, {111} Cu || {110} Nb is assumed with the strain rate of 10^{-3} $/sec$. The layers have an identical thickness of 63 nm under transverse loading. Low precipitate (LP) cases have 2 %, medium precipitate (MP) cases include 5 %, and high precipitate (HP) cases contain 15 % randomly distributed tungsten in volume. The summary of the simulated cases is illustrated in Fig. 6.5. The stress contours are captured at 10% strain.

6.4.1 Low Precipitate Case Studies

Here, three cases of Cu/Nb nano-layers are shown containing 2 % tungsten particles randomly distributed in each and both layers. The stress contours displayed in Fig. 6.6, 6.7, and 6.8 represent the cases where the precipitates are distributed in Cu, Nb, and Cu/Nb, respectively. The rest of the simulation settings are according to what demonstrated in Fig. 6.5.

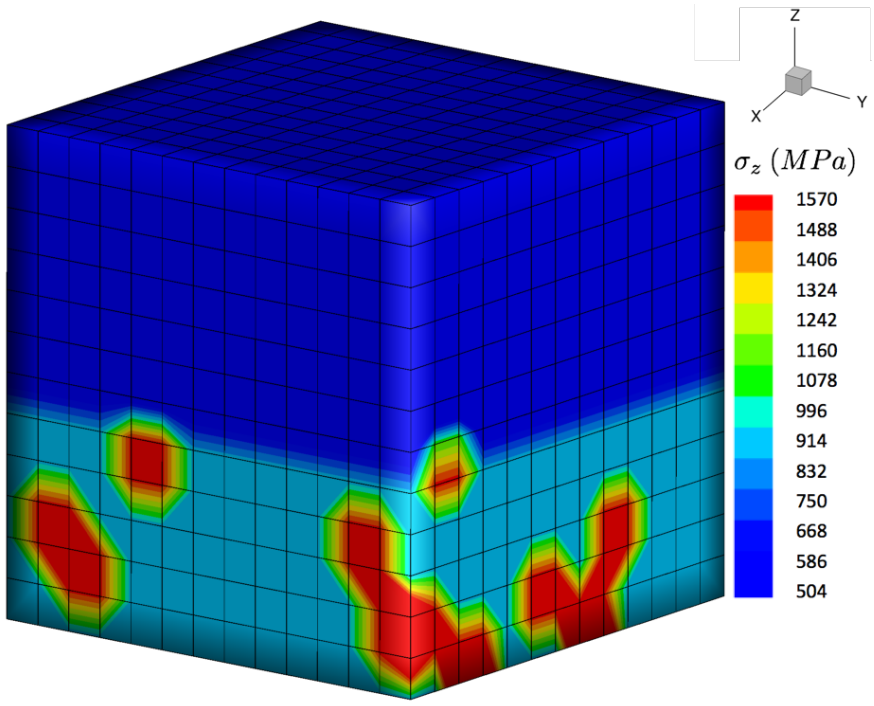

Figure 6.6: Stress contour of the simulated Cu/Nb nano-layers with W precipitates randomly distributed in Cu.

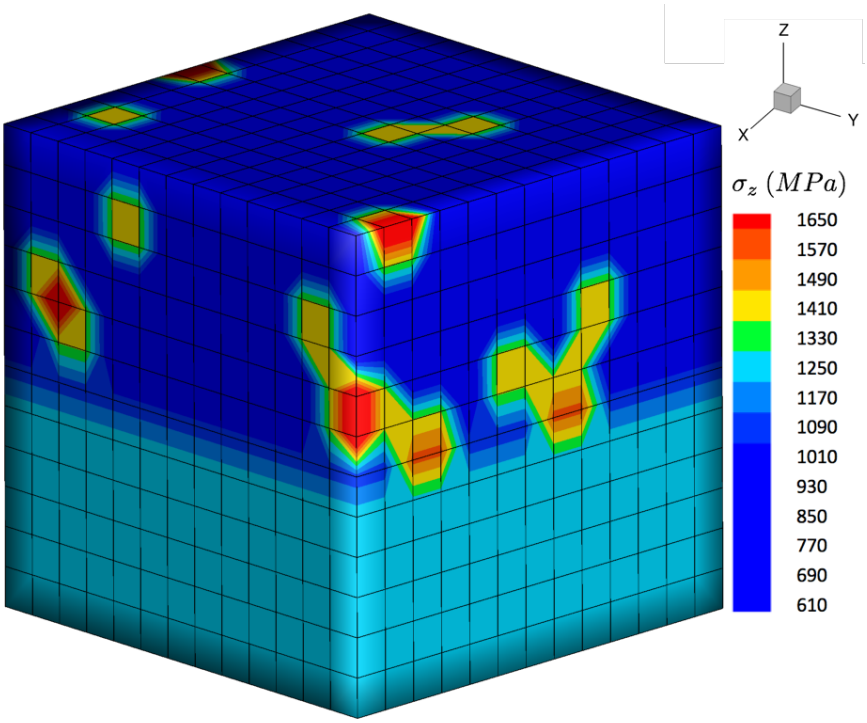

Figure 6.7: Stress contour of the simulated Cu/Nb nano-layers with W precipitates randomly distributed in Nb.

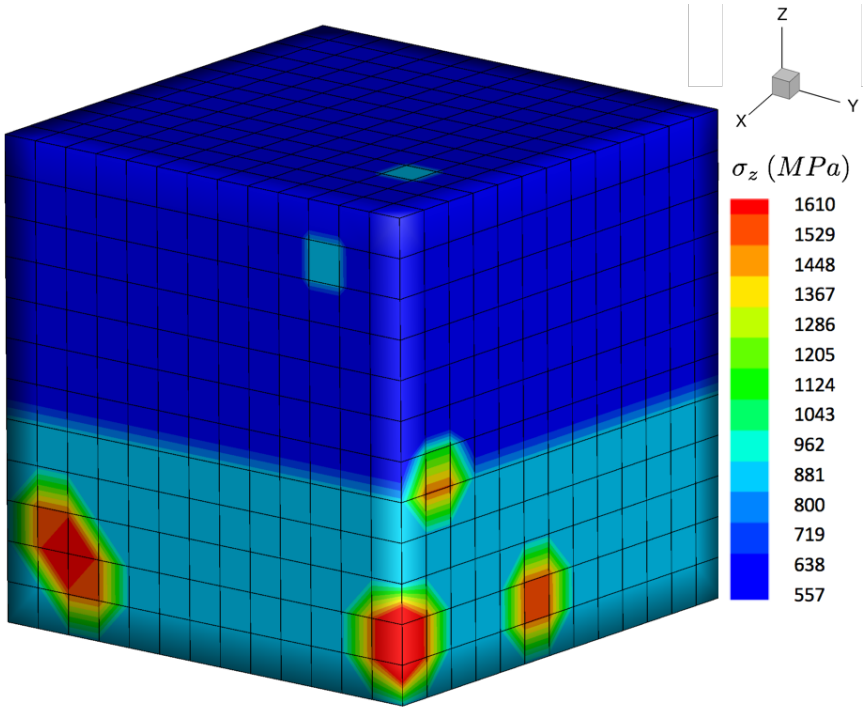

Figure 6.8: Stress contour of the simulated Cu/Nb nano-layers with W precipitates randomly distributed in Cu and Nb.

As observed, the highest values of stress are carried by the precipitates and their surroundings. The high intensity of the stress gradient among the particles and matrix is due to the back-stress induced by the precipitates causing a nonuniform distribution of stress within the layers. The intensity of the stress concentration declines with distance from isolated precipitates while resonances when other particles are closed by. Another point to be discerned is the presence of the highest stress magnitude when precipitates are placed within Nb layers and the lowest one in the case that precipitates are distributed within Cu layers. The similar impact was observed in thickness variation where Nb layers have more impacts on the overall behavior of the Cu/Nb nano-layers.

6.4.2 Medium Precipitate Case Studies

Here, three cases of Cu/Nb nano-layers are shown containing 2 % tungsten particles randomly distributed in each and both layers. The stress contours displayed in Fig. 6.9, 6.10, and 6.11 represent the cases where the precipitates are distributed in Cu, Nb, and Cu/Nb, respectively. The rest of the simulation settings are according to what demonstrated in Fig. 6.5.

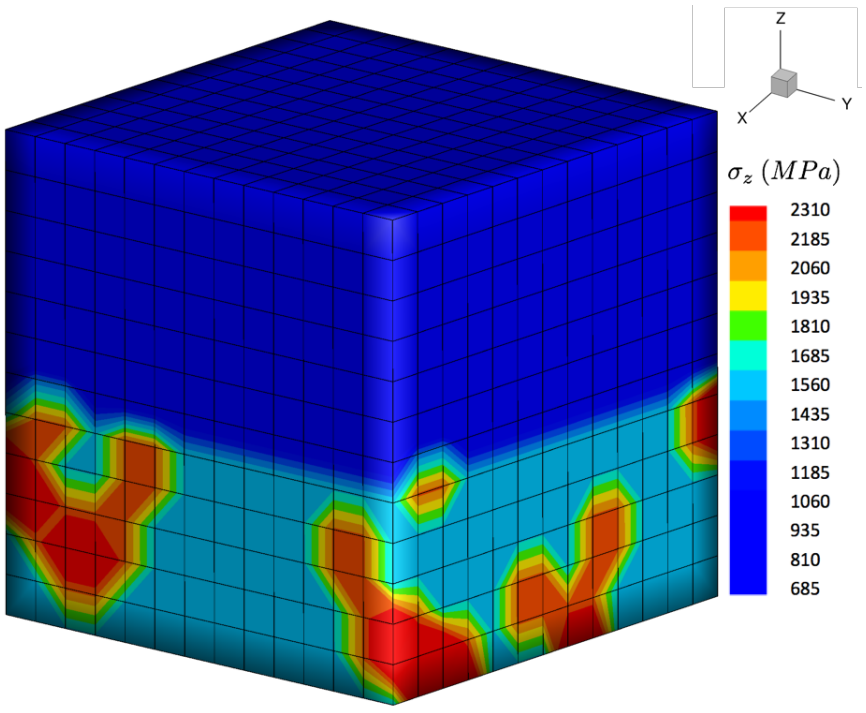

Figure 6.9: Stress contour of the simulated Cu/Nb nano-layers with W precipitates randomly distributed in Cu.

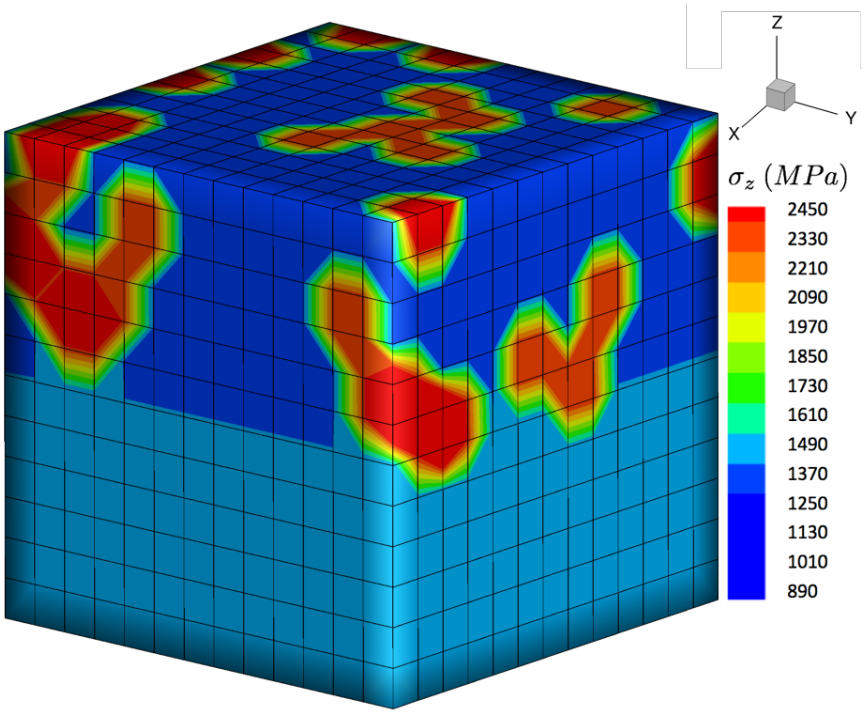

Figure 6.10: Stress contour of the simulated Cu/Nb nano-layers with W precipitates randomly distributed in Nb.

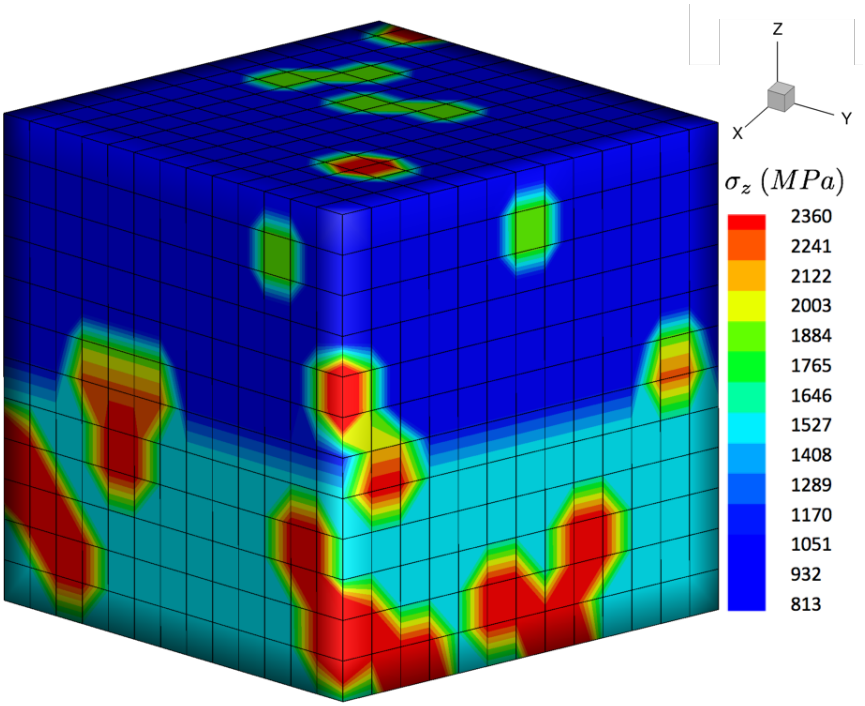

Figure 6.11: Stress contour of the simulated Cu/Nb nano-layers with W precipitates randomly distributed in Cu and Nb.

Based on the demonstrated contours, the highest values of stress are carried by the precipitates and their surroundings. The high intensity of the stress gradient among the particles and matrix is due to the back-stress induced by the precipitates causing a nonuniform distribution of stress within the layers. The intensity of the stress concentration declines with distance from isolated precipitates while resonances when other particles are closed by. Another point to be discerned is the presence of the highest stress magnitude when precipitates are placed within Nb layers and the lowest one in the case that precipitates are distributed within Cu layers. The similar impact was observed in thickness variation where Nb layers have more impacts on the overall behavior of the Cu/Nb nano-layers.

6.4.3 Medium Precipitate Case Studies

Here, three cases of Cu/Nb nano-layers are shown containing 2 % tungsten particles randomly distributed in each and both layers. The stress contours displayed in Fig. 6.12, 6.13, and 6.14 represent the cases where the precipitates are distributed in Cu, Nb, and Cu/Nb, respectively. The rest of the simulation settings are according to what demonstrated in Fig. 6.5.

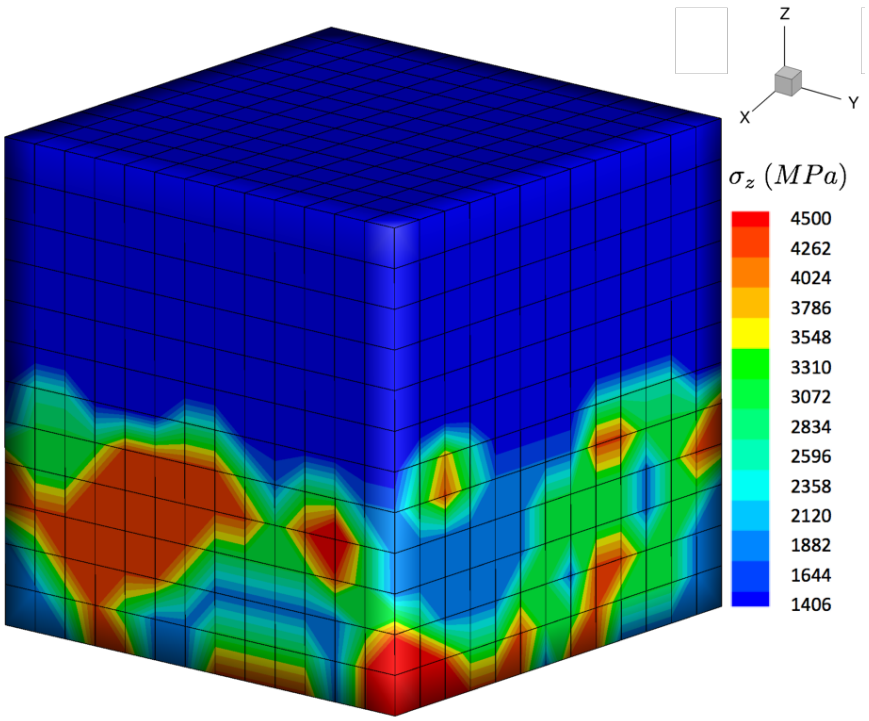

Figure 6.12: Stress contour of the simulated Cu/Nb nano-layers with W precipitates randomly distributed in Cu.

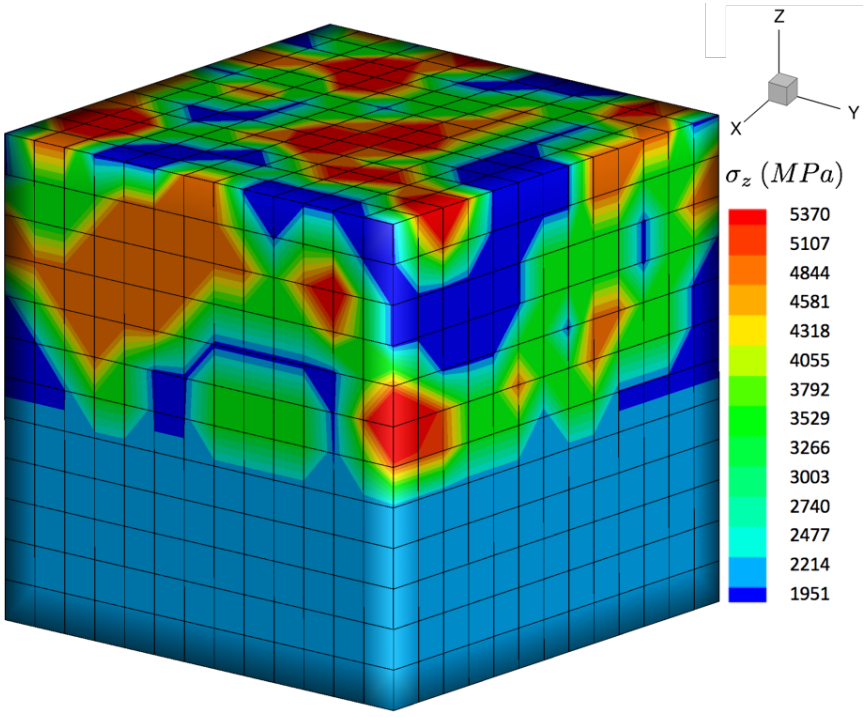

Figure 6.13: Stress contour of the simulated Cu/Nb nano-layers with W precipitates randomly distributed in Nb.

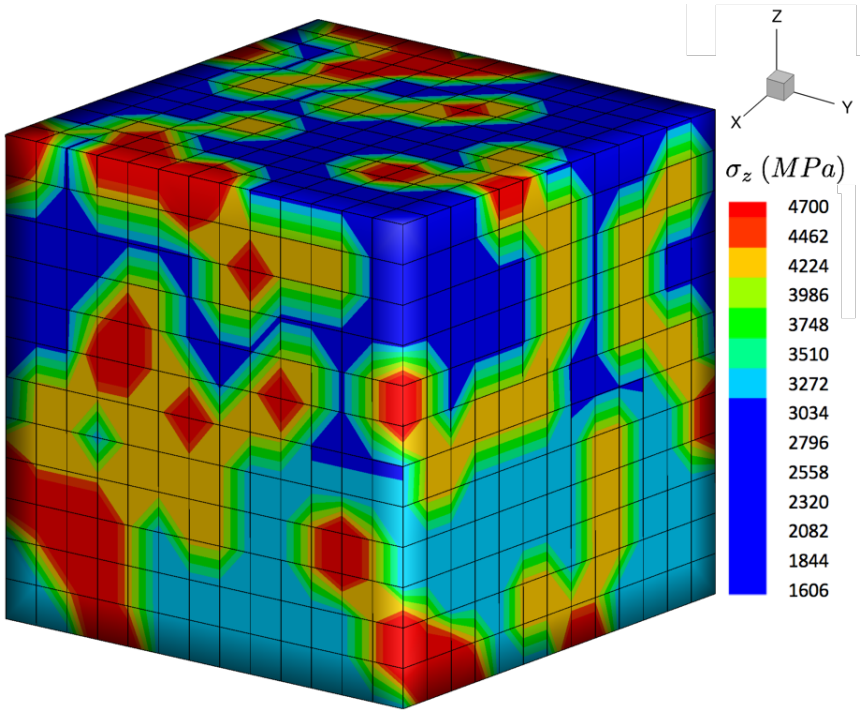

Figure 6.14: Stress contour of the simulated Cu/Nb nano-layers with W precipitates randomly distributed in Cu and Nb.

The results display the highest values of stress are carried by the precipitates and their surroundings. The high intensity of the stress gradient among the particles and matrix is due to the back-stress induced by the precipitates causing a nonuniform distribution of stress within the layers. The intensity of the stress concentration declines with distance from isolated precipitates while resonances when other particles are closed by. Another point to be discerned is the presence of the highest stress magnitude when precipitates are placed within Nb layers and the lowest one in the case that precipitates are distributed within Cu layers. The similar impact was observed in thickness variation where Nb layers have more impacts on the overall behavior of the Cu/Nb nano-layers. With the distribution of 15% precipitates within the layers, the significant changes in the stress absorption of particles in comparison with low and medium concentration cases is observed which results in exponential strengthening effects when the precipitate concentrations among low, medium, and high precipitates are considered.

6.4.4 Precipitate Effects in Constitutive Behavior Case Studies

In this section the stress-strain curves of the Cu/Nb nano-layers are shown containing 2 %, 5 %, and 15 % randomly distributed tungsten in volume. The plots demonstrated in Fig. 6.15, 6.16, and 6.17 represent the cases where the precipitates are distributed in Cu, Nb, and Cu/Nb, respectively.

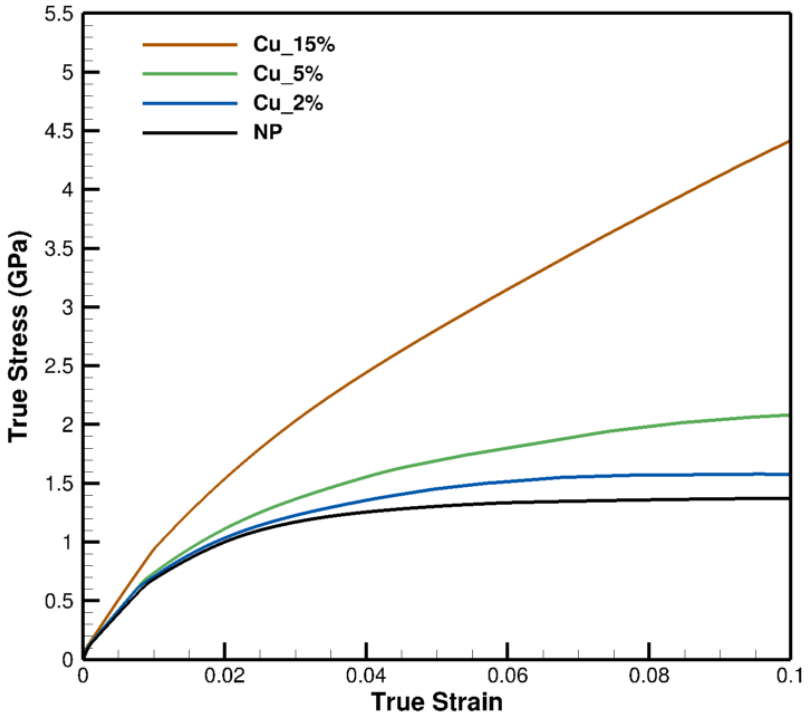

Figure 6.15: Stress-strain curves of contour of the simulated Cu/Nb nano-layers with W precipitates randomly distributed in Cu.

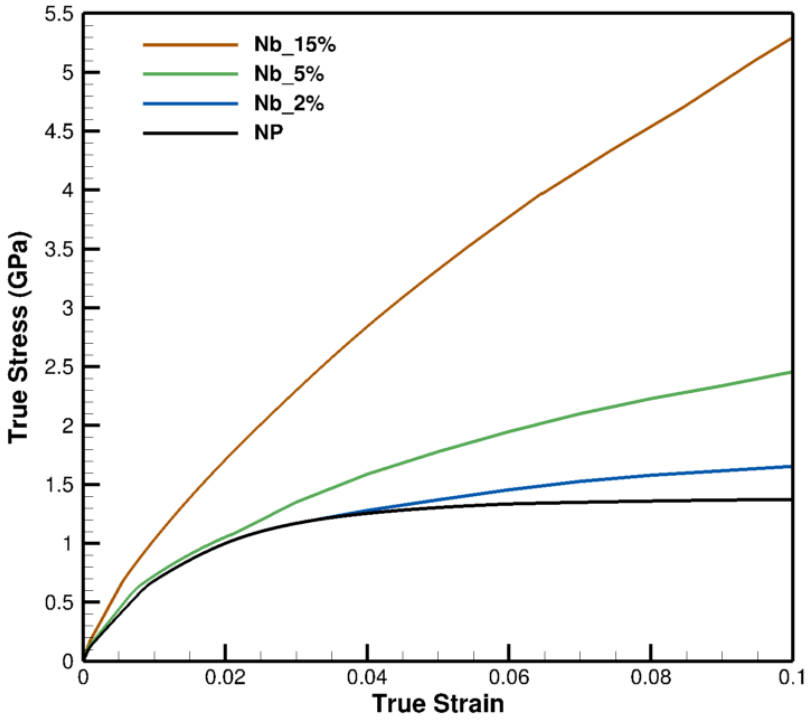

Figure 6.16: Stress-strain curves of contour of the simulated Cu/Nb nano-layers with W precipitates randomly distributed in Nb.

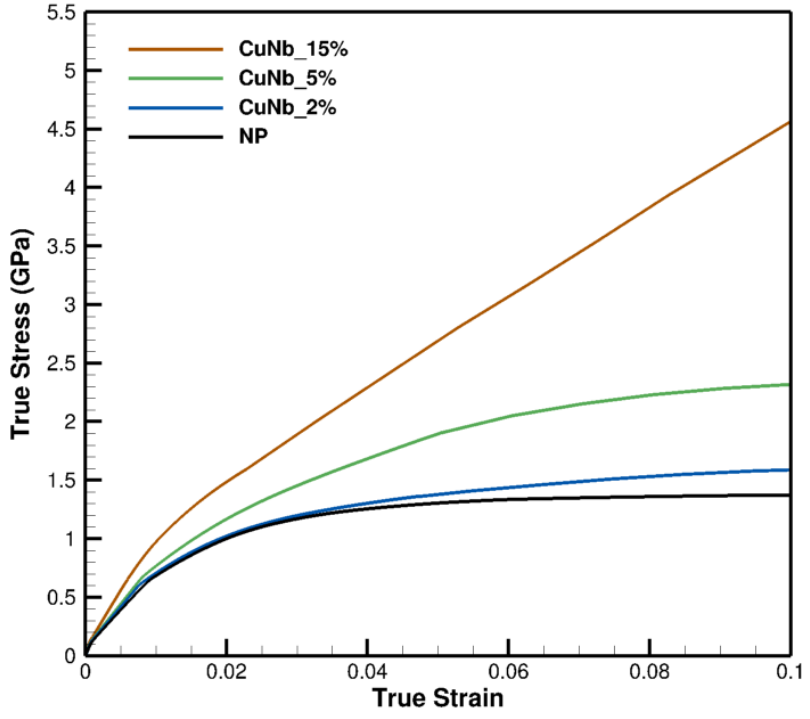

Figure 6.17: Stress-strain curves of contour of the simulated Cu/Nb nano-layers with W precipitates randomly distributed in Cu/Nb.

As noted, adding precipitates to the layers results in the increase of the flow strength and hardening. As demonstrated in Fig. 6.15, 17%, 59%, and 235% increase in flow stress is related to the precipitate volume fraction of 2%, 5%, and 15%, respectively. Hardening has the same trend and it is vividly pronounced at 15% precipitate concentration.

Based on the curves in Fig. 6.16, 23%, 83%, and 300% increase in flow stress is related to the precipitate volume fraction of 2%, 5%, and 15%, respectively. Hardening has the same trend and it is vividly pronounced at 15% precipitate concentration.

From Fig. 6.17, it can be observed that, 20%, 76%, and 250% increase in flow stress is related to the precipitate volume fraction of 2%, 5%, and 15%, respectively. Hardening has the same trend and it is vividly pronounced at 15% precipitate concentration.

Comparing Figs. 6.15, 6.16, and 6.17, shows the significant strengthening occurs by adding precipitates in higher concentrations especially when placed in Nb layers.

7. CONCLUSION

In order to account for the inhomogeneous and high plastic deformation, rate dependence, and anisotropic nature of metallic nano-layers, the crystal plasticity finite element (CPFE) approach in the large deformation platform was utilized in three-dimensional space to mimic the practical cases. Other computational methods including molecular dynamics and discrete dislocation dynamics were found limited in order to acquire accurate and pragmatic predictions, however, the concurrent utilization with CPFE is worth to be considered. The constitutive models, either phenomenological or physics-based, must be accommodating and compatible with the main features of nano-, micro, and homogenized-level, namely, interfaces, dislocation pile-ups, and layers volume fractions, respectively. Additionally, the models must address size effects at each level either in a forward or backward fashion along with the consideration of active mechanisms at each size spectrum in order to reduce excessive computational workload.

At the nano-scale, the size-dependent constitutive model developed based on entropic kinetics addressing size effects both explicitly and implicitly was able to accurately predict the responses of metallic nano-layers under diverse loading conditions at the spatial range of 20 nm to 1 μm below which softening phenomenon must be dealt with considering different mechanisms and models. The associated constitutive parameters were obtained through deep-learning SLC where the behavior of several Cu/Nb nano-layers was predicted. Loading or layer orientation was found to be inconsequential on flow strength at the strain of about 10%. Order combination of Cu/Nb layers with different thicknesses demonstrated the highest flow strength associated with the case having the lowest thickness for both materials while equally increasing the thickness of the layers was under the influence of Nb layers as the dominated constituent affecting the overall behavior of the system. The crucial size effects were observed specifically on the main behavioral features including yield and flow strength as well as transition strain where by decreasing thickness these characteristics exponentially increased especially at the thickness below $\approx$100 nm.

At the micro-scale, the developed constitutive model was able to not only capture Hall-Petch or similar mechanisms while retaining the backbone of the model in the nano-scale, but could predict nano-layers responses considering temperature change, activation energy, and so on which are not possible by simply utilizing the commonly used Hall-Petch relation alone.

The developed homogenized constitutive model was accurately capable of capturing the properties of nano-scale multi-layers while expediting computational processes by several orders of magnitude, e.g., a 25-day running time reduced to a matter of minutes. The deep-learning SLC and genetic algorithms were utilized for obtaining the effective functionals relations and parameters for both homogenized and temperature-dependent constitutive models considering that those relations had different formats and accordingly parameters for each functional. Accordingly, temperature effects were realized by adding other functions and constants to those relations through which several predictive cases of Cu/Nb were presented. Dramatic changes in flow strengths were observed by increasing temperature, specifically, a drop up to $\approx 80\%$ in flow strength at about $1000K$ in 25 nm sample. Moreover, the degradation of a thin nano-layer at high temperature into a thicker one at a lower temperature was observed, namely, a 34 nm sample at $400°C$ functioned as a 63 nm specimen at $25°C$.

Sensitivity analysis was performed on the size-dependent constitutive model as a diagnostic-prognostic field through the factor prioritization in order to capture the influential parameters where the size effects designed parameters, namely, m, c_s, c_{sat}, and h_0 were found the dominant factors on the main behavioral features.

Precipitate hardening phenomenon based on Orowan strengthening mechanism and Eshelby's theorem in nano-systems was considered. The results demonstrated the increase of flow, yield, transition, and hardening at any concentration of precipitates, however, in order to acquire practical strengthening of about 30%, the precipitate concentration more than about 5% is suggested. Larger volume fractions of precipitates yielded higher flow strength and hardening, however, the upper bound must be investigated. For practical cases, Orowan and cutting through mechanisms must be considered in a specific combination to determine the actual responses of strengthened metallic nano-layers considering manufacturing setups and conditions. The element effects were shown with the highest impacts on the overall properties where strengthen Nb demonstrated the strongest case than Cu/Nb, and finally, Cu specifying the role of stronger crystal structure in the precipitate strengthening as well similar to the size effects observed in the order combination cases at nano-scale.

APPENDIX A

General Steps of Solving Equilibrium Equation–FE

1. Equilibrium Equation

   $\int_v \sigma : \delta\mathbf{e}\, dv - \int_\Gamma \mathbf{t}\, \delta\mathbf{v}\, d\Gamma = 0$

2. Finite Element Discretization

   $\delta\mathbf{e} = \dfrac{1}{2}(\delta\mathbf{l} + \delta\mathbf{l}^T)$

   $\mathbf{v} = \sum_{i=1}^{nNode} N_i \hat{\mathbf{v}}_i \;\; \delta\mathbf{l} = \dfrac{\partial\delta\mathbf{v}}{\partial\mathbf{x}} = \sum_{i=1}^{nNode} \hat{\mathbf{v}}_\mathbf{i} \otimes \nabla_x N_i = \nabla_{(\xi,\eta,\zeta)} N_i \left[\sum_{i=1}^{nNode} \mathbf{x}_\mathbf{i} \otimes \nabla_{(\xi,\eta,\zeta)} N_i \right] \hat{\mathbf{v}}$

3. Residual Force

   $\mathbf{R}(\hat{\mathbf{v}}) = \int_v (\nabla_x N_i)^T \sigma dv - \int_s N_i \mathbf{t} \delta d\Gamma = 0$

4. Newton-Raphson Solver

   $\hat{\mathbf{v}}^{n+1} = \hat{\mathbf{v}}^n - \left(\dfrac{\partial\mathbf{R}}{\partial\hat{\mathbf{v}}}\right)_n^{-1} \mathbf{R}_n$

5. Residual Derivative

   $\dfrac{\partial\mathbf{R}}{\partial\hat{\mathbf{v}}} = \int_v (\nabla_x N_i)^T \mathbf{k} (\nabla_x N_i) dv + \int_v (\nabla_x N_i)^T \sigma \otimes (\nabla_x N_i) dv$

6. Material Stiffness

   $K_M = \int_v (\nabla_x N_i)^T \mathbf{k} (\nabla_x N_i) dv = \int_v B^T D_{ep} B dv$

7. Geometrical Stiffness

   $K_\sigma = \int_v (\nabla_x N_i)^T \sigma \otimes (\nabla_x N_i) dv = \int_v B_\sigma^T \sigma B_\sigma dv$

8. Calculation of σ and D_{ep} in Appendix B.

APPENDIX B

General Steps of Acquiring System Stiffness–CP

1. Kinematics

$$\mathbf{F}(\tau) = \mathbf{F}^e(\tau)\,\mathbf{F}^p(\tau) \quad , \quad \dot{\mathbf{F}}^p(\tau) = \mathbf{l}^p(\tau)\,\mathbf{F}^p(\tau)$$

2. Plastic Deformation Rate Dependence

$$\mathbf{l}^p = \sum_{\alpha=1}^{nslip} \dot{\gamma}^\alpha(\tau)\,\mathbf{m}_0^\alpha \otimes \mathbf{n}_0^\alpha \;\Rightarrow\; \dot{\mathbf{F}}^p = \left(\sum_{\alpha=1}^{nslip} \dot{\gamma}^\alpha(\tau)\,\mathbf{m}_0^\alpha \otimes \mathbf{n}_0^\alpha\right)\mathbf{F}^p$$

3. Second Piola-Kircchoff Stress

$$\mathbf{S}(\tau) = \frac{1}{2}\mathbf{C}\left(\mathbf{F}^{eT}(\tau)\mathbf{F}^e(\tau) - \mathbf{I}\right)$$

$$\mathbf{S}(\tau) = \frac{\mathbf{C}}{2}\left[\sum_{\alpha=1}^{nslip}\left(\mathbf{I} - \Delta\gamma^\alpha\,(\mathbf{m}_0^\alpha \otimes \mathbf{n}_0^\alpha)^T\right)\mathbf{F}^{p-T}(t)\mathbf{F}^T(\tau)\mathbf{F}(\tau)\mathbf{F}^{-p}(t)\sum_{\alpha=1}^{nslip}\left(\mathbf{I} - \Delta\gamma^\alpha\,\mathbf{m}_0^\alpha \otimes \mathbf{n}_0^\alpha\right) - \mathbf{I}\right]$$

4. Elastoplastic Parts

$$\mathbf{S}_{el}(\tau) = \tfrac{\mathbf{C}}{2}\left(\mathbf{F}^{p-T}(t)\mathbf{F}^T(\tau)\mathbf{F}(\tau)\mathbf{F}^{-p}(t) - \mathbf{I}\right)$$

$$\mathbf{S}_{pl}(\tau) = -\tfrac{\mathbf{C}}{2}\left(\mathbf{F}^{p-T}(t)\mathbf{F}^T(\tau)\mathbf{F}(\tau)\mathbf{F}^{-p}(t)\sum_{\alpha=1}^{nslip}\left(\Delta\gamma^\alpha\,\mathbf{m}_0^\alpha \otimes \mathbf{n}_0^\alpha\right)\right)$$

$$-\tfrac{\mathbf{C}}{2}\left(\sum_{\alpha=1}^{nslip}\left(\Delta\gamma^\alpha\,\mathbf{m}_0^\alpha \otimes \mathbf{n}_0^\alpha\right)^T\mathbf{F}^{p-T}(t)\mathbf{F}^T(\tau)\mathbf{F}(\tau)\mathbf{F}^{-p}(t)\right)$$

5. Nonlinear Solution–Defined Residual Function

$$\mathbf{G}(\mathbf{S}) = \mathbf{S}(\tau) - \mathbf{S}_{el} - \tfrac{\mathbf{C}}{2}\sum_{\alpha=1}^{nslip}\mathcal{F}(\alpha)\Delta\gamma^\alpha$$

6. Nonlinear Iteration Obtaining 2nd Piola-Kircchoff Stress

$$\mathbf{S}^{(i+1)} = \mathbf{S}^{(i)} - \mathbf{J}^{-1}\left[\mathbf{S}^{(i)} - \mathbf{S}_{tr} + \sum_{\alpha=1}^{nslip}\mathcal{F}(\alpha)\,\Delta\gamma^\alpha\right]$$

$$\mathbf{J} = \mathbf{I} + \sum_{\alpha=1}^{nslip}\mathcal{F}(\alpha) \otimes \frac{\partial\gamma^\alpha}{\partial\mathbf{S}}$$

7. Updated Constitutive Model and Evolving Parameters

$$\dot{\gamma}^{\alpha} = \dot{\gamma}_0^{\alpha} \exp\left\{-\frac{Q_{active}}{k_B T}\left[1 - \left(\frac{(\tau_{\text{eff}}^{\alpha})^2}{\tau_{\text{cut}}^{\alpha}} \frac{c_s \pi}{\mu b}\, d\right)^{p}\right]^{q}\right\} \text{sgn}(\tau^{\alpha})$$

$$\dot{\tau}_{pass}^{\alpha} = \sum_{\beta=1}^{nslip} \mathbf{h}^{\alpha\beta} |\dot{\gamma}^{\beta}|$$

8. Elastic Deformation Gradient

$$(\text{Converged } \sigma\,,\ \mathbf{F}^{p}) \rightarrow \mathbf{F}^{e}(\tau) = \mathbf{F}(\tau)\mathbf{F}^{-p}(\tau)$$

9. Cauchy Stress

$$\boldsymbol{\sigma}(\tau) = \frac{1}{\det \mathbf{F}^{e}(\tau)} \mathbf{F}^{\mathbf{e}T}(\tau)\mathbf{S}(\tau)\mathbf{F}^{e}(\tau)$$

10. Elastoplastic Material Tensor

$$\mathbf{D}_{ep} \downarrow = \mathbf{W} = \frac{\partial \sigma}{\partial \mathbf{E}}$$

REFERENCES

[1] N. Mara, D. Bhattacharyya, J. Hirth, P. Dickerson, A. Misra, Mechanism for shear banding in nanolayered composites, Applied Physics Letters 97 (2) (2010) 021909.

[2] I. N. Mastorakos, R. L. Schoeppner, B. Kowalczyk, D. F. Bahr, The effect of size and composition on the strength and hardening of cu–ni/nb nanoscale metallic composites, Journal of Materials Research 32 (13) (2017) 2542–2550.

[3] P. Guruprasad, A. Benzerga, Size effects under homogeneous deformation of single crystals: a discrete dislocation analysis, Journal of the Mechanics and Physics of Solids 56 (1) (2008) 132–156.

[4] F. Delaire, J. Raphanel, C. Rey, Plastic heterogeneities of a copper multicrystal deformed in uniaxial tension: experimental study and finite element simulations, Acta Materialia 48 (5) (2000) 1075–1087.

[5] T. Tinga, W. Brekelmans, M. Geers, Time-incremental creep–fatigue damage rule for single crystal ni-base superalloys, Materials Science and Engineering: A 508 (1-2) (2009) 200–208.

[6] A. T. Jennings, M. J. Burek, J. R. Greer, Microstructure versus size: mechanical properties of electroplated single crystalline cu nanopillars, Physical review letters 104 (13) (2010) 135503.

[7] H. Yamada, T. Kami, R. Mori, T. Kudo, M. Okada, Strain rate dependence of material strength in aa5xxx series aluminum alloys and evaluation of their constitutive equation, Metals 8 (8) (2018) 576.

[8] J. Snel, M. Monclús, M. Castillo-Rodriguez, N. Mara, I. Beyerlein, J. Llorca, J. M. Molina-Aldareguia, Deformation mechanism map of cu/nb nanoscale metallic multilayers as a function of temperature and layer thickness, Jom 69 (11) (2017) 2214–2226.

[9] N. Mara, A. Misra, R. Hoagland, A. Sergueeva, T. Tamayo, P. Dickerson, A. Mukherjee, High-temperature mechanical behavior/microstructure correlation of cu/nb nanoscale multilayers, Materials Science and Engineering: A 493 (1-2) (2008) 274–282.

[10] S. O. Funtowicz, J. R. Ravetz, Uncertainty and quality in science for policy, Vol. 15, Springer Science & Business Media, 1990.

[11] B. Iooss, A. Saltelli, Introduction to sensitivity analysis, Handbook of uncertainty quantification (2017) 1103–1122.

[12] L. Li, Z. Zhang, J. Tan, C. Jiang, R. Qu, P. Zhang, J. Yang, Z. Zhang, Stepwise work hardening induced by individual grain boundary in cu bicrystal micropillars, Scientific reports 5 (2015) 15631.

[13] A. Schneider, D. Kaufmann, B. Clark, C. Frick, P. Gruber, R. Mönig, O. Kraft, E. Arzt, Correlation between critical temperature and strength of small-scale bcc pillars, Physical review letters 103 (10) (2009) 105501.

[14] D. Hull, D. J. Bacon, Introduction to dislocations, Vol. 37, Elsevier, 2011.

[15] W. D. Nix, Mechanical properties of thin films, Metallurgical transactions A 20 (11) (1989) 2217.

[16] I. J. Beyerlein, J. R. Mayeur, Mesoscale investigations for the evolution of interfaces in plasticity, Current Opinion in Solid State and Materials Science 19 (4) (2015) 203–211.

[17] J. Mayeur, I. Beyerlein, C. Bronkhorst, H. Mourad, B. Hansen, A crystal plasticity study of heterophase interface character stability of cu/nb bicrystals, International Journal of Plasticity 48 (2013) 72–91.

[18] E. Hall, Proc. phys. soc, Series B 64 (1951) 747.

[19] N. Petch, J iron steel inst, London 174 (1) (1953) 25–8.

[20] J. P. Hirth, The influence of grain boundaries on mechanical properties, Metallurgical Transactions 3 (12) (1972) 3047–3067.

[21] J. Schiøtz, K. W. Jacobsen, A maximum in the strength of nanocrystalline copper, Science 301 (5638) (2003) 1357–1359.

[22] E. Kroner, On the plastic deformation of polycrystals, Acta Metallurgica 9 (2) (1961) 155–161.

[23] D. Peirce, R. Asaro, A. Needleman, An analysis of nonuniform and localized deformation in ductile single crystals, Acta metallurgica 30 (6) (1982) 1087–1119.

[24] W. A. Curtin, R. E. Miller, Atomistic/continuum coupling in computational materials science, Modelling and simulation in materials science and engineering 11 (3) (2003) R33.

[25] F. Roters, P. Eisenlohr, L. Hantcherli, D. D. Tjahjanto, T. R. Bieler, D. Raabe, Overview of constitutive laws, kinematics, homogenization and multiscale methods in crystal plasticity finite-element modeling: Theory, experiments, applications, Acta Materialia 58 (4) (2010) 1152–1211.

[26] R. J. Asaro, J. Rice, Strain localization in ductile single crystals, Journal of the Mechanics and Physics of Solids 25 (5) (1977) 309–338.

[27] E. Orowan, Zur kristallplastizität. iii, Zeitschrift für Physik 89 (9-10) (1934) 634–659.

[28] J. R. Rice, Inelastic constitutive relations for solids: an internal-variable theory and its application to metal plasticity, Journal of the Mechanics and Physics of Solids 19 (6) (1971) 433–455.

[29] H. Gao, Y. Huang, Geometrically necessary dislocation and size-dependent plasticity, Scripta Materialia 48 (2) (2003) 113–118.

[30] A. Ma, F. Roters, D. Raabe, A dislocation density based constitutive model for crystal plasticity fem including geometrically necessary dislocations, Acta Materialia 54 (8) (2006) 2169–2179.

[31] J. Nye, Some geometrical relations in dislocated crystals, Acta metallurgica 1 (2) (1953) 153–162.

[32] M. Ashby, The deformation of plastically non-homogeneous materials, Philosophical Magazine 21 (170) (1970) 399–424.

[33] E. Kröner, et al., Continuum theory of defects, Physics of defects 35 (1981) 217–315.

[34] J. H. Holland, et al., Adaptation in natural and artificial systems: an introductory analysis with applications to biology, control, and artificial intelligence, MIT press, 1992.

[35] D. E. Goldberg, J. H. Holland, Genetic algorithms and machine learning.

[36] H. Gleiter, N. Hansen, A. Horsewell, T. Leffers, H. Lilholt, Deformation of polycrystals: Mechanisms and microstructures, in: Proc. of 2nd RISO Symposium on Metallurgy and Materials Science., 1981, pp. 15–21.

[37] H. Gleiter, Nanostructured materials: basic concepts and microstructure, Acta materialia 48 (1) (2000) 1–29.

[38] J. Wang, A. Misra, An overview of interface-dominated deformation mechanisms in metallic multilayers, Current Opinion in Solid State and Materials Science 15 (1) (2011) 20–28.

[39] Y. Yamazaki, H. Gleiter, C. Wu, Z.-c. OY, Non-equilibrium properties of nano structured materials, in: Materials Science Forum, Vol. 426, Trans Tech Publications Ltd., Zurich-Uetikon, Switzerland, 2003, pp. 2363–2368.

[40] M. Demkowicz, R. Hoagland, J. Hirth, Interface structure and radiation damage resistance in cu-nb multilayer nanocomposites, Physical review letters 100 (13) (2008) 136102.

[41] R. Birringer, Nanocrystalline materials, Materials Science and Engineering: A 117 (1989) 33–43.

[42] H. Gleiter, H. Hahn, T. Schimmel, Advances in nanomaterials (2013).

[43] J. Koehler, Attempt to design a strong solid, Physical review B 2 (2) (1970) 547.

[44] M. Dao, L. Lu, R. Asaro, J. T. M. De Hosson, E. Ma, Toward a quantitative understanding of mechanical behavior of nanocrystalline metals, Acta Materialia 55 (12) (2007) 4041–4065.

[45] Y. Wang, M. Chen, F. Zhou, E. Ma, High tensile ductility in a nanostructured metal, Nature 419 (6910) (2002) 912.

[46] C. Koch, Optimization of strength and ductility in nanocrystalline and ultrafine grained metals, Scripta Materialia 49 (7) (2003) 657–662.

[47] K. Kumar, S. Suresh, M. Chisholm, J. Horton, P. Wang, Deformation of electrodeposited nanocrystalline nickel, Acta Materialia 51 (2) (2003) 387–405.

[48] M. Chen, E. Ma, K. J. Hemker, H. Sheng, Y. Wang, X. Cheng, Deformation twinning in nanocrystalline aluminum, Science 300 (5623) (2003) 1275–1277.

[49] M. A. Meyers, A. Mishra, D. J. Benson, Mechanical properties of nanocrystalline materials, Progress in materials science 51 (4) (2006) 427–556.

[50] R. Valiev, I. Alexandrov, Y. Zhu, T. Lowe, Paradox of strength and ductility in metals processed bysevere plastic deformation, Journal of Materials Research 17 (1) (2002) 5–8.

[51] A. Misra, J. Hirth, R. Hoagland, Length-scale-dependent deformation mechanisms in incoherent metallic multilayered composites, Acta materialia 53 (18) (2005) 4817–4824.

[52] A. Misra, M. Demkowicz, X. Zhang, R. Hoagland, The radiation damage tolerance of ultra-high strength nanolayered composites, Jom 59 (9) (2007) 62–65.

[53] J. Carpenter, S. Vogel, J. LeDonne, D. Hammon, I. Beyerlein, N. A. Mara, Bulk texture evolution of cu–nb nanolamellar composites during accumulative roll bonding, Acta materialia 60 (4) (2012) 1576–1586.

[54] M. Ashby, Results and consequences of a recalculation of the frank-read and the orowan stress, Acta Metallurgica 14 (5) (1966) 679–681.

[55] G. Dehm, B. N. Jaya, R. Raghavan, C. Kirchlechner, Overview on micro-and nanomechanical testing: New insights in interface plasticity and fracture at small length scales, Acta Materialia 142 (2018) 248–282.

[56] R. Raghavan, J. M. Wheeler, T. P. Harzer, V. Chawla, S. Djaziri, K. Thomas, B. Philippi, C. Kirchlechner, B. N. Jaya, J. Wehrs, et al., Transition from shear to stress-assisted diffusion of copper–chromium nanolayered thin films at elevated temperatures, Acta Materialia 100 (2015) 73–80.

[57] A. H. Cottrell, Dislocations and plastic flow in crystals.

[58] J. Langer, E. Bouchbinder, T. Lookman, Thermodynamic theory of dislocation-mediated plasticity, Acta Materialia 58 (10) (2010) 3718–3732.

[59] C. Truesdell, R. Toupin, The classical field theories, in: Principles of classical mechanics and field theory/Prinzipien der Klassischen Mechanik und Feldtheorie, Springer, 1960, pp. 226–858.

[60] B. D. Coleman, W. Noll, The thermodynamics of elastic materials with heat conduction and viscosity, in: The Foundations of Mechanics and Thermodynamics, Springer, 1974, pp. 145–156.

[61] A. G. Holzapfel, Nonlinear solid mechanics ii.

[62] H. J. Frost, M. F. Ashby, Deformation mechanism maps: the plasticity and creep of metals and ceramics, Pergamon press, 1982.

[63] W. Kocks, Thermodynamics and kinetics of slip, Progr. Mater. Sci. 19 (1975) 291.

[64] H. Van Swygenhoven, P. Derlet, A. Frøseth, Nucleation and propagation of dislocations in nanocrystalline fcc metals, Acta Materialia 54 (7) (2006) 1975–1983.

[65] S. Keshavarz, Z. Molaeinia, A. Reid, S. Langer, Morphology dependent flow stress in nickel-based superalloys in the multi-scale crystal plasticity framework, Crystals 7 (11) (2017) 334.

[66] Y. Freund, R. E. Schapire, et al., Experiments with a new boosting algorithm, in: icml, Vol. 96, Citeseer, 1996, pp. 148–156.

[67] J. H. Friedman, Greedy function approximation: a gradient boosting machine, Annals of statistics (2001) 1189–1232.

[68] J. Friedman, T. Hastie, R. Tibshirani, et al., Additive logistic regression: a statistical view of boosting (with discussion and a rejoinder by the authors), The annals of statistics 28 (2) (2000) 337–407.

[69] J.-Y. Kim, D. Jang, J. R. Greer, Insight into the deformation behavior of niobium single crystals under uniaxial compression and tension at the nanoscale, Scripta Materialia 61 (3) (2009) 300–303.

[70] A. Chokshi, A. Rosen, J. Karch, H. Gleiter, On the validity of the hall-petch relationship in nanocrystalline materials, Scripta Metallurgica 23 (10) (1989) 1679–1683.

[71] A. Argon, S. Yip, The strongest size, Philosophical Magazine Letters 86 (11) (2006) 713–720.

[72] V. L. Berdichevsky, Variational principles, in: Variational Principles of Continuum Mechanics, Springer, 2009, pp. 3–44.

[73] V. Berdichevsky, Thermodynamics of chaos and order, Vol. 90, CRC Press, 1997.

[74] V. L. Berdichevsky, Homogenization in micro-plasticity, Journal of the Mechanics and Physics of Solids 53 (11) (2005) 2457–2469.

[75] G. I. Taylor, Plastic strain in metals, J. Inst. Metals 62 (1938) 307–324.

[76] U. Kocks, The relation between polycrystal deformation and single-crystal deformation, Metallurgical and Materials Transactions B 1 (5) (1970) 1121–1143.

[77] R. Hill, Elastic properties of reinforced solids: some theoretical principles, Journal of the Mechanics and Physics of Solids 11 (5) (1963) 357–372.

[78] R. Hill, On constitutive macro-variables for heterogeneous solids at finite strain, Proceedings of the Royal Society of London. A. Mathematical and Physical Sciences 326 (1565) (1972) 131–147.

[79] C. Herring, Diffusional viscosity of a polycrystalline solid, Journal of applied physics 21 (5) (1950) 437–445.

[80] R. Coble, A model for boundary diffusion controlled creep in polycrystalline materials, Journal of applied physics 34 (6) (1963) 1679–1682.

[81] J. Carpenter, S. Zheng, R. Zhang, S. Vogel, I. Beyerlein, N. Mara, Thermal stability of cu–nb nanolamellar composites fabricated via accumulative roll bonding, Philosophical Magazine 93 (7) (2013) 718–735.

[82] A. Misra, R. Hoagland, H. Kung, Thermal stability of self-supported nanolayered cu/nb films, Philosophical Magazine 84 (10) (2004) 1021–1028.

[83] C. K. Lieou, C. A. Bronkhorst, Thermodynamic theory of crystal plasticity: formulation and application to polycrystal fcc copper, Journal of the Mechanics and Physics of Solids (2020) 103905.

[84] A. Saltelli, Making best use of model evaluations to compute sensitivity indices, Computer physics communications 145 (2) (2002) 280–297.

[85] J. C. Helton, J. D. Johnson, C. J. Sallaberry, C. B. Storlie, Survey of sampling-based methods for uncertainty and sensitivity analysis, Reliability Engineering & System Safety 91 (10-11) (2006) 1175–1209.

[86] A. Saltelli, M. Ratto, T. Andres, F. Campolongo, J. Cariboni, D. Gatelli, M. Saisana, S. Tarantola, Global sensitivity analysis: the primer, John Wiley & Sons, 2008.

[87] A. Saltelli, S. Tarantola, F. Campolongo, et al., Sensitivity anaysis as an ingredient of modeling, Statistical Science 15 (4) (2000) 377–395.

[88] E. De Rocquigny, N. Devictor, S. Tarantola, Uncertainty in industrial practice: a guide to quantitative uncertainty management, John Wiley & Sons, 2008.

[89] A. Saltelli, S. Tarantola, F. Campolongo, M. Ratto, Sensitivity analysis in practice: a guide to assessing scientific models, Vol. 1, Wiley Online Library, 2004.

[90] D. Kurowicka, R. M. Cooke, Uncertainty analysis with high dimensional dependence modelling, John Wiley & Sons, 2006.

[91] E. Hall, The deformation and ageing of mild steel: Iii discussion of results, Proceedings of the Physical Society. Section B 64 (9) (1951) 747.

[92] G. E. Dieter, D. J. Bacon, Mechanical metallurgy, Vol. 3, McGraw-hill New York, 1986.

[93] A. Argon, Strengthening mechanisms in crystal plasticity, Vol. 4, Oxford University Press on Demand, 2008.

[94] Z. Molaeinia, Non-linear finite element simulations of hydrogen diffusion and hydrogen-dislocation interactions, Ph.D. thesis, Johns Hopkins University (2015).

[95] J. D. Eshelby, The determination of the elastic field of an ellipsoidal inclusion, and related problems, Proceedings of the royal society of London. Series A. Mathematical and physical sciences 241 (1226) (1957) 376–396.

[96] A. E. H. Love, A treatise on the mathematical theory of elasticity, Cambridge university press, 2013.

[97] E. Orowan, Symp. on internal stress in metals & alloys', london, institute of metals (1947).

[98] W. F. Hosford, Mechanical behavior of materials, Cambridge university press, 2010.